Chair of General and Analytical Chemistry

Doctoral Thesis

Depassivation and Repassivation of Stainless Steels

Emir Mujanović, univ. dipl. inž. str.

March 2020

MONTANUNIVERSITÄT LEOBEN
www.unileoben.ac.at

Affidavit

I declare on oath that I wrote this thesis independently, did not use other than the specified sources and aids, and did not otherwise use any unauthorized aids.

I declare that I have read, understood, and complied with the guidelines of the senate of the Montanuniversität Leoben for "Good Scientific Practice".

Furthermore, I declare that the electronic and printed version of the submitted thesis are identical, both, formally and with regard to content.

March 3rd, 2020

Emir Mujanović

Kurzfassung

Bei der Öl- und Gasgewinnung werden in Sonden mit hoher Aggressivität oftmals hochbeständige, passive Stähle eingesetzt. Diese erhalten ihre ausgezeichneten Korrosionseigenschaften durch die Ausbildung einer Chrom- und Molybdänreichen Passivschicht. Bei Säuerungen zur Wiederfreilegung von Verkalkungen bzw. durch Förderung von Sand können lokale oder großflächige Depassivierungen auftreten, die zu einer hohen Korrosionsrate auf die verwendeten Stähle führen.

In der vorliegenden Arbeit wurde die chemische Beständigkeit von Passivschichten unterschiedlicher Stähle sowie die Bedingungen und Kinetik ihrer erneuten Bildung mit Hilfe von Auslagerungsversuchen, Kratztests und in Durchflusszellen bei Variation des pH-Werts untersucht. Die Ergebnisse zeigen, dass mit Ausnahme besonders niedrig legierter passiver Stähle alle übrigen eine Repassivierung nach Säuerungen bei Wiederanstieg des pH-Werts über 3 erreichen und dass die Passivschichtbildung innerhalb von 100 s hinreichend weit fortgeschritten, aber noch nicht vollständig abgeschlossen ist.

Abstract

In oil and gas production, deep wells producing highly aggressive media are often completed with highly alloyed corrosion resistant alloys (CRAs, mainly steels). These CRAs have excellent corrosion properties due to the formation of a passive layer of chromium, iron and molybdenum oxides and hydroxides. During acidizing jobs, when a plugged well is re-opened, and during sand production at high flow velocities, localized or uniform depassivation can occur and yield high corrosion rates of used CRAs.

In the present work the resistance of passive layers of various stainless steels was investigated alongside the conditions and kinetics of when these layers are rebuilt. Methods applied consisted of: potentiodynamic experiments, immersion tests, scratch tests and variable pH flow experiments. Results revealed that, with the exception of those with very low alloys, all stainless steels showed repassivation after acidizing when the pH level increased above 3. Repassivation occurs within 100 s to a certain (sufficient) extent, although the passive layer is not completely rebuilt within this period.

Acknowledgement

I want to thank Assoc.Prof. Dr. Gregor Mori, Montanuniversität Leoben, for the supervision of this thesis, for being a mentor and for his ongoing support in the last three years.

I owe a very special thanks to Assoc.Prof. Dr. Andraž Legat for being an examiner of this thesis and giving me guiding talks during the last three years.

My deepest thanks go to Dr. Tadeja Kosec and Dr. Bojan Zajec at ZAG, who supported, pushed, helped and enriched me throughout the last three years. They gave me the great opportunity to work with them and to learn from them about corrosion and many other topics.

Especially I want to thank my industrial partners Dr. Gerald Zehethofer and Dr. Stefan Hönig, OMV Austria Exploration and Production, who enabled this work and gave financial support as well as many highly valuable discussions during our meetings.

I want to thank very sincerely Dr. Mirjam Bajt Leban for her support during the first year, while she worked at ZAG, and for her motivation and spirit.

Assoc.Prof. Dr. Janez Kovač, Institute Jožef Stefan, I want to thank very sincerely for the joint discussions and the XPS and ToF-SIMS analysis.

To my working colleagues at ZAG, Dr. Miha Hren, Mag. Nina Gartner and Dr. Petra Močnik I want to express special thanks for the good working climate, their acceptance, patience, support and often joy that they brought to me during work.

To my working colleagues at Montanuniversität Leoben Dr. Jojo Vidic, Dipl.-Ing. Anton Trautmann, Dipl.-Ing. Wolfgang Siegl, Hubert Falk and Melissa Eberhard I want to thank for their warm welcome in their labs and for all the support during my 9 month stay in Leoben.

Above all I want to thank my parents, who with their love and encouragement allowed me to study for such a long time, who always supported me in all phases of my life and to whom I want to dedicate this work.

Table of Contents

1 Introduction

As with many other industries, corrosion in oil and gas production is a large concern in regards to maintaining a profitable business venture. Corrosion is one of the main factors in determining the lifetime of the OCTG (oil country tubular goods) installed in an oil well, and steps must be taken to ensure that completion can stay in use as long as the oil or gas well is actively producing. The possibilities for corrosion protection vary from corrosion inhibitors used in combination with carbon steel to the use of stainless steel. In this work the possibility of using different stainless steels is examined, where special focus is paid to protectiveness and stability of the oxide layer formed on the surface of these steels under various conditions.

There are two principle possible ways that a passive layer may be destroyed, and both may be present in oil and gas production. The first is mechanical depassivation, which may occur by impacts of hard particles (e.g. sand) flowing in the liquid being produced or by tool insertion. The other form is chemical depassivation, which occurs when the conditions in the oil well are too aggressive for the passive layer to persist. In the case of oil production this usually occurs during acidizing jobs, where a strong acid (e.g. concentrated HCl) is introduced into the well to dissolve precipitated limestone in the reservoir. Afterwards the production begins again and pH inside the well increases back to operating values, ranging mostly between 4 and 7, depending on the well. One of the main concerns with the use of stainless steel in oil and gas production is whether the steel can form a new passive layer under the aggressive conditions inside an oil well, after the existing one has been damaged. Primary aim of this research will be to determine the limit conditions for this kind of repassivation in combination with different stainless steels.

2 Theory

2.1 Passivity of stainless steels

Steels containing at least 10.5 % of chromium are considered stainless steels. The reason for this is in the protective oxide layer formed on such steels, containing chromium and/or iron oxy-hydroxides. These form the passive layers with an average thickness between 1 and 4 nm. The passive layer greatly slows down oxidation and protects the underlying metal from corrosion. If a passive layer is mechanically damaged, the underlying metal will repassivate under suitable conditions and form a new passive layer. So the passive layer is a self-healing, natural layer of certain metals and alloys. A graphical representation of passive layer formation is shown in Figure 2.1 [1].

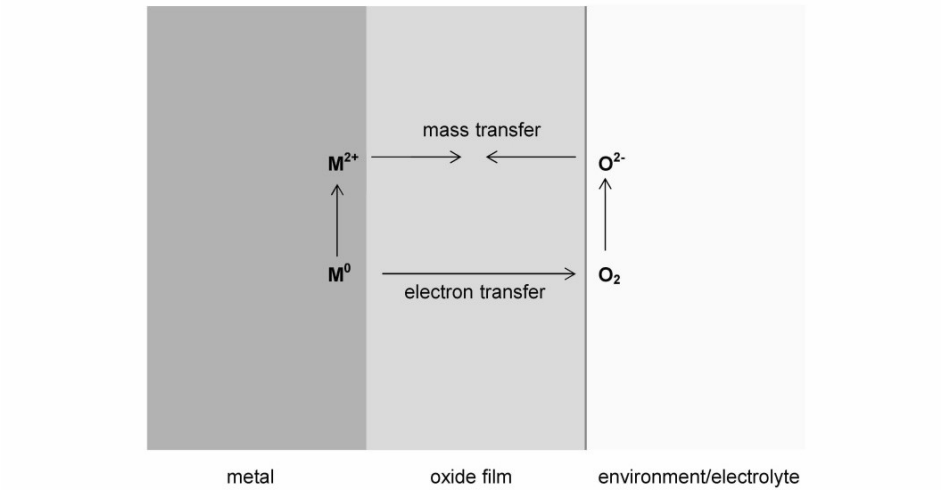

Figure 2.1: Growth of an oxide film on a metal surface [1]

There are several theories on how passive layers work, however, it is widely accepted that the protectiveness of the passive layer depends on how thick it is and what the defect density in the layer is. For a passive layer to exist, it must be thin enough to not break due to mechanical stress, which means the defect density must be low enough to ensure proper protection when the layer is thin.

All passive layers work as semi-conductors, reducing the amount of electron flow [2]. Since passive layer formation/growth is in fact oxidation, one may consider the passive layer thickness as a rate limiting factor for oxidation kinetics. The thicker the oxide layer is, the more time ions take to diffuse through the oxide layer. This will limit the passive layer thickness. Kinetics of oxidation is retarded, as the layer thickens. Still some minor dissolution occurs at the oxide layer/electrolyte interface. This behavior results in low corrosion rates of passive metals and alloys compared to active ones. A steady state is reached once the oxidation rate reaches the oxide dissolution rate. Once a steady state is achieved, the oxide layer thickness remains constant as the oxidation speed equals the dissolution rate, also known as the corrosion rate.

The passive layer is usually comprised of several different metal oxides, with different concentration of metal oxides across the thickness of the film. It can be divided into the "outer" and "inner" part of the film. When a stainless steel forms such a passive film, the steel found beneath the passive layer can also be divided, into the bulk metal deep in the metal part and the underlying metal, found just underneath the passive film, which has a modified chemical composition in comparison to the bulk [3]. Usually it is enriched in nickel and nitrogen, however this may vary depending on the conditions in which the passive film is formed.

The type of corrosive attack on steel depends on the steel/electrolyte combination. In cases where a passive layer is not present, uniform corrosion can be expected since oxidation and dissolution is present on the entire surface. When a passive layer is present however, different types of localized corrosive attack may appear, ranging from crevice corrosion in areas where the electrolyte is trapped, to pitting corrosion in the presence of halide ions, along with other forms of attack such as grain boundary attack on sensitized steel, corrosion under the influence of mechanical stress such as stress corrosion cracking, corrosion fatigue, erosion corrosion, and galvanic corrosion near joints of different metals and three-phase boundary corrosion.

The types of corrosive attack to be expected in oil and gas production are pitting corrosion due to the presence of chloride ions, stress corrosion cracking, erosion corrosion, general corrosion during acidizing jobs and hydrogen induced cracking or sulfide stress cracking due to the possible presence of H_2S gas [4].

2.1.1 Structure, thickness and chemical composition of passive layers

A passive layer will vary widely in its properties, depending on the metal/electrolyte combination. As mentioned previously, the thickness of the passive film depends on the defect density within the film itself as well as the presence of aggressive ions in the solution and the passivation process of the film. When steel is passivated with the help of oxidizing solutions such as HNO_3, the passive layer is generally quite thick without having a large defect density, meaning it will be more protective than one that has been formed in water or air (a less oxidizing environment compared to HNO_3) as a native passive film.

Presence of Cl^- ions in an environment will cause the native oxide layer to be thinner [5]. This however is not a result of a smaller defect density but a negative effect of chloride on film thickness. Addition of alloying elements to basic metals can greatly reduce the defect densities of their passive films thus enhancing their protective properties. Stainless steel is an example of such a complex alloy – apart from the needed chromium to make it stainless, it can contain other alloying elements such as molybdenum, tungsten, nickel and nitrogen, making the passive film more protective in different ways.

In neutral and alkaline pH solutions both iron and chromium oxy-hydroxides are found on the surface of the passive layer while in low pH solutions the passive film/electrolyte interface is strongly enriched in chromium as iron is dissolved. If the pH is reduced even further, to values well below 3, very little chromium is found on the surface of the film, and an enrichment in iron oxy-hydroxides takes place.

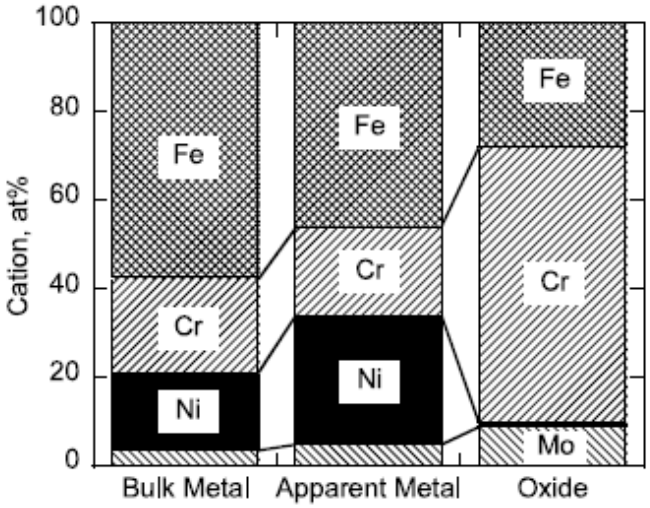

Figure 2.2: XPS results from a passive film formed in the high passive region in a 0.1 M HCl + 0.4 M NaCl solution. Figure shows chemical composition of the bulk metal, interface between bulk metal and passive layer (apparent metal) and passive layer of a Fe-Cr-Ni-Mo stainless steel [3]

In a similar fashion, other alloying elements such as nickel, molybdenum, tungsten, etc. are enriched or depleted either in the oxide layer/electrolyte interface or the metal/oxide layer interface (Figure 2.2 [3]), depending on the pH of the solution.

Pourbaix diagrams [6] may be used to predict the behavior of pure metals in water. Such diagrams describe, which chemical reactions take place at certain pH and potential values. Since this work is mostly focusing on solutions in the pH range of 4-7 with an additional interest in very acidic solutions, the Pourbaix diagrams below pH 7 are shortly discussed. It is noted that these diagrams show thermodynamic data. Neither overpotentials nor kinetic information are included in the diagrams. It should also be noted that once these pure metals are part of an alloy they may react at different pH-potential combinations and that changes of the electrolyte (for example NaCl salt addition) will affect these diagrams.

The Pourbaix diagrams for iron (Figures 2.3 (a) and (b)) show that both Fe_3O_4 and $Fe(OH)_2$ are unstable at pH 5-7 in low potential ranges. At an elevated potential however other oxides and hydroxides such as Fe_2O_3 and $Fe(OH)_3$ are stable even at lower pH values. Below pH 4.2 the oxides dissolve into Fe^{2+} ions between - 600 and 770 mV_{SHE}. Above 770 mV_{SHE} and below pH 4.2 Fe^{3+} ions are stable. At reducing potentials lower than - 620 mV_{SHE} metallic iron is stable and will not be corroded (all values are given for diluted electrolytes with an ion concentration of $1 \cdot 10^{-6}$ M, this is the most relevant case in corrosion issues).

It should also be noted that only the area between the two slightly decreasing lines a and b (in between which water is stable) has to be considered. The whole neutral to alkaline pH range in the water stability regime shows that $Fe(OH)_3$ or Fe_2O_3 is stable at more oxidizing potentials and $Fe(OH)_2$ or Fe_3O_4 in more reducing potentials. The diagram shows that iron is corroding actively in acidic solutions and reaches passivity in alkaline solution. When iron oxide or hydroxide is formed in a passive layer (which takes place in neutral to alkaline solutions) the iron species will be dissolved when the pH drops below 4 (thermodynamically, reaction can be hindered).

From the Pourbaix diagram of chromium (Figure 2.4) it can be seen that solid Cr_2O_3 and $Cr(OH)_3$ have a wide range of stability. The oxide and the hydroxide of chromium have a low defect density and this is the main cause for the ability to passivate. Chromium and also stainless steels are passive due to the wide stability range of chromium oxide and hydroxide.

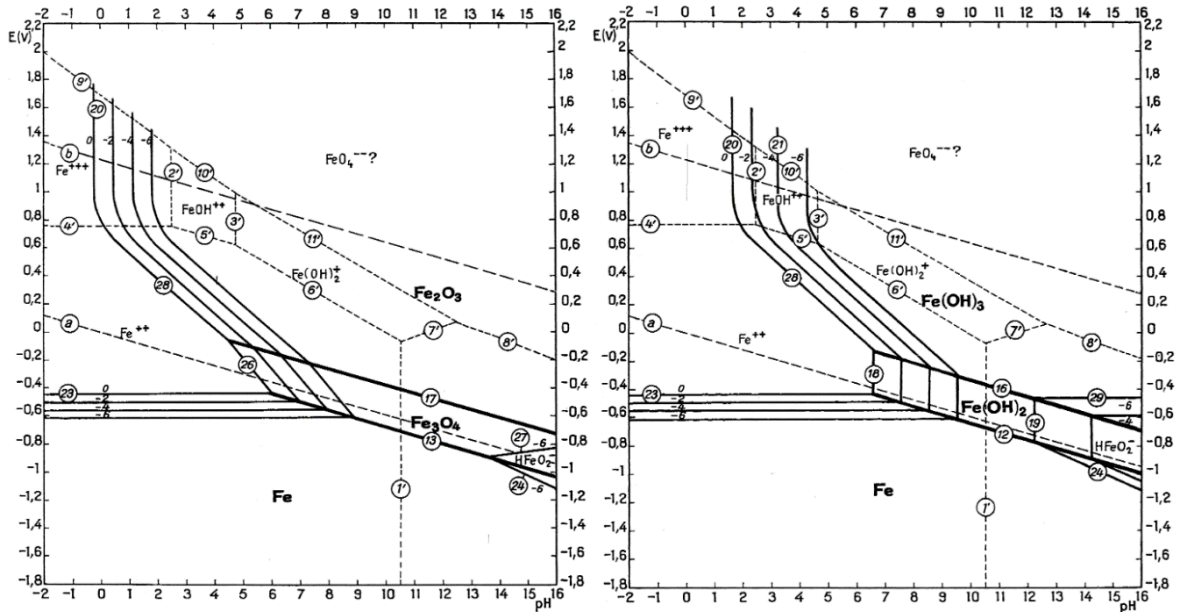

(a) (b)

Figure 2.3: Potential-pH equilibrium diagrams for the system iron-water at 25 °C, (a) considering as solid substances only Fe, Fe_3O_4 and Fe_2O_3, (b) considering as solid substances only Fe, $Fe(OH)_2$ and $Fe(OH)_3$ [6]

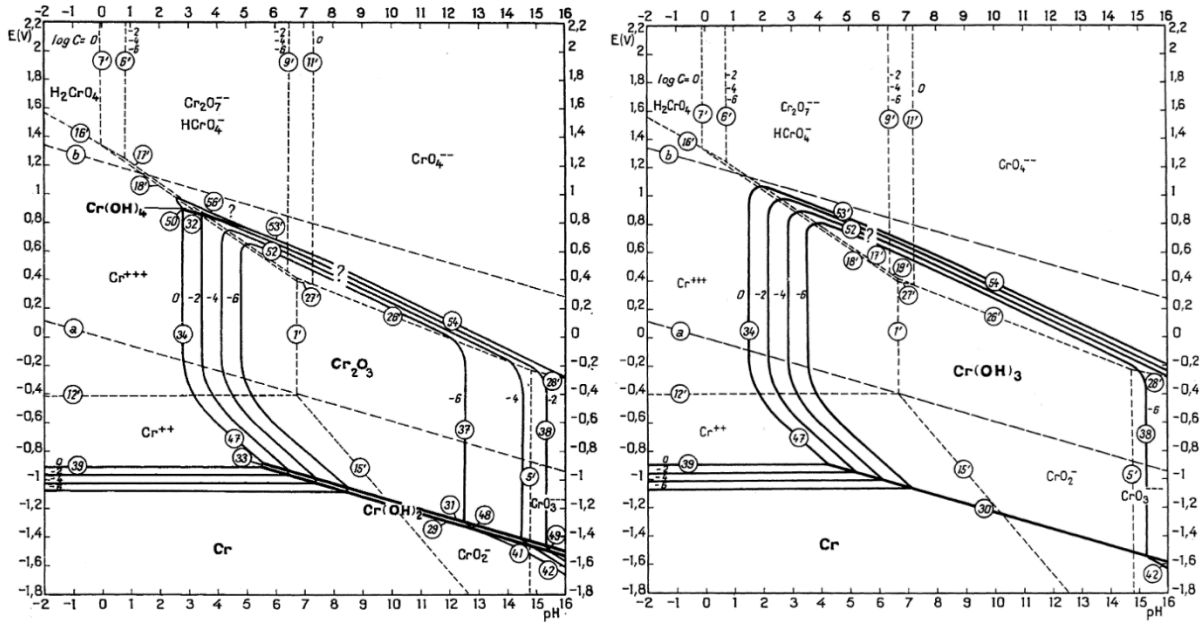

(a) (b)

Figure 2.4: Potential-pH equilibrium diagrams for the system chromium-water at 25 °C in solutions not containing chloride, (a) considering anhydrous Cr_2O_3, (b) considering $Cr(OH)_3$ [6]

When the pH decreases below 3.7, chromium is stable as divalent or trivalent ion and dissolves. At very high potentials close to and above oxygen formation (dotted line b in Figure 2.4) the hexavalent chromate ion is stable. This is the reason, why stainless steels show a so-called secondary passivity at very high potentials, where trivalent chromium hydroxide from the passive layer is dissolved to chromate ions – in this elevated potential range the iron hydroxide is still stable and protects the steel. Due to its higher defect order (which cannot be derived from the Pourbaix diagram) the protective effect of pure iron oxide/hydroxide is lower than the one for chromium oxide/hydroxide.

When considering the behavior of iron and chromium according to their Pourbaix diagrams one can see that in acids below pH ~4, stainless steel will be corroded actively since both metals are soluble. In neutral to alkaline solutions stainless steels are passive. Both metals form oxides or hydroxides. At very high potentials chromium can be oxidized to chromate ions, while iron still remains stable as an oxide. This will result in secondary passivity, which can be derived from Pourbaix diagrams and that is experimentally found especially in sulfuric acidic electrolytes (see Figure 2.5 [7]).

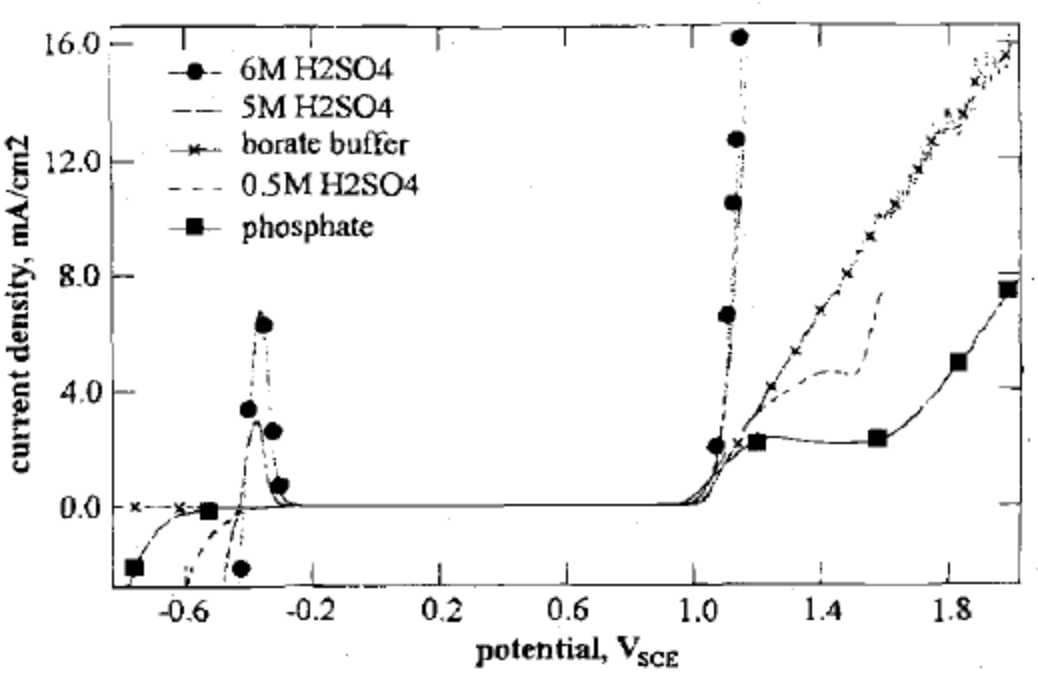

Figure 2.5: Secondary passivity of stainless steel 304 in 0.5M H_2SO_4 and phosphate solutions at potentials above 1 V_{SCE} [7]

The secondary passivity always shows a higher corrosion current density than the true passivity, where both metal oxides/hydroxides are contributing to passivity, since the defect

density of iron oxide/hydroxide is higher than that of chromium oxide/hydroxide or of the combined oxide/hydroxide.

The Pourbaix diagram for nickel (Figure 2.6 [6]), including both oxides and hydroxides, shows that nickel is actively corroding below pH 9, meaning the metal is not passive. Nevertheless nickel is a very noble element, which cannot form a passive layer on its own. Due to its very noble behavior nickel is depleted as an oxide in the passive layer, although its content is not zero [1]. Instead, it is not oxidized as easily as chromium or iron and is therefore enriched in the metal just underneath the passive film.

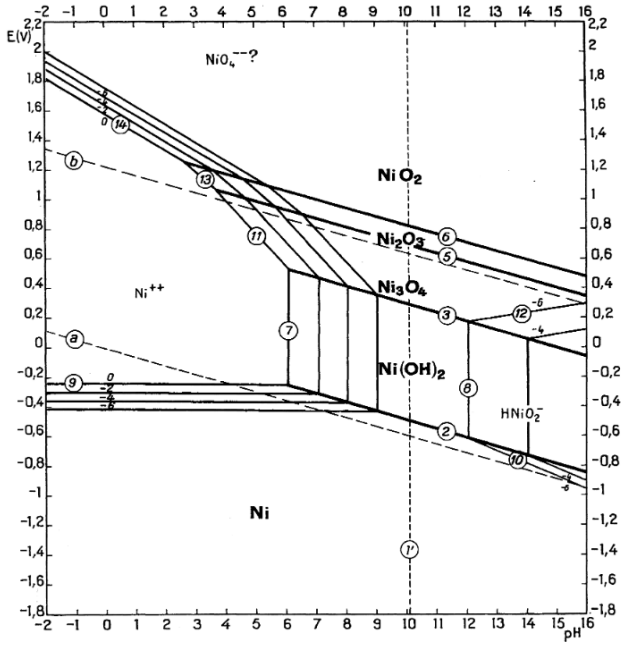

Figure 2.6: Potential-pH equilibrium diagram for the system nickel-water at 25 °C [6]

Molybdenum is a metal that supports many different oxidation states, allowing that it fills gaps in other metal oxides and reducing their defect density. Additionally, molybdenum is one of the few metals that forms stable oxides at very low pH values (below 3) as seen in Figure 2.7 [6]. Since molybdenum may be added to stainless steels and it lowers the defect density of the passive layer, it increases the corrosion resistance of stainless steels to a large extent. Especially the acid resistance of molybdenum oxide improves corrosion properties for stainless steels in the low pH range.

In alkaline solutions molybdenum is soluble as a molybdate as can be seen from Figure 2.7. In oxidizing media near line b (oxygen reduction) in Figure 2.7 molybdenum shall not be used either. Molybdenum has a high resistance in reducing media and in acidic media.

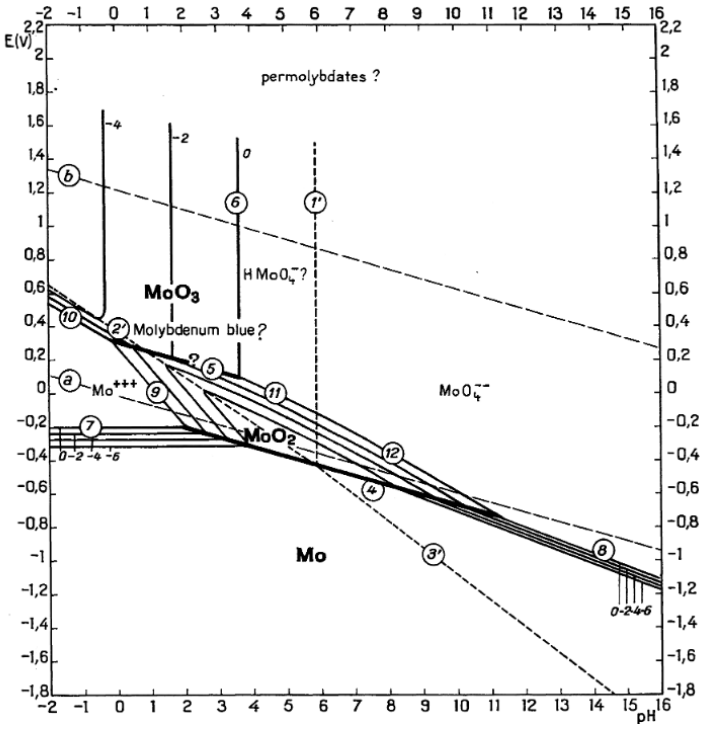

Figure 2.7: Potential-pH equilibrium diagram for the system molybdenum-water at 25 °C [6]

2.1.2 Effect of alloying elements on passivity

It is well documented that chromium, molybdenum and nitrogen have positive effects on the passivity of stainless steels. Of particular interest is the interaction between these alloying elements and how they work in conjunction with each other, leading to a synergistic effect [8]. A major concern is pitting corrosion and how this can lead to failure of the product, despite most of the steel staying intact. Due to this concern, nucleation and propagation of pits is a highly studied field in corrosion research, which has led to greater understanding of the mechanism involved and has proposed how different alloying elements in stainless steel affect resistance to pitting as a combination of the ability of nucleated pits to repassivate and the propagation rate of stable pits.

From 1969 on many authors have tried to correlate chemical composition with pitting resistance. The first, who have succeeded in a quantitative approach were Lorenz and Medawar 1969 [9]. By investigating a number of stainless steels according to ASTM G48, they found the empirical formula:

$$PREN = \%Cr + 3 \cdot \%Mo \quad (1).$$

Although this formula has no physical meaning, it has gained incredible importance since it represents a linear relation between chemical composition and the resistance of stainless steels to pitting and also to crevice corrosion. In the 70s up to the 90s, many authors have tried to optimize the early found PREN formula from Lorenz and Medawar. A compilation of different PREN formulae proposed by various authors has been presented by Mori and Bauernfeind [10]. The nowadays most widely used PREN formula is:

$$PREN = \%Cr + 3.3 \cdot \%Mo + 16 \ldots 30 \cdot \%N \quad (2).$$

The factor for nitrogen varies between 16 and 30. The higher the total content of alloying elements the higher is the positive effect of nitrogen in PREN and the higher is its factor in the PREN. This also shows that there is no physical meaning of PREN, but only an empirical attempt, to characterize the resistance to chlorides. Some authors have found more complex and maybe even more precise PREN formulae. Jargelius-Pettersson [11] has added synergistic effects of Mo and N. Jonsson et al. [12] have confirmed the positive effect of the alloying element tungsten. Note: Tungsten has the same positive effect like molybdenum on pitting resistance and can replace the latter, however due to its atomic weight AW being twice as high compared to that of molybdenum (AW_W = 184 g/mole vs AW_{Mo} = 96 g/mole) only half the number of atoms of tungsten compared to that of molybdenum are alloyed to the stainless steel when alloying the same weight percent of Mo and W to the steel. This results in a positive (beneficial) factor of 1.65 for tungsten in the PREN formula (factor of W is half of factor of Mo in PREN). Since only very seldomly tungsten is added to stainless steels, PREN including the tungsten term is seldomly used, although the positive effect of tungsten is undisputed.

In the early 2000s Speidel [13] has proposed a PREN that contained even more alloying elements. In his MARC (Measure of Alloying as a Resistance to Corrosion) and based on a large number of investigated steels with very different chemical compositions including high nitrogen steels as well as high manganese austenites, he proposed a negative effect of manganese and nickel:

$$MARC = \%Cr + 3.3 \cdot \%Mo + 20 \cdot (\%N + \%C) - 0.5 \cdot \%Mn - 0.25 \cdot \%Ni \quad (3).$$

In the last 15 years this measure however has not been widely accepted by other authors although especially the negative effect of manganese on passivity of stainless steels due to its un-noble nature and together with the high solubility of manganese oxide in the electrolyte from the passive layer seems to be reasonable. The dissolution of manganese from the passive layer has been found by several authors [14,15].

In the following section the effect of the most important and relevant alloying elements for maintaining a passive film in stainless steels is discussed.

Chromium

Although the factor of chromium in the PREN is lower than the factors of molybdenum and nitrogen, chromium is the most important element for maintaining a passive layer on stainless steels. Chromium forms the main structure of the passive layer consisting of trivalent chromium oxides and hydroxides with low defect order (Figure 2.8 [16]).

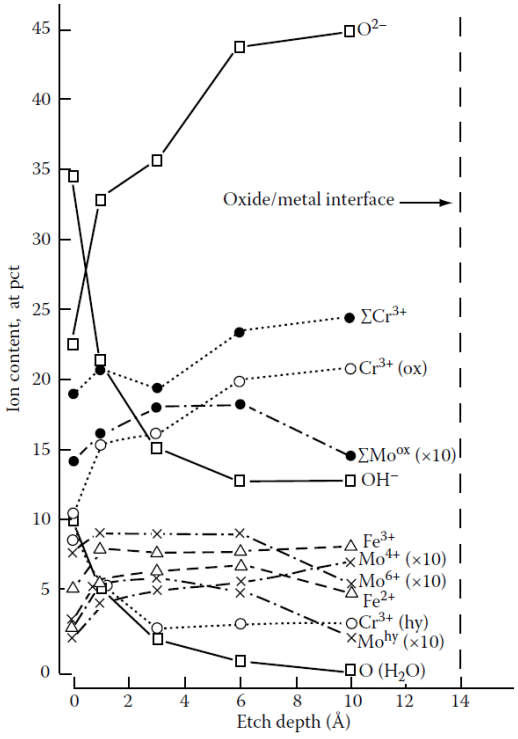

Figure 2.8: Ion content vs. etch depth for the austenitic stainless steel Fe18Cr14.3Ni2.5Mo polarized at 500 mV_{SCE} [16]

Above a chromium content of 10.5 to 11.5 %, steel can form this protective passive layer with a thickness of a few nm. The passive layer consists of an inner oxidized and an outer more hydrated layer. Chromium is enriched over iron in both layers, although iron content in the steels is higher than chromium content. This is due to its low electrochemical potential and high reactivity. Chromium determines the structure of the passive films on stainless steels. Without the presence of the above mentioned minimum chromium content of 10.5 to 11.5 % the passive layer cannot be maintained.

Molybdenum (and Tungsten)

Molybdenum is enriched in the passive layer like chromium. Molybdenum can be present in a number of oxidation states namely hexavalent and quadrivalent. Clayton and Olefjord state in

their review that quadrivalent molybdenum is in the inner region of the passive layer and hexavalent is more present in the outer region [16]. According to data from Olsson and Hörnström [17] the distribution of Mo(VI) and Mo(IV) is shown in Figure 2.9 [3].

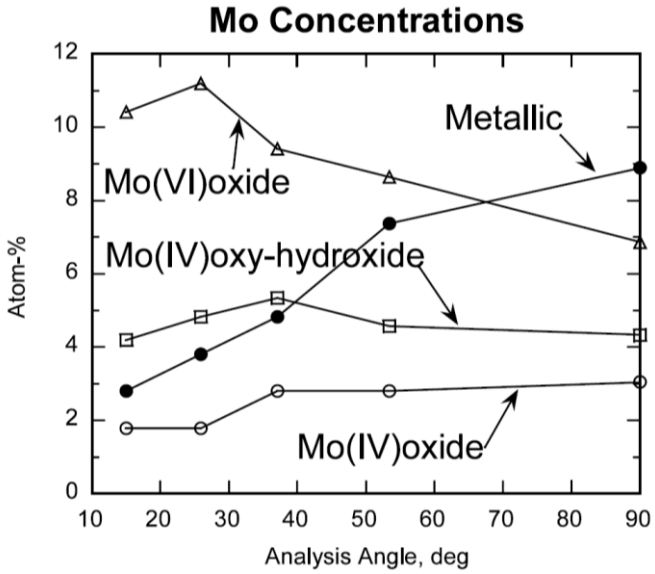

Figure 2.9: Concentration gradients in a passive film for molybdenum, recorded for a 6Mo superaustenitic stainless steel after immersion in ferric chloride solution using XPS, for angles close to grazing, there is a strong contribution of Mo(VI), whereas metallic Mo dominates for angles close to perpendicular, the Mo(IV) states show less angular dependence [3]

The beneficial effect of molybdenum in CRAs is explained by various models. Sugimoto and Sawada suggested that Mo(VI) forms a solid solution with CrOOH and inhibits transpassive dissolution [18]. Hashimoto et al. [19] came to the conclusion that MoO_2 forms an inner passive layer and the outer oxy-hydroxide acts as a diffusion barrier through the film. Earlier they proposed that active sites are inhibited to corrosion by deposition of molybdates or molybdenum oxy-hydroxides [20]. Ogawa et al. found that molybdate is formed as a secondary corrosion product from a dissolved molybdenum species [21]. Olefjord et al. have proposed that in an oxide film containing trivalent ions (Fe and Cr), there are point defects present (vacancies). The density of vacancies can be reduced by the presence of hexavalent and quadrivalent ions [22]. This has also been supported by Urquidi and MacDonald [23].

Concluding it is important to note that molybdenum alone without chromium being present in the alloy does not form truly passive layers that protect the alloy against pitting. Chromium in contradiction can maintain passivity on its own. The presence of chromium is absolutely necessary to maintain a passive layer, whose protective effect, however, can be further improved by alloying the material with molybdenum. Molybdenum, however, due to its high

melting point and due to its high density, tends to segregate and to form precipitates (carbides and/or intermetallic phases). Both locally reduce the resistance to pitting corrosion.

Tungsten has a very similar chemistry to molybdenum and it is claimed that tungsten behaves in the same way as molybdenum. The only difference seems to be its higher atomic weight so that a smaller beneficial effect of the heavier tungsten is obtained compared to molybdenum.

Nitrogen

As can be seen from equations (2) and (3) describing PREN/MARC, nitrogen improves pitting resistance of stainless steels 16 to 30 times more than chromium. The usefulness of nitrogen depends on several factors ranging from synergies between molybdenum and nitrogen, increase of solution pH in pits and general reduction of corrosion rates. It is considered that nitrogen might create ammonium ions that react with free chlorine to form chlorine species that are less effective oxidants in comparison to chloride ions, thus retarding autocatalytic reactions inside a pit [24] and helping repassivation inside the pit before it can propagate further. The other explanation for the beneficial effect of nitrogen is the formation of a nitride at the metal/film interface, which reduces the dissolution rates for individual elements such as iron [25] or nickel-molybdenum complexes [26,27].

Due to the decreasing pH inside a stable pit, it is expected for the pit to propagate until the surface layer is corroded widely enough to allow a wash-out of electrolyte, which will increase pH and decrease Cl^- content inside the pit and allow repassivation. Molybdenum, however, can form oxides even in very low pH solutions, allowing at least partial repassivation despite a decreasing pH value before the wash-out phenomenon takes place. Some sources argue that molybdenum may dissolve in the presence of ammonia and locally increase pH inside the pit and support repassivation in that way [24].

Nickel

Nickel is generally not found inside the passive layer due to its noble characteristic. Nickel is the most noble element found in stainless steel (among the main elements iron, chromium, nickel, molybdenum and manganese, the latter only in the case of CrMnN stainless steels). Nickel is enriched underneath the passive layer and forms the so-called interface ("apparent metal" in Figure 2.2). It is considered that nickel helps to retard the corrosion rate inside pits, allowing the bare stainless steel inside the pit to create a new passive layer and preventing further pit propagation. Nickel due to its nobility will result in a lower localized corrosion rate inside the pit that will result in a lower acidification rate and pH drop due to slower dissolution.

Therefore nickel is not found inside the equation used to calculate the PREN value. Nickel does not form oxy-hydroxides in low pH solutions and cannot contribute to passivation. A minor negative effect of nickel on MARC (equation (3) [13]) has only been reported by Speidel. A mechanistic explanation is not given for the small obtained effect. A negative factor of only -0.25 in MARC means a minor or even a negligible effect.

Manganese

Manganese increases tensile strength of stainless steels but at the same time it reduces their corrosion resistance. Manganese as an un-noble alloying element is enriched in the passive layer and yields to mixed (Fe,Cr,Mn)-oxides there. This has been found by Park and Kwon [28]. They describe the reduction of pitting potential for Fe-18Cr stainless steels with different Mn contents (Figure 2.10).

A second effect of manganese is that in stainless steels especially manganese sulfides but also manganese oxides are formed. These serve as local defects in passive layers and increase the susceptibility to pitting [29]. In addition to pit initiation, dissolution of manganese sulfide results in the formation of aggressive species inside the early pits. Dissolution can occur electrochemically and chemically. At open circuit potential the relevant reaction is [30]:

$$MnS + H^{+} \rightarrow Mn^{2+} + HS^{-} \qquad (4).$$

MnS inclusions have another detrimental effect that there is a crevice formation between the matrix and the inclusion during solidification from melting temperature [29]. Ryan et al. [31] claimed that MnS on top of all these effects dissolves chromium from the surrounding steel matrix during solidification and by this decreases the local PREN of the alloy just adjacent to the sulfide inclusion. With this the authors claimed that pitting resistance would be locally reduced and pit propagation is more likely to take place. The authors underline their hypothesis with FIB-SIMS analysis. The results could not be reproduced by other authors [32] and finally Ryan et al. withdrew their findings [33].

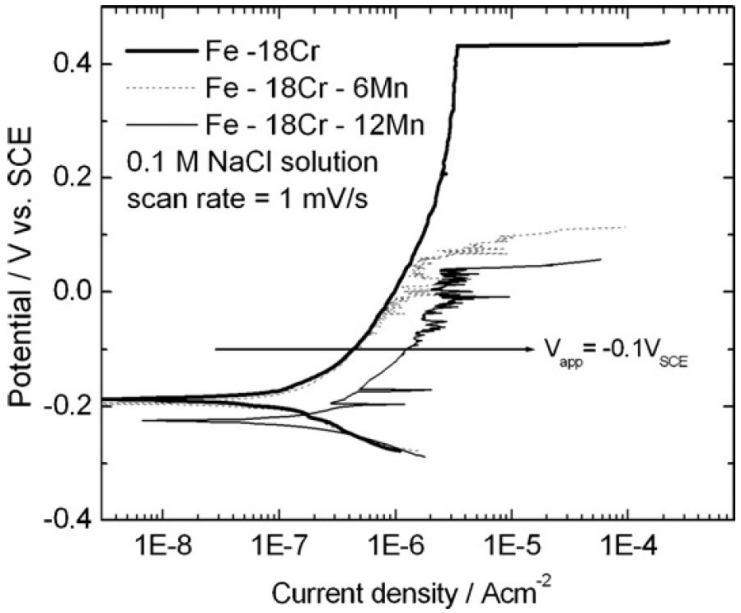

Figure 2.10: Effect of manganese on pitting behavior of Fe-18Cr stainless steels in current density potential measurements in 0.1 M NaCl [28]

2.2 Depassivation

Passive metals and alloys can suffer depassivation resulting in a sharp increase of corrosion rate. This may occur either locally (pitting corrosion) or across the entire surface (uniform corrosion). Passive corrosion current densities can vary widely across several orders of magnitude depending on alloy composition, electrolyte conditions, potential and time.

Iron in sodium phosphate solution reaches a corrosion current density in the passive state between 10^{-7} and 10^{-5} A/cm^2 (Figure 2.11 in [34]).

For Fe-Cr-Ni stainless steels in 2N H_2SO_4 solution Osozawa and Engell [35] have found corrosion current densities between 10^{-9} and 10^{-5} A/cm^2 at room temperature and between 10^{-7} and 10^{-5} A/cm^2 at 90 °C (Figure 2.12).

For pure aluminum and AlCuPbBi alloy 2011 in 0.3 % Na_2SO_4 solution Barbucci et al. report a passive corrosion current density between 10^{-6} and 10^{-5} A/cm^2 (Figure 2.13 [36]).

The most frequently used titanium alloy TiAl6V4 reaches a passive corrosion current density of 10^{-8} A/cm^2 after 400 h immersion in physiological salt solution at 37 °C [37]. Also niobium and tantalum reach similar levels of passivity between 10^{-9} and 10^{-5} A/cm^2 at 25 °C in 0.5 M NH_4HSO_4 at 0 V_{SCE} as function of stabilization time (between 10 and 10^5 s) [38].

Summing up, passive corrosion current densities are between 10^{-9} and 10^{-5} A/cm^2 depending on corrosion system and degree of healing of the passive layer.

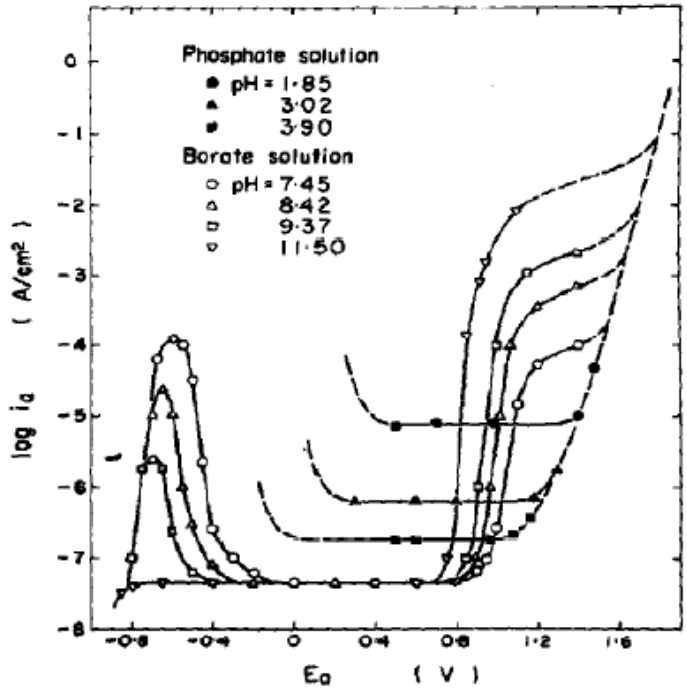

Figure 2.11: Stationary anodic polarization curve of iron in acidic, neutral and alkaline solutions at 25 °C under deaerated conditions pH 1.85 – 3.90: phosphate solution; pH 7.45 – 11.5: borate solution [34]

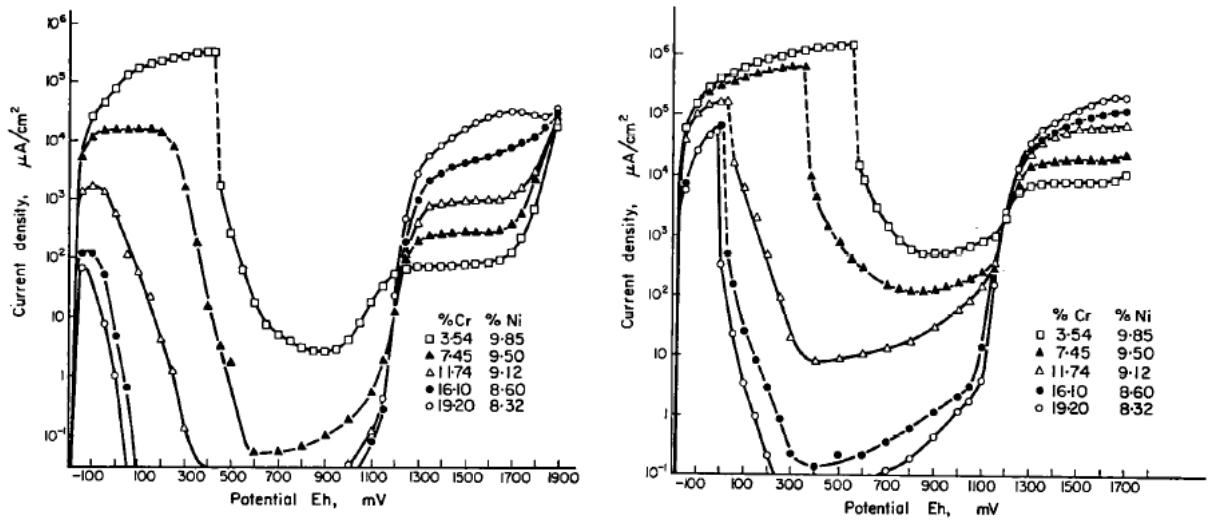

(a) (b)

Figure 2.12: Potential – current density curves of various stainless steels in 2 N H_2SO_4 at (a) 25 °C and (b) 90 °C [35]

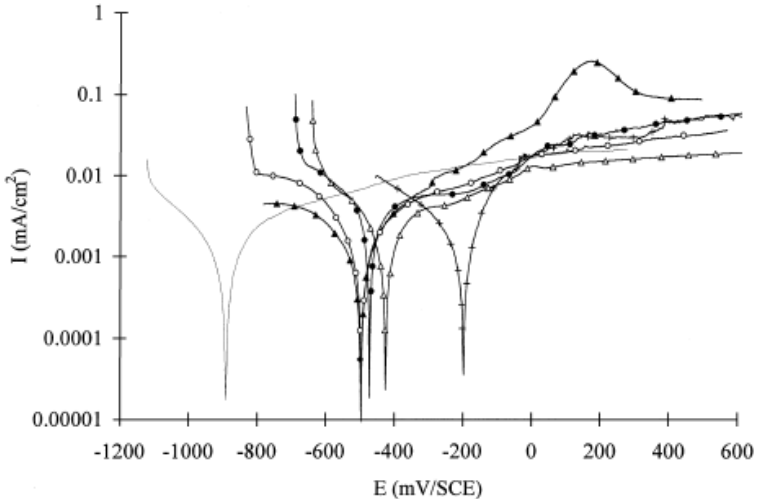

Figure 2.13: Anodic polarisations of the pure Al (grey), aluminum alloy 2011 (AlCu5.5Pb0.4Bi0.4, indicated with (+), Al98Cu2 (Δ), Al96Cu4 (▲), Al97,75Cu2Be0.25 (○) and Al97.5Cu2Be0.5 (●) in 0,3 % sodium sulphate at 25 °C [36]

The true passive behavior of the above mentioned metals differs to the so-called pseudopassive behavior that has been reported for cemented carbides [39-41]. There a cobalt or nickel binder that is not passive due to its nature but containing some dissolved W after sintering and retarding corrosive attack, shows higher corrosion current densities than true passive metals. Corrosion current densities in the pseudopassive range are between 10^{-4} and 10^{-2} A/cm^2 (Figure 2.14 [40]). These current densities can already be called active behavior, nevertheless in the polarization tests there is a sort of a passive behavior obtained (Figure 2.14).

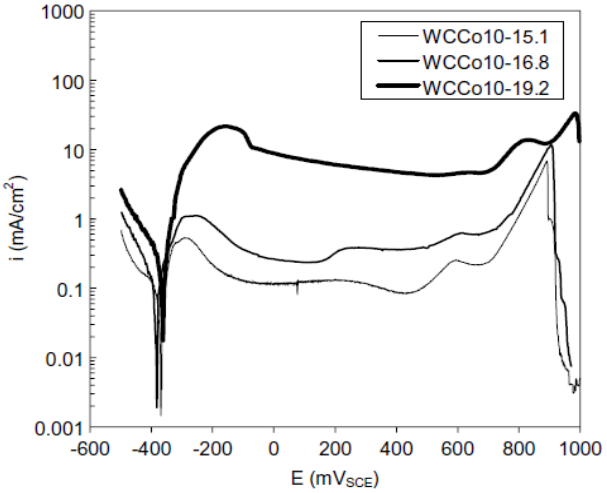

Figure 2.14: Polarization curves of WCCo10 cemented carbides in 1 N H_2SO_4 at 25 °C, "15.1" is equal to 39 % W in the binder phase, "16.8" is equal to 33 % W in the binder phase and "19.2" is equal to 18 % W in the binder phase [40]

Once a passive layer is formed on a metal or an alloy, depassivation can happen by various processes. Possibilities for localized depassivation are:

- Mechanical depassivation by impacting or scratching particles,
- chemical depassivation by aggressive ions, or
- structural depassivation by the presence of nonmetallic inclusions or precipitates.

In contradiction, general depassivation can take place:

- Chemically by highly aggressive conditions such as low pH or highly aggressive species; or
- mechanically by extensive wear distributing over large areas.

The consequence of depassivation is an increase of corrosion current density (locally or generally) by several orders of magnitude to the range of 10^{-5} to 10^{-3} A/cm^2. A corrosion current density of 10^{-4} A/cm^2 is for a divalent metal with a molar weight between 55 and 66 g/mol and a density between 7 and 9 g/cm^3 (valid for Fe, Co, Ni, Cu, Zn) equal to a corrosion rate of 1 mm/y according to Faraday's law.

Below, the different possibilities of depassivation are discussed.

2.2.1 Localized depassivation

Localized mechanical depassivation

Mechanical depassivation occurs as the oxide layer is removed due to a mechanical stress. These are limited to scratches, erosion due to impacting particles in a fluid, tearing as a result of mechanical constant or cyclic stresses and imploding gas bubbles during cavitation processes [42-49].

Characteristic for all these processes is that localized damage of the passive layer is generated and that the surrounding area is still passive, being more noble and serving as a cathode for anodic dissolution of the damaged area.

Due to this, a scratch test is often employed to study repassivation kinetics of metals in an electrolyte. The scratch test has the advantage of localized activation, which is the case under such conditions. Therefore scratching is a highly proper method to investigate such phenomena.

Localized chemical depassivation (pitting)

Localized chemical depassivation can be caused by an aggressive solution, which attacks the passive layer, breaking it down and not allowing instant repassivation. Local chemical depassivation occurs during pitting and crevice corrosion. Pits may be critical with other phenomena as well, e.g. mechanical loading, when a pit often serves as an initiation site for stress corrosion cracking or corrosion fatigue.

Pits may be introduced into the material in chloride electrolytes due to a chloride level above the threshold level, due to an increased temperature [50], due to material imperfections or locally increased solution aggressiveness as a result of occlusivity of the surface. The latter (flutes, grinding marks, surface roughness) will maintain a localized environment with less electrolyte exchange by convection. Consequently, high chloride containing local solutions will last longer and early pits are more likely to propagate in a metastable regime until they reach their stable regime. Other aggressive anions, such as thiosulfates may also cause pitting. Once a pit is nucleated, the bare metal at the damaged area of the passive layer begins to dissolve until saturation of metal ions is obtained. Then acidification by hydrolysis (reaction of metal ions with water form hydroxides plus hydronium ions) takes place and due to charge balance (high quantities of Me^{2+} and H^+ inside the early pit) negative ions are attracted to diffuse into the pit. Mainly Cl^- ions are able to enter due to their small size and high mobility. There is a potential gradient between the anodic pit and the vast cathodic surface surrounding the pit, which drives the negatively charged Cl^- ions into the pit and, together with the H^+ ions, forming HCl. A schematic with the paths of the involved ions is presented in Figure 2.15 [51].

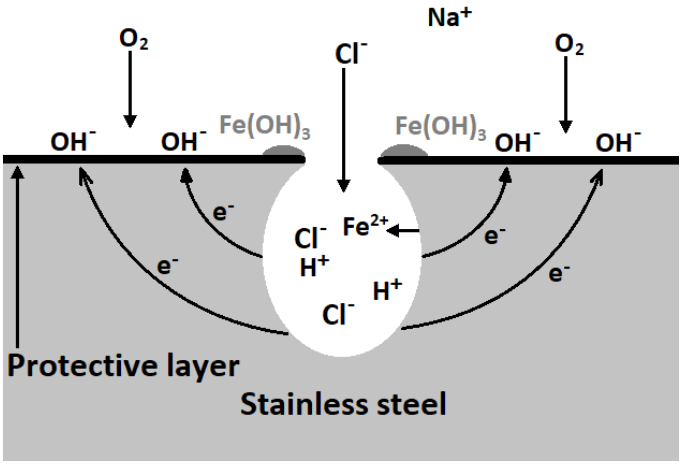

Figure 2.15: Reactions during stable pitting corrosion on stainless steels – redrawn from [51]

This mechanism causes a decrease of pH within the pit to further accelerate corrosion processes. Since the metal corrodes and dissolves much faster than the oxide layer, pits will

become deep and wide underneath the oxide layer. When the passive layer above the pit collapses or is dissolved, wash-out of electrolyte by exchange of the aggressive solution inside the pit with fresh electrolyte from outside can happen and the pit dies.

The most discussed part of the pitting phenomenon is pit nucleation itself, more specifically the breakdown of the passive layer. An important concept is the point defect model (PDM) proposed by Macdonald [52], which assumes both cations and anions may travel through the oxide layer by means of diffusion. More importantly, it also assumes defects are formed at either end of the passive film and travel through it. Anions (oxygen ions) thus may diffuse towards the metal, which thickens the oxide layer, while cations (metal) diffuse towards the outer surface. Their dissolution will result in thinning of the layer.

Once certain ions such as hydrated chlorides are adsorbed to the surface they will introduce cation vacancies into the metal. These vacancies will start to diffuse towards the metal/oxide interface since metal ions are generated there and diffuse via cation vacancies outwards. When the cation vacancies reach the metal/oxide interface, vacancy condensation and subsequent local film detachment will take place, leading to void formation. As the now detached film is subjected to mechanical stress and further dissolution, it breaks, which becomes an initiation site for a pit (Figure 2.16 [52]).

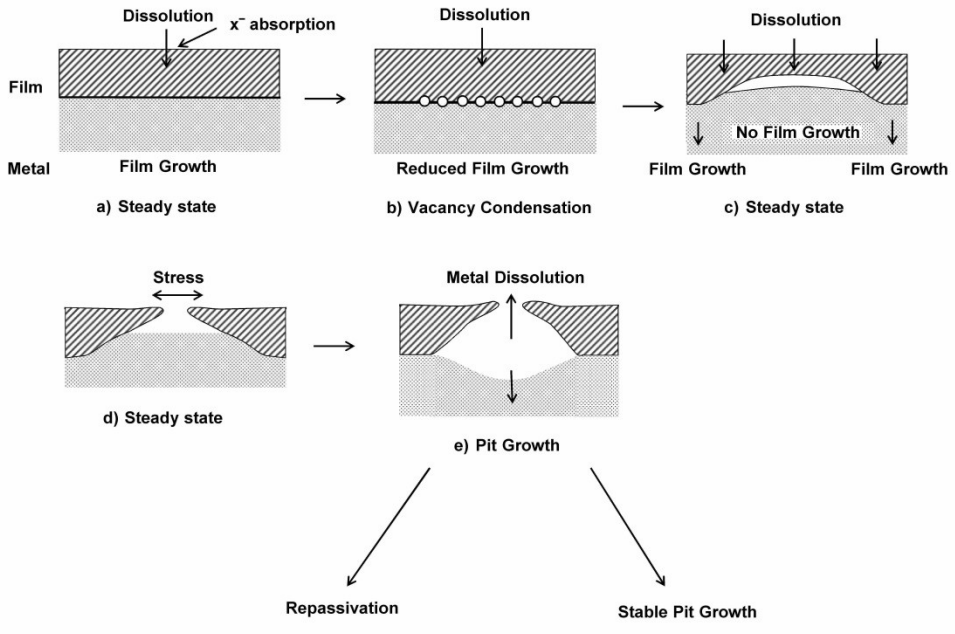

Figure 2.16: Schematic of pit formation [52]

The question, as to why especially chloride ions are so efficient to produce many cation vacancies, is answered by the author of the PDM model with the explanation that chloride ions might fit best into oxygen vacancies. It is postulated that Gibbs energy for such an adsorption is composed of two principal components, the dehydration energy and the energy required to expand the vacancy, to accommodate the ion. In the series of halides F^-, Cl^-, Br^- and I^-, the F^- ion has the highest dehydration energy and the I^- ion has the largest ion radius. Calculations by the author indicate that Cl^- have the lowest total energy to absorb in an oxygen vacancy in NiO. In titanium oxide, however, Br^- has a lower pitting potential than Cl^- ions. So understanding the size of oxygen vacancies would be very important to achieve a deeper understanding.

The model does not fully explain, why such an initiation site does not form a new passive film instantly as solution comes into contact with the bare metal found underneath the oxide film.

Other notable theories are the ion penetration theory, the adsorption theory and film breakdown theory [53]:

The ion penetration theory [54] assumes that Cl^- ions penetrate the passive film due to their small diameter, locally destroy the passive layer and cause pit nucleation there, however it does not explain the reason why other ions such as SO_4^{2-} cause pitting, despite their larger size. Burstein et al. [54] conclude that the pitting process consists of 4 steps:

1. Chloride migration through the passive layer in a violent event,
2. Embryonic pit propagation through the formation of a locally saturated salt solution
3. Metastable pit growth where washout of the saturated chloride solution is hindered by geometry of the site and its occlusivity,
4. Stable pit propagation, when the pit is stabilized by its own size and shape and more chloride diffuses into the pit due to acidification.

The adsorption theory states that in certain places Cl^- ions are adsorbed instead of O^{2-} ions after film removal due to aggressive anions, forming metal salts and resulting in the initiation of pits. The issue with this theory is that the displacement of the more negatively charged O^{2-} ions by the less negatively charged Cl^- ions should be theoretically favored by a negative potential shift and not a positive one, which is contrary to what the adsorption theory suggests.

The film breakdown theory suggests that a large concentration of aggressive anions in the bulk solution causes the adsorption of a salt layer, which leads to pit nucleation, somewhat similar to the adsorption theory. It however adds the condition of a critical concentration of the aggressive anions required to initiate pitting, which has been experimentally shown. While there is some merit to this theory it suffers from similar drawbacks as the adsorption theory.

Localized structural depassivation by nonmetallic inclusions and precipitates

Certain materials are subjected to local depassivation due to inclusions or precipitates. At such particles the passive layer is severely damaged (often thinned), has a different composition or is even unable to form.

Burstein et al. [54] show the effect of pitting events in stainless steels as function of time in comparison to titanium (Figure 2.17). Stainless steels containing non-metallic inclusions (manganese sulfides) show in many identical runs a decay of pit nucleation events. This is connected to the sulfide inclusions at the surface that dissolve into the electrolyte, generating early pits and even forming aggressive species (see equation 4). When the sulfides have been dissolved no new pits are introduced. In case of titanium, which does not contain non-metallic inclusions, the frequency of nucleation events is increasing with time and this can be attributed to the chloride ions penetrating the passive layer and initiating early pits.

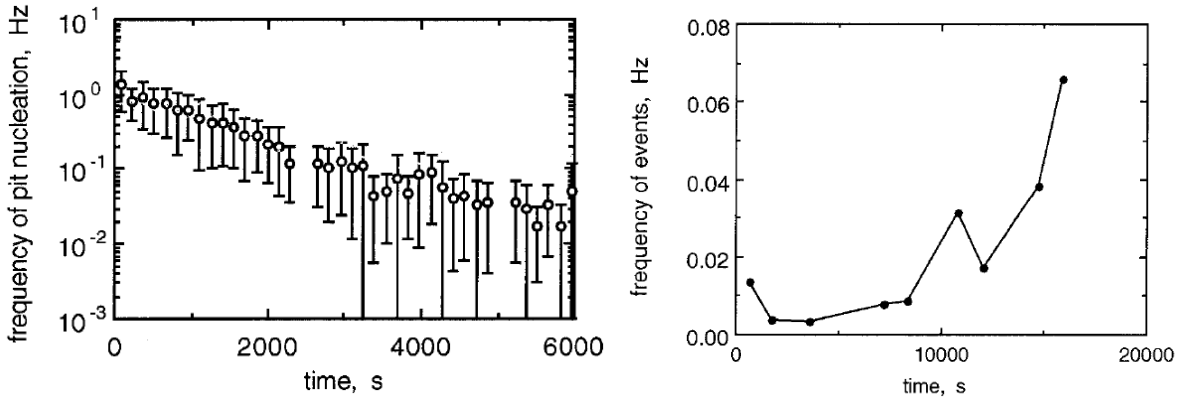

(a) (b)

Figure 2.17: Frequency of nucleation of corrosion pits as a function of time of polarization; (a) stainless steel 304L in 0.025 M HCl and 0.075 M $HClO_4$ at 0.2 V_{SCE}, (b) commercially pure titanium in 1.5 M HCl at 0.5 V_{SCE} [54]

Manganese sulfides are special in the respect that they are soluble on the one side and form aggressive species on the other side. So this type of inclusion/precipitate is the most critical for materials. Less critical are soluble precipitates that do not form aggressive species (e.g. $MgZn_2$ in aluminum alloys) and insoluble inclusions (e.g. oxide inclusions in steels) or precipitates (e.g. TiC in steels). The latter precipitates can however have additional detrimental effects such as depletion of a passivating element (e.g. $Cr_{23}C_6$ with chromium depleted zones in stainless steels) or a galvanic effect (e.g. Al_2Cu is a strong cathode in aluminum alloys).

2.2.2 General depassivation

General chemical depassivation by highly aggressive species

Complete breakdown of the passive layer can occur when highly aggressive species are in direct contact with the passive material and dissolve the passive layer. The most common example of such a breakdown is a high concentration of H^+ ions (low pH), which simply increases the dissolution rate of the oxide layer to the point that it cannot regrow quickly enough. Once the film is completely dissolved, the underlying metal dissolves at an even higher rate.

An example from practice are acidizing jobs in oil and gas production. Due to plugging by limestone, production can rapidly decrease and reach almost zero, meaning a complete plug of the borehole. This is mainly due to the fact that under changing pressures dissolved Ca^{2+} ions together with dissolved CO_2 precipitate as $CaCO_3$ and plug the flow of hydrocarbons to the well. In such cases concentrated HCl (37 %) is pumped downhole to dissolve the precipitated limestone. The pH of solution is below 0 and since stainless steels depassivate below pH 4 according to the Pourbaix diagram of chromium (Figure 2.4 (b)), steels become active and high corrosion rates take place.

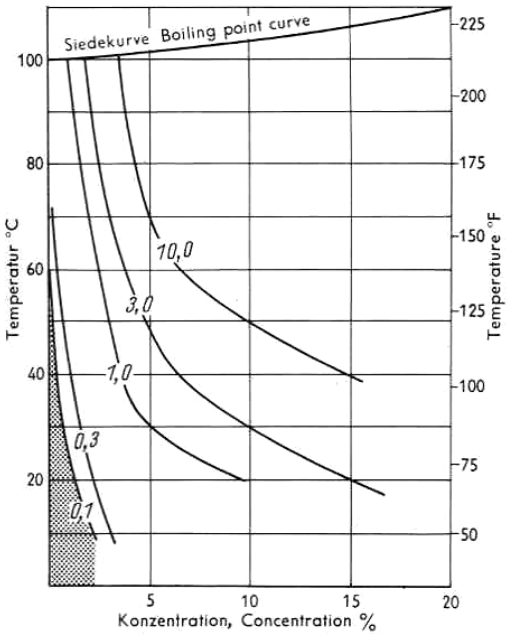

Figure 2.18: Corrosion rates of stainless steel 316 (1.4401, X5CrNiMo17-12-2) in HCl as function of temperature and HCl concentration, numbers at lines represent corrosion rates in [mm/y] [55]

Corrosion rate of a stainless steel 316 (1.4401, X5CrNiMo17-12-2) in HCl can be seen in Figure 2.18 as function of temperature and HCl concentration. At room temperature in concentrated HCl, a corrosion rate of ca. 10 mm/y is obtained [55].

It is unclear, whether and at which pH the passive layer may be rebuilt once the solution becomes less aggressive. In acidizing jobs the acid that has been pumped downhole is, after a certain retention time, produced out of the reservoir and is continually diluted with brine from the reservoir. Consequently the pH of the produced solution will rise constantly after acidizing has been finished until it reaches the original pH of the brine of the well (in equilibrium with the gas that is produced).

The other option for general chemical depassivation is a combination of low pH and aggressive ions, causing a stable corrosion product film with less protective properties (e.g. a sulfide or a carbonate). This film may then prevent oxygen from reaching the thinned oxide layer, which causes an increased corrosion rate. While such a corrosion product film will provide some protection, it is less protective than a true passive layer. Such films of corrosion products often contain many defects like vacancies, cracks and inclusions of electrolyte.

General mechanical depassivation by extensive wear and/or erosion

By extensive mechanical loads (wear or erosion) a uniform depassivation can occur. Not only is the passive layer scrubbed away, additionally cold deformation is introduced into the metal resulting in a higher dislocation density and therefore in general in a more active metal. In addition the corrosion rate of bare metal is usually higher than the rate of dissolution of a protective (or non-protective) layer. Any layer of corrosion product, regardless of whether it is highly protective or not, is more noble than the metal itself and will in most cases have a lower corrosion rate than the metal itself. Consequently a combined chemo-mechanical attack will result in an accelerated attack of the metal.

Neville has investigated with several co-authors the phenomenon of synergistic effects between a mechanical and a chemical attack on passive metals. In their work [56] they described the total weight loss under such conditions as the sum of a mechanical degradation, the corrosive attack and a synergy effect (equation 5):

$$TWL = E + C + S \quad (5),$$

where TWL is the total weight loss, E is the weight loss due to erosion, C is the weight loss due to corrosion and S is the weight loss due to synergy effects between erosion and corrosion. This means that due to the synergy effects the damage of a combined chemo-mechanical load

is higher than the sum of the damages that happen by a single corrosive and a single erosive attack.

In [57] they have split up the WL_S term to two synergy sub terms. The one is due to corrosion that is accelerating erosion by attacking elevated and cold deformed areas at the metal surface. The second subterm is connected to erosion accelerating corrosion, when sand particles collide with the surface consisting of loose corrosion products and result in spalling of these corrosion products (equation 6).

$$TWL = E + C + \Delta E_C + \Delta C_E \quad (6),$$

with ΔC_E being the increase of corrosive attack due to the presence of erosion and ΔE_C representing the contribution of erosive mass loss due to corrosive attack.

While they investigated stainless steels in a 3.5 M NaCl solution in a submerged liquid-solid jet with sand (grain size of grains mostly between 100 and 425 µm) [58] they found out that for superaustenitic stainless steels the mass loss is dominated by erosion (83 – 95 %), and that the synergy effects contribute up to 12 % of weight loss. Pure corrosive attack was always less than 4 % of the total weight loss.

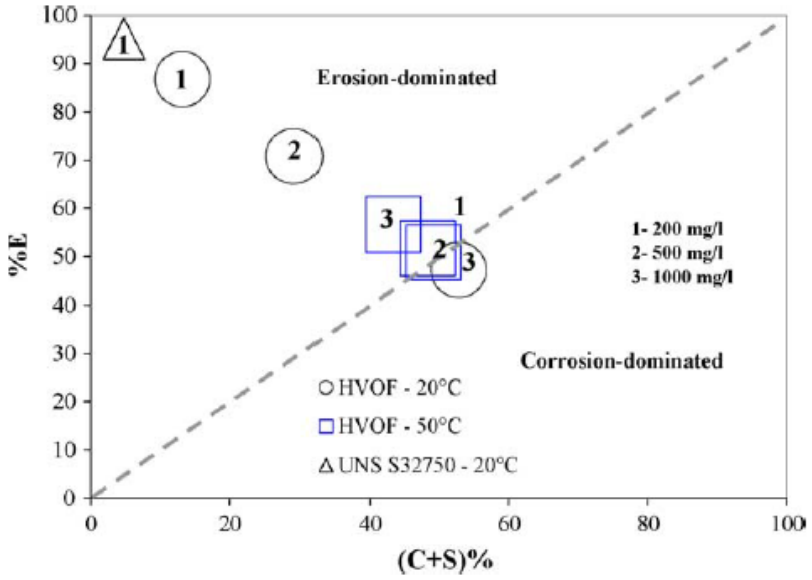

Figure 2.19: Material degradation regimes of HVOF WC-Co-Cr and of superaustenitic stainless steel S32750 in 3.5 % NaCl, numbers 1-3 indicate the mg/l solids (sand particles) in the slurry [59]

The data of passive materials that are simultaneously damaged mechanically by erosion and chemically by corrosion can be shown by material degradation regimes. There, the chemical attack including the synergy effect is drawn on x-axis and the mechanical on the y-axis [59]. A superaustenitic stainless steel (S32750) is clearly mainly mechanically damaged. No

substantial corrosive attack was observed on S32750 steel (Figure 2.19 [59]). For a WC-Co-Cr cemented carbide with a passive layer formed from Cr and W dissolved in the binder phase a 70 % lower degradation rate was obtained. The damage regime changed more towards the corrosive attack in Figure 2.19 since the cemented carbides exhibits a hardness of 1569 HV compared to 318 HV for the stainless steel and its corrosion resistance is somewhat lower when compared to the superaustenite.

2.3 Kinetics of passive layer formation / of repassivation

Once a passivating metal is exposed to oxygen it combines to form a monolayer of metal oxides. This oxidation process is thermodynamically favored and happens very quickly. The monolayer, just as the thick passive film already discussed, works as a semiconductor, decreasing the speed of cation and/or anion transfer through the layer.

When considering anions diffusing through the film then oxygen is moved toward the bulk metal, as new oxygen is first adsorbed and then absorbed into the surface. This process repeats itself, until the passive film reaches a maximum thickness. This means that as the film thickens an increasing diffusion path has to be overcome, consequently reducing the oxidation rate. Once the oxide dissolution speed is equal to the speed at which the oxide film is thickening a steady state is achieved and the film thickness no longer changes.

On the one side metal cations may diffuse through the film outward and on the other side oxygen anions diffuse inwards. The faster process will determine, where the passive layer grows – anion transfer implies, it grows at the metal/film interface, while cation transfer implies growth at the film/electrolyte interface. Both of these mechanisms require a driving force as otherwise neither anion nor cation would move from the thermodynamically favorable metal oxide bond. The driving force behind this movement is considered to be the different electrochemical potentials at the metal/film interface and the film/electrolyte interface (Figure 2.20 [1]).

Different authors consider different processes to be rate determining, the ion transfer through the oxide layer due to the electric field, the phase reaction at the metal/film interface or even the phase reaction at the film/electrolyte interface.

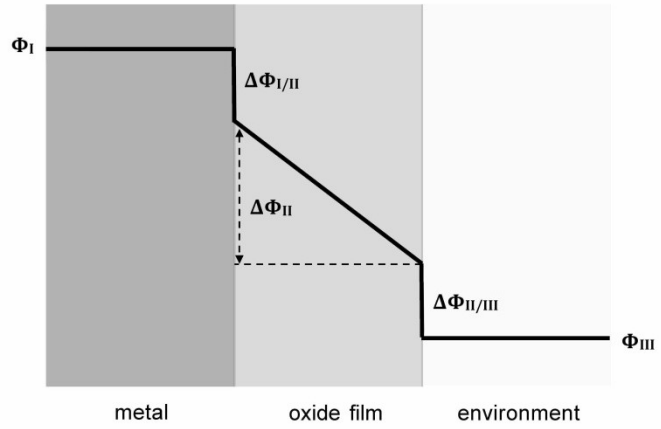

Figure 2.20: Schematic representation of the potential drop across a metal/passive film/environment system [1]

Some authors claim that non-stoichiometric oxides caused by ions moving through the oxide produces a buildup of space charges [1]. Regardless of what the rate limiting step is, the same equation can be used to represent or approximate the current density (and thus oxidation rate) of the metal:

$$i = A \cdot \exp(ß \cdot Fo) \quad (7),$$

where A and ß are constants and Fo is the electric field strength over the oxide. Since the electric field strength is defined as the potential drop divided with the distance (or film thickness), this results in the inverse logarithmic growth law, represented by equation 8:

$$1/x = A - B \cdot \log(t) \quad (8),$$

where A and B are constants, x is the film thickness and t is time. The equation defines the film thickening in a relation to time, however it does not take into account the dissolution speed of the film. This is unfortunately very difficult to take into account, as it depends on several different factors, ranging from the alloying elements in the steel to the solution. In a low pH solution we can initially expect iron oxy-hydroxides to be dissolved from the surface of a still-passivating film, increasing the chromium oxy-hydroxide concentration. Later on however, as the film thickens, we need to take into account the time required for cations to travel through the passive film, where they can enrich in one region (for example nickel in the metal/oxide layer interface) or dissolve in another (more iron at the oxide layer/electrolyte interface). Thus it is expected that the amount of alloying elements has a very large effect on the oxide dissolution rate both initially and over time but cannot be easily quantified.

In the following a stainless steel that cannot repassivate quickly in its environment (meaning it has a high dissolution rate compared to the film formation rate) and starting with a passive layer is assumed. Once the passive film is locally damaged, it will become a strong anodic spot, driving the potential of the entire sample/part to lower values, while emitting a large amount of current as corrosion reactions take place. The area close to the exposed metal becomes a strong cathode, while the area further away is less cathodic. Initially one can expect dissolution of iron at the exposed bare metal surface, which produces electrons according to the anodic reaction:

$$Fe \rightarrow Fe^{2+} + 2\ e^- \quad (9).$$

Subsequently, the solution will locally become increasingly more saturated with dissolved metal ions, slowing down further dissolution considerably and promoting film formation instead. The electrons will flow from the anode to the strong cathodic area surrounding the exposed metal, where they are discharged according to reaction 10 and locally increase the solution pH during the reaction.

$$½\ O_2 + H_2O + 2\ e^- \rightarrow 2\ OH^- \quad (10).$$

The combination of an abundance of dissolved iron ions and OH^- at the cathodic site will likely form $Fe(OH)_3$ at the cathodic sites, a phenomenon sometimes called rouging. Since the iron is mostly dissolved from the surface a thin passive film comprised mostly of chromium oxy-hydroxides is then formed at the anodic site, which begins repassivating. If we consider that same case with the addition of chloride ions in the solution, it is considered that the strong anode may attract the negatively charged Cl^-. This results in a locally lowered pH at the anodic site due to reaction 11:

$$FeCl_2 + 2\ H_2O \rightarrow Fe(OH)_2 + 2\ HCl \quad (11).$$

This may cause that the thin chromium oxide/hydroxide is not stable and also dissolves. If we now further imagine some flow of the solution taking place, there is no large buildup of iron ions at the anodic site preventing further iron dissolution, further increasing dissolution speed. At the same time, flow would mean that some of the OH^- ions are transported to the anodic site, thus increasing the pH there. Naturally there is never pure film formation or pure dissolution taking place during repassivation but a mix of both at different rates. Unfortunately, despite many studies in the field of repassivation kinetics, it is still impossible to quantify the effect of everything which might affect the ability of repassivation or the speed at which it will occur.

Kinetic studies on repassivation are most often evaluated with the following equations 12 to 15 [60,61] based on the relation found by Stern [62]:

$$i(t) = a \cdot t^{-\alpha} \quad \text{or} \quad \log i(t) = -\alpha \cdot \log t + k \tag{12}$$

i(t) is the current density at time t after scratching, α is the current decay gradient with a constant value for a given corrosion system (metal/environment system), a and k are constants related to the oxidation rate of the bare metal surface. The higher α is, the higher is the repassivation rate. Additionally one can write:

$$i(t) = A \cdot \exp[BV/h(t)] \tag{13},$$

A and B are associated with the activation energy for mobile ion migration, V is the potential drop across the oxide film and h(t) is the thickness of the oxide film.

While:

$$q(t) = zF\rho \cdot h(t)/M \tag{14},$$

where z is the number of involved electrons, F is the Faraday constant, ρ is the film density, M the molecular mass of the film and q(t) is the integral of current over time (charge at time t), it follows:

$$\log i(t) = \log A + BVzF\rho/2.3Mq(t) = \log A + cBV/q(t) \tag{15}.$$

According to this equation there is a linear relation between log i(t) and 1/q(t) with a slope of cBV where c is $zF\rho/2.3M$. The equation has been proposed by Marshall and Burstein [60] in 1984. Figure 2.21 shows the linear relation between log i(t) and 1/q(t) in a schematic. From the slope of the line Kwon et al derive the type of corrosion that appears to a wide range (Figure 2.21).

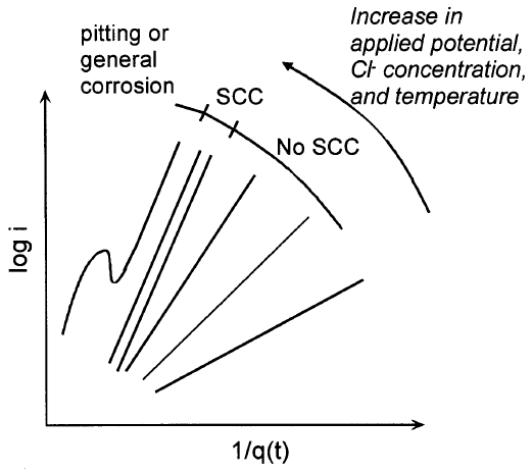

Figure 2.21: Schematic log i(t) vs 1/q(t) plots representing the relationship between the change in cBV and different types of corrosion [61,63]

Repassivation kinetics depends mostly on the ability of the metal to form a native passive layer, meaning that metals which have a good resistance to pitting should also be able to repassivate well. It is unknown whether the PREN value may be directly correlated to repassivation kinetics.

In the following literature, data on repassivation kinetics for several passive materials and alloys are reviewed, namely for:

- stainless steels,
- aluminum alloys,
- titanium alloys, and
- other passive alloys,

with the aim to present different investigation methods and ways of presenting results.

2.3.1 Repassivation data on stainless steels

Kwon et al. [61] have investigated susceptibility of stainless steel 304 in 4 M NaCl at 50 °C by scratching the material at different potentials. Figure 2.22 shows that an increasingly positive potential results in a slower repassivation. At -110 and -10 mV_{SCE}, who are both near to the pitting potential (-54 mV_{SCE}) the conditions for passive film formation are unfavourable and the passive layer allows a rather high corrosion current density (Figure 2.22 (a) and (b)). In Figure 2.22 (c) it can be seen that the current density remains high and moves towards very small 1/q(t) values (high q(t) indicates a large amount of dissolution).

Repassivation is strongly hindered near the pitting potential, which can be seen in Figure 2.22 (b) as horizontal lines at higher current densities between 10^{-1} and 1 A/cm^2. At lower potentials, repassivation happens within 10^{-2} and 10^{-1} s, while the current density decreases to 10 mA/cm^2 or lower. It has to be mentioned that the authors only did very fast measurements that resulted in rather high current densities after "repassivation". True repassivation shall reach current densities that have been mentioned above as passive current densities. The authors found a certain range of cBV values, where stress corrosion cracking occurred close to conditions, where repassivation is no longer possible.

In [63] the same group investigated ferritic stainless steels and found a similar time dependence in 1 M $MgCl_2$ at 50 °C and -300 mV_{SCE} (10^{-2} A/cm^2 at 0.1 s after the scratch).

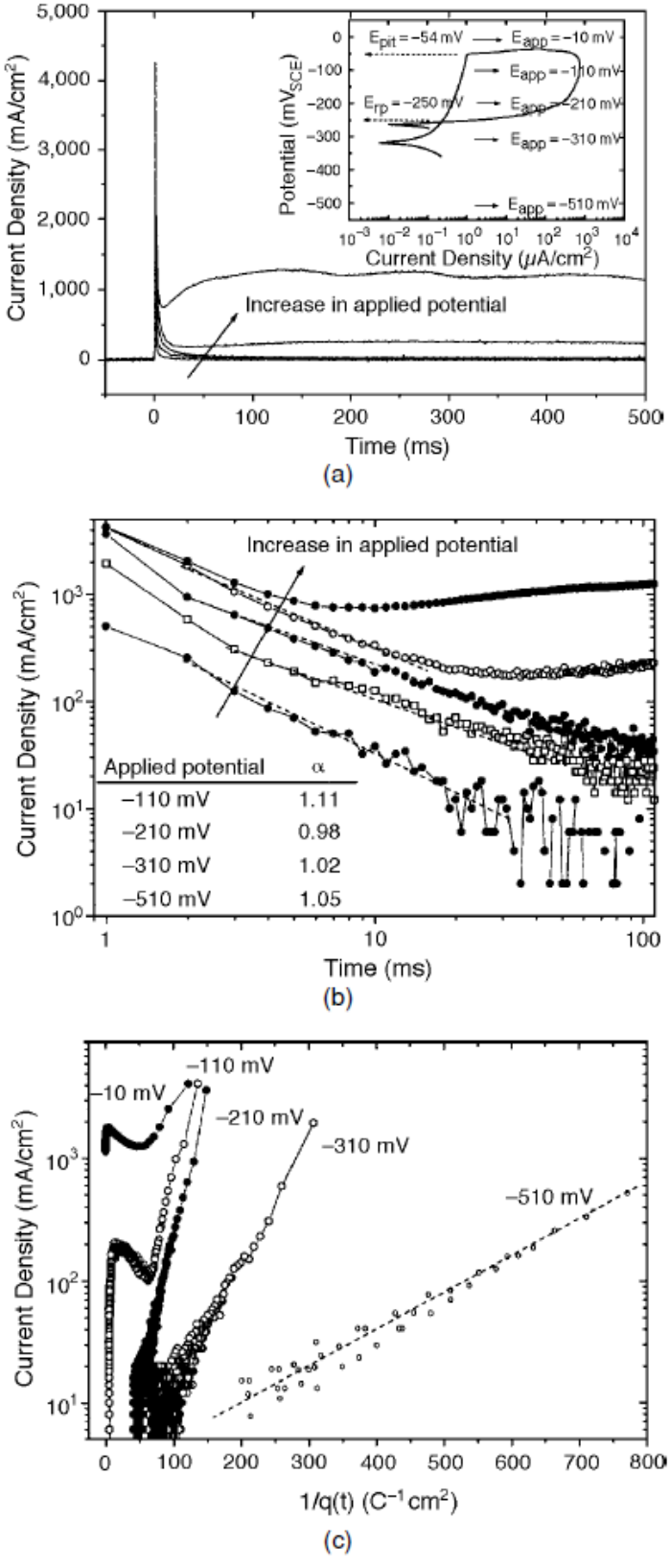

Figure 2.22: (a) Effects of applied potential on the current transient on scratched surface of stainless steel 304 in deaerated 4 M NaCl at 50 °C, (b) log i(t) vs log t plots and (c) log i(t) vs 1/q(t) plots [61]

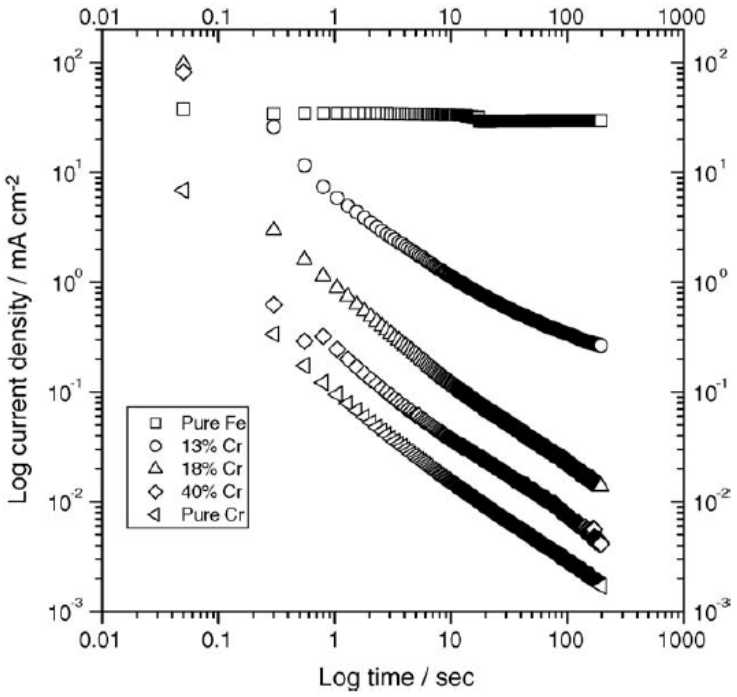

Figure 2.23: Decay of current density with time during repassivation of Fe-Cr alloys in deaerated 0.1 N H_2SO_4 at -0.25 V_{SCE} [64]

Lee [64] has investigated repassivation of Fe-Cr and Fe-Cr-Mo alloys in sulfuric acid solutions with and without Cl^- ions. He did his tests with an electrode that was grinded in the electrolyte by abrasive paper. His systematic variation of alloying elements shows that an addition of chromium improves kinetics of repassivation. After 200 s of repassivation time much lower current densities were reached when compared to the shorter times of Kwon and co-authors [61,63]. Within the first 200 s current density values are reduced to between 10^{-6} and 10^{-4} A/cm^2 for chromium contents of 18 % and higher (Figure 2.23 [64]). A value between 10^{-6} and 10^{-5} A/cm^2 for CrNi austenitic stainless steel 304 has also been obtained by Carranza and Galvele in 0.5 M Na_2SO_4 with the fast strain rate technique, where they strained a wire by 10 % at a strain rate of 10 s^{-1}, within 10^{-2} s. [65].

In Figure 2.24 [64] Lee showed the influence of molybdenum on repassivation kinetics. It turned out that in chloride free electrolyte there is a rather small effect on repassivation kinetics. In a 0.6 M NaCl containing sulfuric acid electrolyte 1 % of Mo addition already decreased corrosion current after 200 s by almost an order of magnitude from $3 \cdot 10^{-4}$ to $3 \cdot 10^{-5}$ A/cm^2. An increase in molybdenum content did not yield a significant additional reduction of the corrosion current density in the tested conditions.

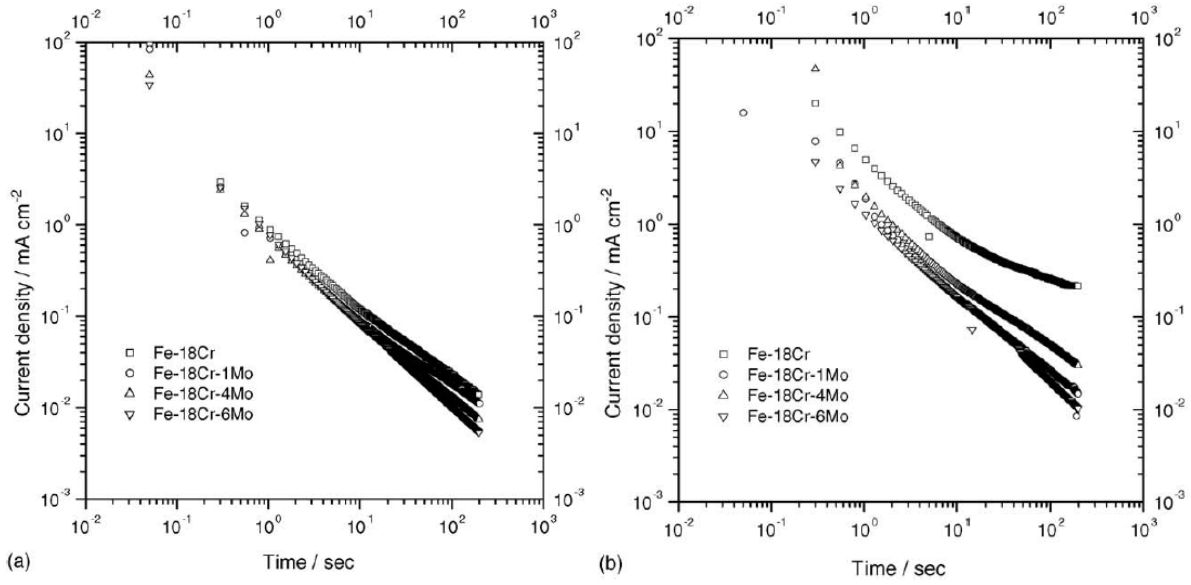

Figure 2.24: Decay of current density with time during repassivation of Fe-Cr-xMo alloys (x = 0, 1, 4, 6) at -0.25 V_{SCE} in deaerated (a) 0.1 N H_2SO_4 and (b) 0.1 N H_2SO_4 + 0,6 N NaCl [64]

Burstein and Sasaki [66] have investigated stainless steel 304L in 0.44 M Na_2SO_4 and in 0.6 M NaCl solution at a potentiostatic potential of 0.40 V_{SCE}. Repassivation kinetics are shown for both solutions in Figure 2.25. Tests were done at room temperature. Their guillotined stainless steel wire had a total area of $1.23 \cdot 10^{-4}$ cm^2.

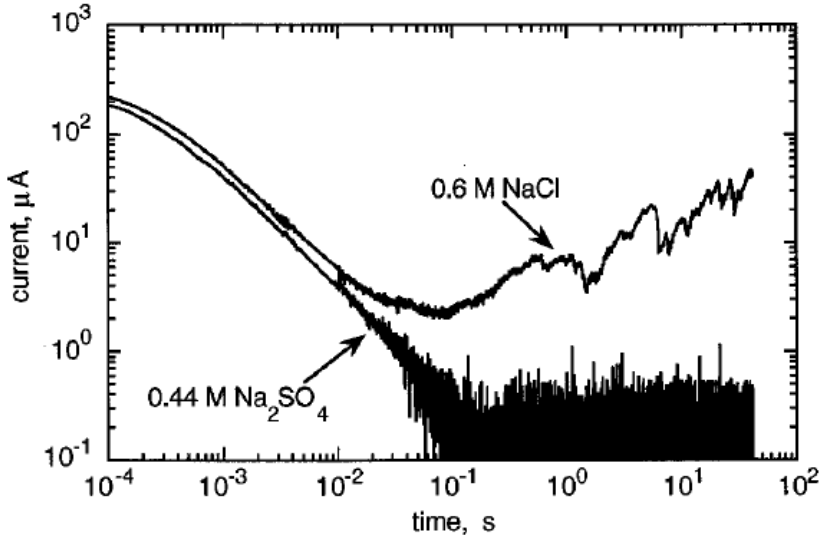

Figure 2.25: Potentiostatic current transients due to guillotined 304L at 0.40 V_{SCE} in 0.44 N Na_2SO_4 and 0.6 M NaCl [66]

Material 304L showed a corrosion current density in the sulfate solution of 10^{-3} A/cm^2 after 0.1 s (10^{-7}/1.23·10^{-4} A/cm^2). In contradiction in the chloride electrolyte no full repassivation took place, and the corrosion current density maintained high at 10^{-1} A/cm^2 with a tendency to increase further (Figure 2.25 [66]).

2.3.2 Repassivation data on aluminum alloys

Frankel et al. investigated repassivation of aluminum with the breaking electrode cell [67]. Sputtered pure aluminium with a total area of 9.5·10^{-6} cm^2 was broken in a 1 N K_2SO_4 solution at 0 V_{MSE} equal to 0.458 mV_{SCE} (MSE – mercury sulphate electrode with a potential of 0.679 V_{SHE} or 0.438 V_{SCE}). Figure 2.26 shows the current vs time behaviour of this test.

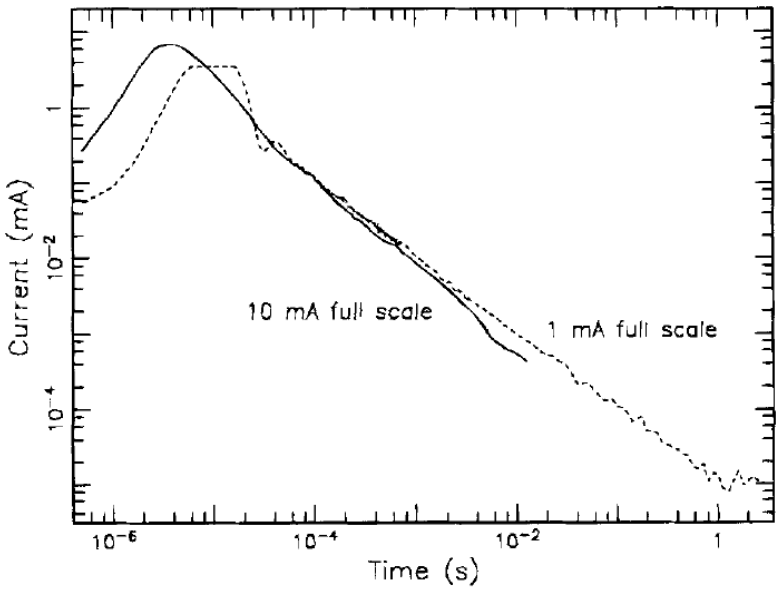

Figure 2.26: Potentiostatic current transients of ruptured aluminum at 0.458 V_{SCE} in 1 N K_2SO_4 [67]

A current of 10^{-5} mA is equal to a current density of approximately 0.1 A/cm^2 (10^{-8}/9.5·10^{-6} A/cm^2) one second after depassivation. This seems to be a rather high value for the current density especially when comparing it with stainless steels.

Wloka, Hack and Virtanen [68] performed scratch tests on various aluminium alloys in media with different pH values. The pH was adjusted by adding either HCl or NaOH. They chose a different way of evaluation. During scratching under potentiostatic conditions a potential transient and a current transient is formed that fades out when repassivation occurs. The authors took as repassivation time the time interval that was found to reduce these transients

to 10 % of their peak value. Figure 2.27 shows the repassivation times of the investigated alloys at various pH values.

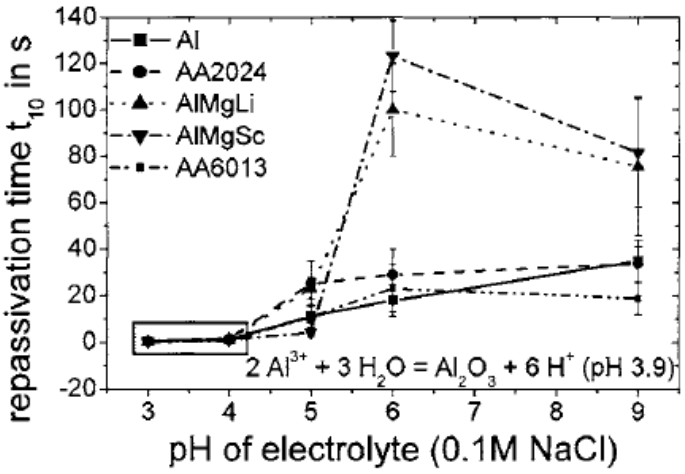

Figure 2.27: Repassivations times of various aluminum alloys in 0.1 M NaCl as function of pH, repassivation time t_{10} means that transients declined to 10 % of their peak value [68]

Repassivation happens within some 20 s for pure Al and for conventional alloys such as AlCu5.5Mg1.5Mn0.6 (AA2024) and AlMg1Si1Cu1Mn0.6 (AA6013). When investigating the alloys containing Li and Sc the authors report significantly longer repassivation times at pH 6 and 9, where the repassivation times were between 80 and 120 s. The slightly acidic conditions result in fast repassivation for all alloys, while the more alkaline conditions result in slower repassivation. Below pH 4 no repassivation was obtained which is in good agreement with the general passive behavior of aluminum according to the Pourbaix diagram.

The most comprehensive study on repassivation kinetics of aluminium and its alloys has been done by Madden et al. [69]. They investigated pure aluminium, alloy 7075 and alloy 2024 by use of the scratch method.

The latter two alloys were peak aged in the condition T6. Figure 2.28 (a) shows that for repassivation of Al99.999 in 1 M NaCl a potential of -0.8 V_{SCE} is necessary. At more oxidising potentials activity is maintained. At lower concentrations of chloride in Figure 2.28 (b) repassivation can occur up to potentials as low as -0.7 V_{SCE}. Repassivation occurs for pure Al99.999 within a few tenths of a second. Within this time a corrosion current density between 10^{-2} and 10^{-1} A/cm^2 is reached after starting at some A/cm^2.

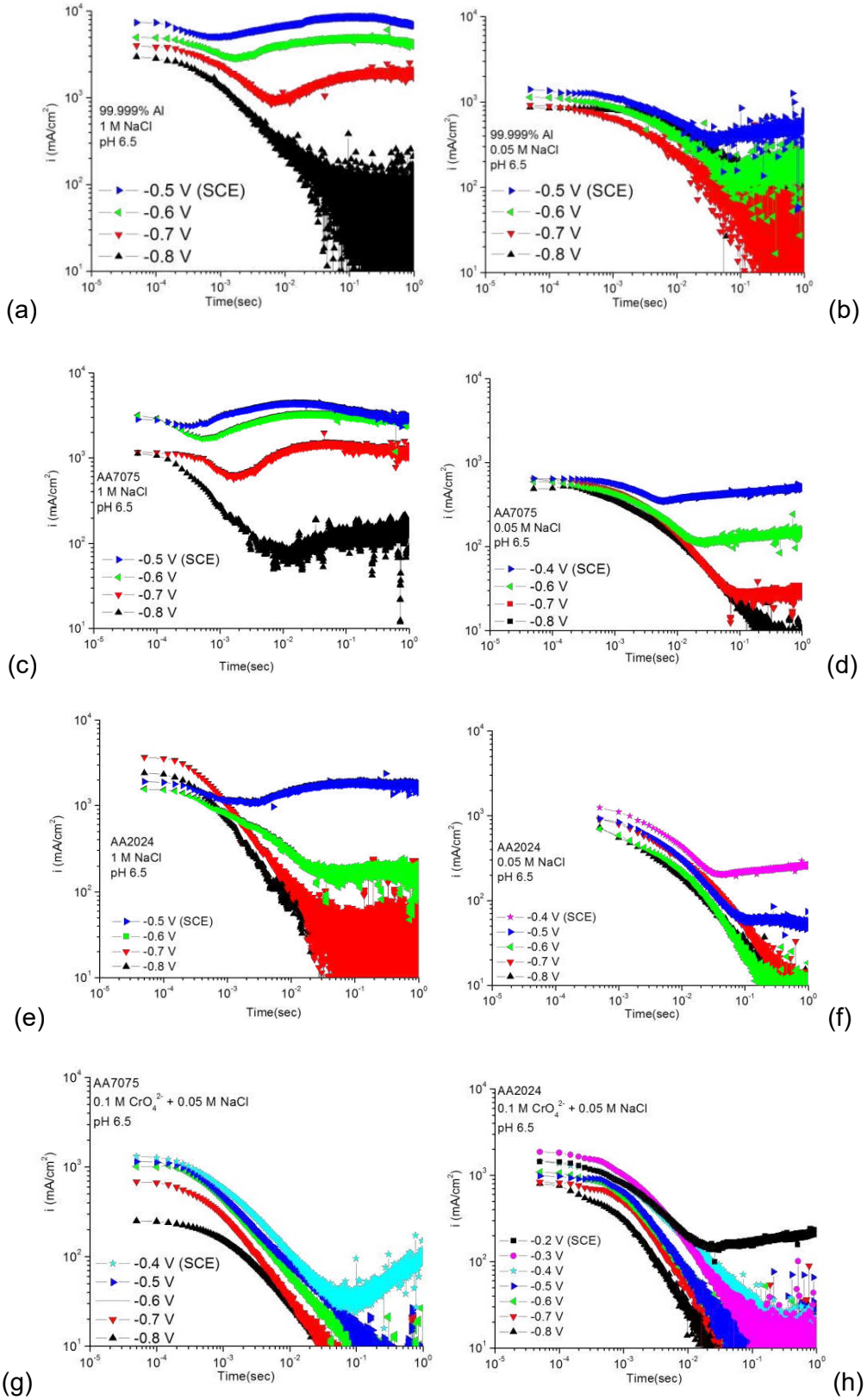

Figure 2.28: Decay of current density vs time for Al99.999, AA7075 and AA2024 in NaCl solutions at different potentials and for AA7075 with the addition of chromate ions [69]

Alloy AA7075 shows slightly worse repassivation behaviour than pure aluminium (Figures 2.28 (c) and (d)). This is easily understandable when considering the precipitations that are present in this high strength alloy when compared Al99.999.

The alloy AA2024 shows slightly better repassivation behaviour than pure aluminium (Figures 2.28 (e) and (f)). The authors conclude that this is due to the higher amount of dissolved copper in the aluminium matrix which yields to a more positive pitting potential [69-71]. As a result the repassivation potential of the alloy is increased.

By adding chromate to the electrolyte (Figure 2.28 (g) and (h)) repassivation behaviour of alloys 7075 and 2024 improves significantly. Chromate ions serve as an inhibitor of the anodic dissolution reaction in the scratch and thus reduce the charge used for repassivation. The authors have also investigated the addition of molybdate to the electrolyte, in contradiction to chromate the molybdate did not improve repassivation properties of the alloys (not shown in this work). [69]

2.3.3 Repassivation data on titanium alloys

In 1974 Beck [72] has investigated repassivation of titanium in chloride solutions to get a better understanding of stress corrosion cracking (SCC) of titanium. He already applied Stern's approach and showed data on repassivation kinetics in log i(t) vs log t plots. Figure 2.29 shows the repassivation of titanium in 3 M HCl and in 0.6 M KCl. The setup was a fast rupture method generating fresh surface and acquisition of data at a rate of 10^4 s^{-1}. In Figure 2.29 (a) a theoretical curve of repassivation has been included as well (in contradiction to many more recent works) that has been derived from the growth kinetics of TiO_2 by the high field mechanism by the same author [73].

The author found very similar repassivation rates in chloride and sulfate solutions [72].

After 1 s titanium reaches a corrosion current density of 10^{-3} A/cm^2. Steady state of passivity of titanium is reported to be close to 1 µA/cm^2. The extremely high repassivation rate of titanium together with very high active corrosion current density led the author to the expression of the "electrochemical knife" by which titanium is damaged during SCC processes. Another expression with the same meaning is the epithet "binary metal" for titanium. It is either highly passive or it corrodes at very high rates [74].

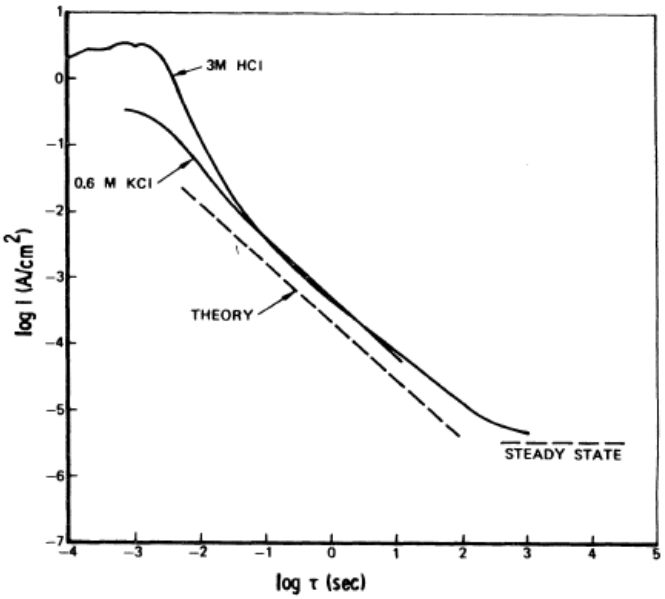

Figure 2.29: Current density vs time for titanium in 0.6 M KCl and 3 M HCl at 0 V_{SCE} measured by fast fracture experiments [72]

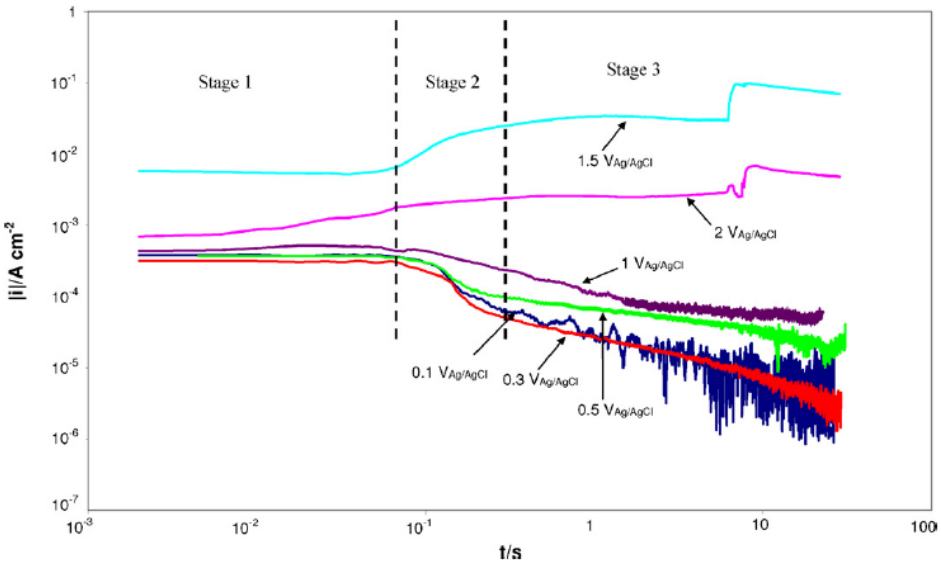

Figure 2.30: Current density vs time for titanium in 992 g/L LiBr solution at different potentials; depassivation was introduced by cavitation [75]

Fernandez-Domene et al. have found a similar behavior of titanium with high rates of repassivation or – at too high potentials – no repassivation at all and dissolution at high rates, when passive layer formation is no longer possible (Figure 2.30 [75]). The current densities appear low immediately after activation in this work.

Repassivation rates with different methods have been measured for titanium by Kolman and Scully [76,77]. Their data (Figure 2.31) fit very well to those found earlier by Beck under similar conditions [72]. Limitations of potentiostatic repassivation experiments are that potentiostatic conditions are not always maintained and that the peak current is not accurately measured since some repassivation has already taken place during the scratch creation itself.

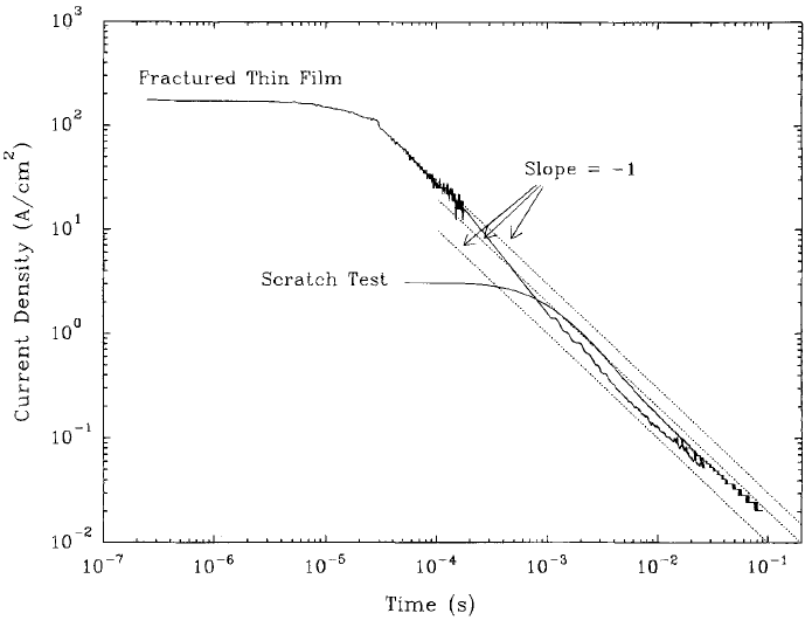

Figure 2.31: Comparison of current transients on titanium obtained from scratch testing and thin-film fracture testing in 0.6 M NaCl at 0 V_{SCE} [76]

2.3.4 Repassivation data on other passive alloys

Kim et al. [78] have investigated the behavior of scratched zirconium alloys in boric acid containing lithium hydroxide. Their evaluation was, however, aimed at the cBV value and they do not show any log i(t) vs log t plots. A 90 % extent of repassivation is reached at times equal to 0.01 s after scratching.

Guan et al. [79] have investigated niobium in fluoride containing solutions with different pH. They did not show any log i(t) vs log t plots as well. The same is valid for Gad-Allah and co-authors [80], who investigated molybdenum in several salt solutions (NaCl, $NaNO_3$, Na_2SO_4, Na_3PO_4). Especially data on molybdenum would have been interesting, since it is not a truly passive metal and forms oxide films with a high defect density.

2.4 Methods of investigating repassivation kinetics

Several types of experiments were developed in the pursuit of understanding repassivation and its kinetics. These experimental methods remove the pre-existing oxide film (most often mechanically) and focus on the current response of a sample, usually under potentiostatic polarization. The potential at which a metal is polarized will have a large effect on repassivation – both in regards to the peak current height as well as the resulting thickness of the passive layer formed on the exposed metal. For stainless steel, it can be expected that a potential above 800 mV_{SHE} (at pH 7) will result in iron oxi-hydroxides formed while chromium oxides are being dissolved. Due to this reason the corrosion potential of the steel is usually determined beforehand and polarization is set in relation to that, ranging anywhere between +25 mV vs. the measured corrosion potential to 800 mV_{SHE}.

Generally speaking, the closer the applied potential is to the measured corrosion potential, the closer the resulting passive film will mimic the native passive film. This, however, comes at the expense of precision. The corrosion potential of samples made from the same steel may vary in several 10 mV, meaning it may be difficult to determine the difference between the applied potential and corrosion potential if a small applied potential is used. This type of testing has resulted in a better understanding of the potential drop occurring in the oxide films formed on different types of material – for example the AISI 316L steel formed in borate buffer solution was found to have an electric field strength of $3.97 \cdot 10^6$ V/cm^2 [81].

2.4.1 Scratch test

The scratch test is the simplest method used for investigation of repassivation kinetics. It involves a sample passivated with the help of a potentiostat and a counter electrode, which is then scratched with the help of a non-reactive tip, creating a fresh metal surface that comes into contact with the electrolyte [82,83]. The current response is measured and several parameters may be calculated, such as the amount of charge consumed, the electric field strength of the formed oxide layer and certain parameters describing repassivation rates. The background has been described in equations 12 to 15.

In these equations, however, one cannot explain the peak current height, as it makes no sense at time t = 0.

The equations 12 to 15 have allowed researchers to propose several theories, again each with their strengths and weaknesses. While some believe that initial nucleation and formation of a monolayer of film follows the exchange model, followed by the high field ion conduction model describing the passive film growth in thickness, others claim that the relationship between current density and time at the start of repassivation events are skewed because anodic dissolution of the bare metal was not taken into account, claiming to be able to separate the anodic dissolution current from the oxide formation current and conforming fully to the ion conduction model.

Figure 2.32 shows the setup for a scratch test [61]. With a diamond tip, often a Vickers hardness indenter, a fast scratch is made on the sample resulting in depassivation at the scratch and maintained passivity outside the scratched area. An advantage of the scratch test is that it can be built up without extreme efforts. On the other side some disadvantages have to be considered such as only local activation of the specimen including the possibility of galvanic effects between scratched and not scratched areas, introduction of cold deformation, a certain lack of reproducibility of scratch size and the danger of the diamond tip jumping over the specimen resulting in undefined scratched areas.

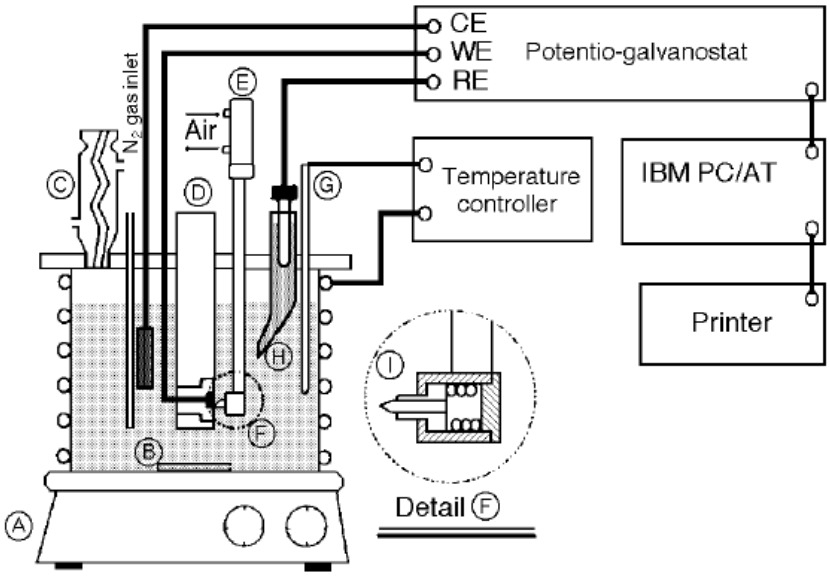

Figure 2.32: Schematic of scratching electrode cell, with A…magnetic plate, B…stirrer, C…condenser, D…specimen holder, E…electric valve, F…scratcher, G…thermometer, H…Luggin capillary, I…diamond tip [61]

The other option for scratch testing involves not polarizing the working electrode, instead utilizing a zero resistance ammeter in conjunction to a high resistivity voltmeter, measuring the current flowing between two identical electrodes (one of which is scratched) and the potential

of the entire system by connecting the voltmeter to the scratched electrode and a reference electrode of choice. During scratching the charge stored in the electrochemical double layer (EDL) is released and current flows from the anodic scratched area to the cathodic untouched surface of both electrodes. If we assume the scratch is small in comparison to the entire electrode surface this in effect means approximately half of the current flowing from the scratch will flow into the unscratched electrode with some losses due to the solution electrical resistance and distance between the electrodes.

2.4.2 Guillotine test

The guillotine test [66,84-88] is similar to the scratch test, where a fresh metal surface is introduced to the solution by means of mechanical removal of the passive layer. Unlike the scratch test there is no leftover passive surface on the working electrode but instead an entirely new cross section of the sample is created by cutting off (or guillotining) the sample (Figure 2.33).

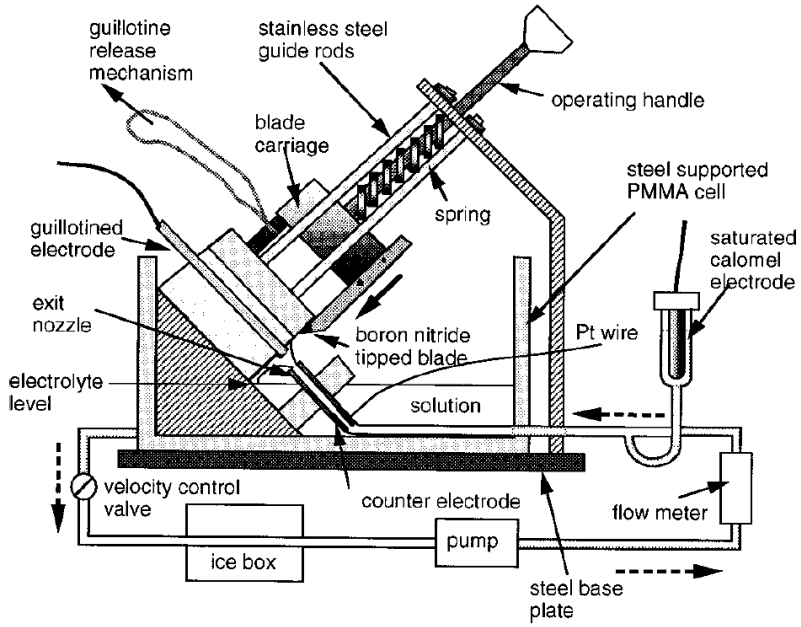

Figure 2.33: Schematic of the fluid impacting guillotined electrode and cell, by a spring the guillotine scratches the wire specimen that is connected with a reference and a counter electrode [66]

The main benefit of using the guillotine test over the scratch test is having a well-defined surface area that is repassivating with no additional (galvanic) effect from the rest of the still

passive surface, allowing more precise measurements of certain parameters such as the current density flowing from the oxidizing metal, allowing further precise calculations of other parameters such as charge density and constants used in defining repassivation kinetics as described in equations 12 to 15. Another advantage of this method is that due to having a small enough surface area exposed, there is little chance of a sample not being homogenous in microstructure or chemical composition. Unfortunately, this method also has several drawbacks, such as requiring a relatively soft metal in order to not damage the equipment used or even causing unwanted effects such as crevice corrosion due to the metal being deformed in the protective sleeve. Individual samples made from the same alloy may have widely different chemical compositions in case of the alloy used to create the samples having non-homogenous properties due to for example segregations and creating such samples from larger pieces of metal is a process that might cause dislocations, affecting the overall behavior of such samples. Thus, samples should be produced in the form of thin wires in a highly controlled environment, meaning the method is best suited for basic study of pure metals and not as well suited for robust studies in applicative scenarios.

2.4.3 Micro-indentation test

Another idea used for the study of repassivation kinetics involves indenting the surface of a sample by means of a hardness indenter (for e.g. a Vickers hardness indenter) [89-94]. A schematic diagram of such an experimental setup is shown in Figure 2.34 [90]. This type of test is interesting, as it allows for a controlled indenting force applied, extremely precise measurement of the indented surface area and additionally allows hardness measurements of the investigated samples. Unfortunately, unlike the scratch and guillotine tests, this method does not completely remove the oxide layer and instead pushes it into the underlying metal, meaning that the indented surface is partially covered in a cracked oxide layer, the underlying metal does not necessarily have the same chemical composition as the bulk metal (depending on alloying elements) and thus might affect results depending on several factors that are not quantifiable. To address this, researchers have used this method in such a way, that the same spot is indented several times in a row with an ever increasing force while measuring the effect of indentation depth on the responses from the sample. While such a method may yield interesting results it is not meant for use with metals, where the chemical compositions of the bulk metal and the metal just beneath the passive layer (interface) might vary, such as stainless steel and was thus found unfit for the use in this study.

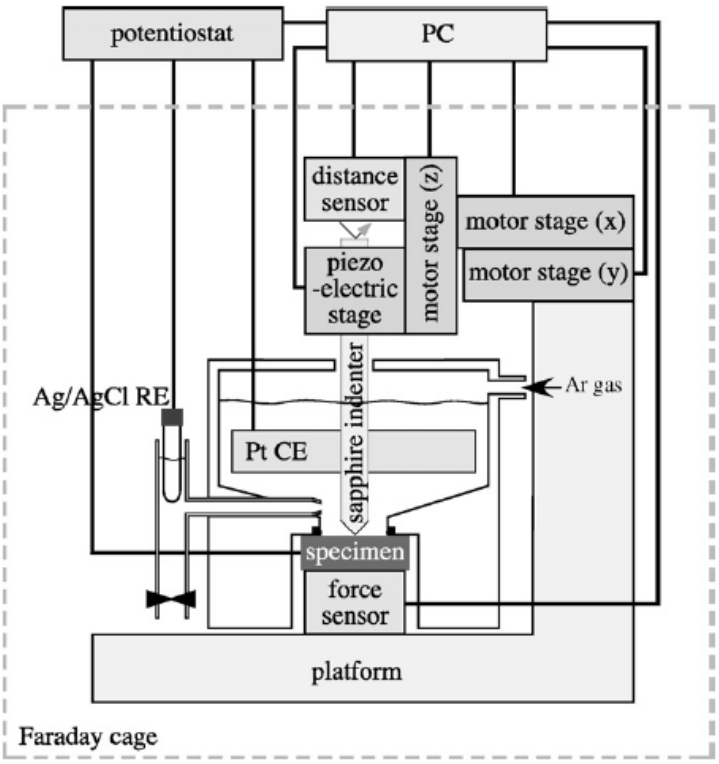

Figure 2.34: Schematic of micro-indentation test [90]

2.4.4 Abrading electrode technique

Lee [64] used an electrode that was grinded during activation with a rotating cylinder of abrasive paper (Figure 2.35). The advantage of this method is that a fast and sudden generation of a completely bare metal surface can be obtained. In contradiction to the guillotine test the surface remains less mechanically damaged by cold working and introduction of heavy plastic deformation. This is maintained by using a fine grained abrasive SiC paper (#1200). During abrading the holder with the SiC paper is raised suddenly by a spring.

2.4.5 Fast straining experiment

Galvele and his group [65,95] describe a mechanical device that via release of a spring produces 10 % elongation of a wire. Elongation was completed within 10^{-2} s. The corresponding strain rate was 10 s^{-1}. In contradiction to that a slow strain rate test works on a strain rate of 10^{-5} to 10^{-6} s^{-1} [96] and a conventional tensile test shall be performed between

10^{-4} and 10^{-3} s^{-1} [97]. With the help of this fast elongation a fresh metal surface is produced, allowing repassivation testing. The setup is shown in Figure 2.36.

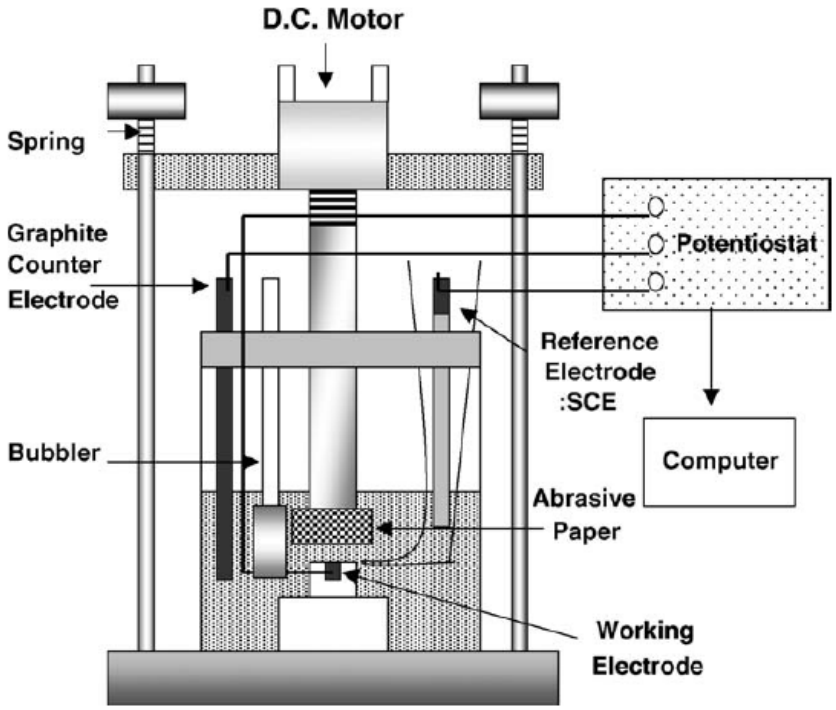

Figure 2.35: Apparatus for the abrading electrode technique [64]

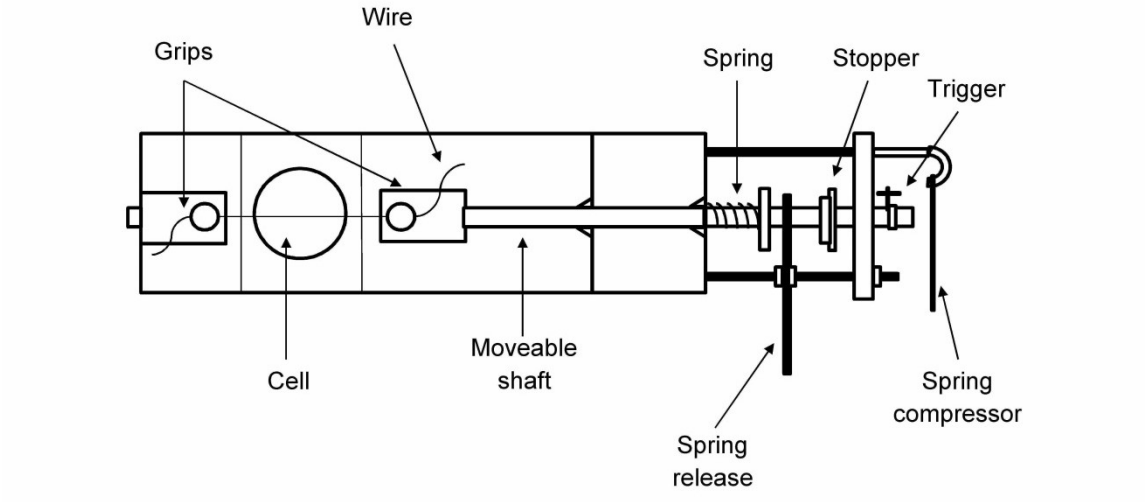

Figure 2.36: Schematic view of a fast straining experiment [65]

2.4.6 Breaking-electrode cell

Frankel and co-workers have used the breaking-electrode cell [67]. It is shown schematically in Figure 2.37. The authors thermally oxidized a silicon strip to form a thick insulating oxide layer on its surface. Then they masked its surface with Si_3N_4 and sputtered the passive metal – in their case aluminum – into the profile. Finally the aluminum was covered with another deposited Si_3N_4 top layer (Figure 2.37 (a)). The sample was inserted through a slot in a Plexiglas cell and clamped. The sample extended into the cell 4 mm over the clamp. A scribe mark was introduced to enable crack initiation and finally the cantilever part of the specimen was tapped by a Plexiglas plunger (Figure 2.37 (b)). All other parts including application of a constant potential and a measurement device were comparable with other methods.

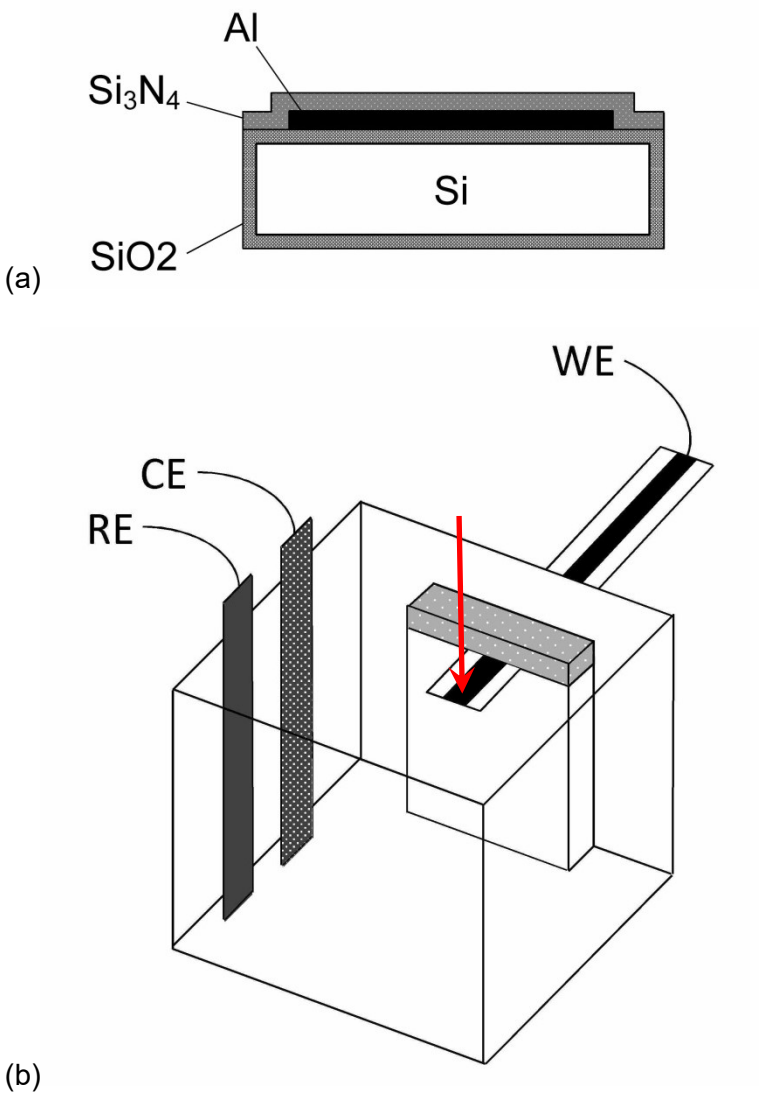

Figure 2.37: Schematic diagrams of (a) sample cross section and (b) breaking-electrode cell [67]

3 Experimental

3.1 Materials

Several different types of stainless steel were investigated, with different alloying content and microstructure. Since the surface preparation affects corrosion properties, these conditions are explained for each type of experiment separately. The steels themselves ranged from martensitic to bainitic, austenitic and duplex (austenitic-ferritic combination) in microstructure. Seven steel grades have been investigated. Table 3.1 shows chemical compositions and PREN values.

Table 3.1: Chemical composition and PREN values of investigated stainless steel grades

Steel	C [%]	Mn [%]	S [%]	Cr [%]	Ni [%]	Mo [%]	N [%]	PREN
13Cr	0.190	0.52	0.0037	12.41	0.18	0.01	0.022	12.7
13Cr6Ni2Mo	0.013	0.36	0.0022	12.55	5.85	2.2	0.007	19.9
15Cr6Ni2Mo	0.028	0.28	0.0023	14.67	6.04	1.92	0.028	21.4
17Cr4Ni2Mo	0.033	0.33	0.0031	16.84	3.74	2.4	0.035	25.3
17Cr12Ni2Mo	0.01	1.87	0.0007	17.24	11.62	2.34	0.063	26.0
22Cr5Ni3Mo	0.027	1.79	0.0028	22.08	5.42	3.29	0.101	34.5
20Cr24Ni6Mo	0.010	0.83	0.0005	20.36	24.49	6.35	0.076	42.5

PREN = %Cr + 3.3·%Mo + 16·%N

Throughout this work the investigated materials are used with the following self-explaining nomenclature:

XCrYNiZMo … meaning stainless steels with

X wt% Cr, Y wt% Ni and Z wt% Mo (16).

For sub-surface applications in oil and gas production (tubing and piping used inside wells) mainly the martensitic grades (including both martensitic and bainitic steels) are considered primarily due to their lower alloying content (and price) as well as due to their ability to strengthen by heat treatment, while the austenitic steels do not allow this. The austenitic steels may only have their mechanical properties enhanced or changed by cold working.

The main outlier of the group is 13Cr (Figure 3.1) which contains no nickel or molybdenum, and which contains a higher amount of carbon allowing a martensitic microstructure. It has by far the lowest PREN value (12.7). The next two steels 13Cr6Ni2Mo (Figure 3.2) and 15Cr6Ni2Mo (Figure 3.3) are very similar in all regards – both have a bainitic microstructure and similar PREN values (19.9 and 21.4), meaning they are expected to have similar corrosion resistances. 17Cr4Ni2Mo (Figure 3.4) and 17Cr12Ni2Mo (Figure 3.5) steels have very similar amounts of chromium, molybdenum and consequently PREN values (25.3 and 26.0) with only a large difference in nickel content, which affects microstructure – the 17Cr4Ni2Mo is both ferritic and bainitic, while 17Cr12Ni2Mo is purely austenitic. The comparison of these two steels might thus be able to show how microstructure affects corrosion properties. The 22Cr5Ni3Mo (Figure 3.6) is the only duplex steel. It has a high PREN value of 34.5. In the image shown below the ferritic phase (α) has a grey blue color, the austenitic phase (γ) is bright. The matrix is the ferrite and representing between 55 and 60 % (estimated from Figure 3.6) of the whole microstructure.

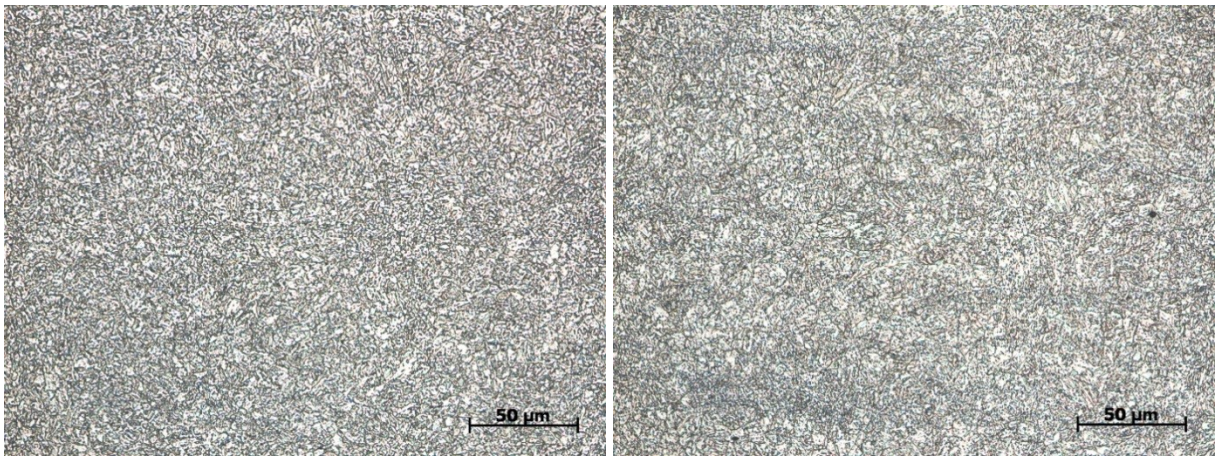

Figure 3.1: Martensitic microstructure of 13Cr steel viewed on the longitudinal plane (left) and transversal plane (right), fine grain size between 10 and 30 µm

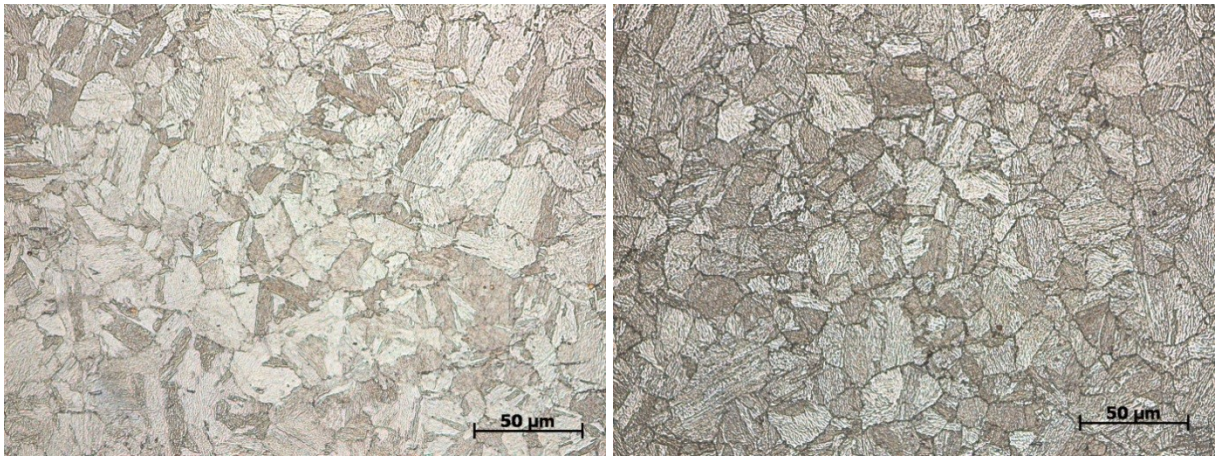

Figure 3.2: Bainitic microstructure of 13Cr6Ni2Mo steel viewed on the longitudinal plane (left) and transversal plane (right), fine grain size between 20 and 40 µm

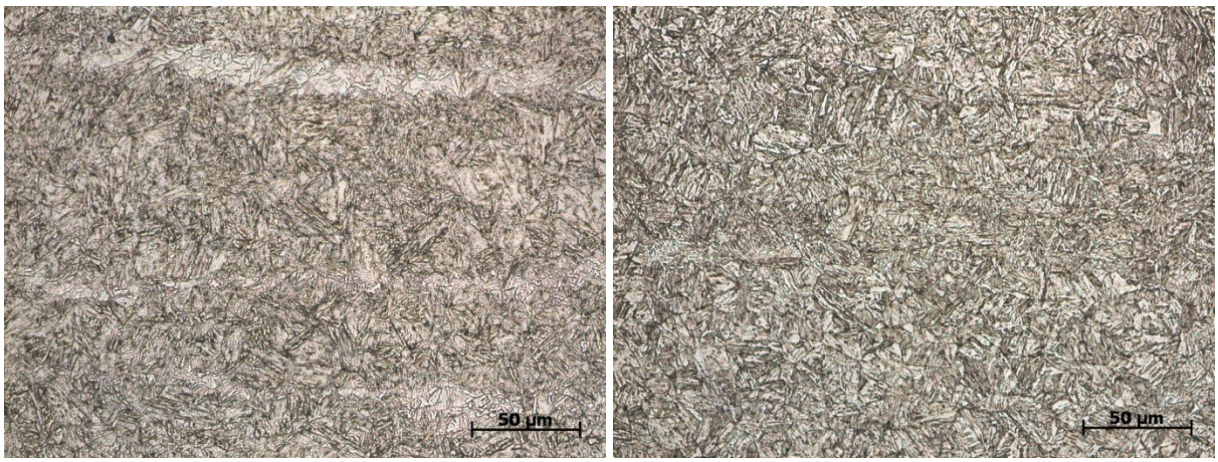

Figure 3.3: Bainitic microstructure of 15Cr6Ni2Mo steel viewed on the longitudinal plane (left) and transversal plane (right), fine grain size between 20 and 40 µm

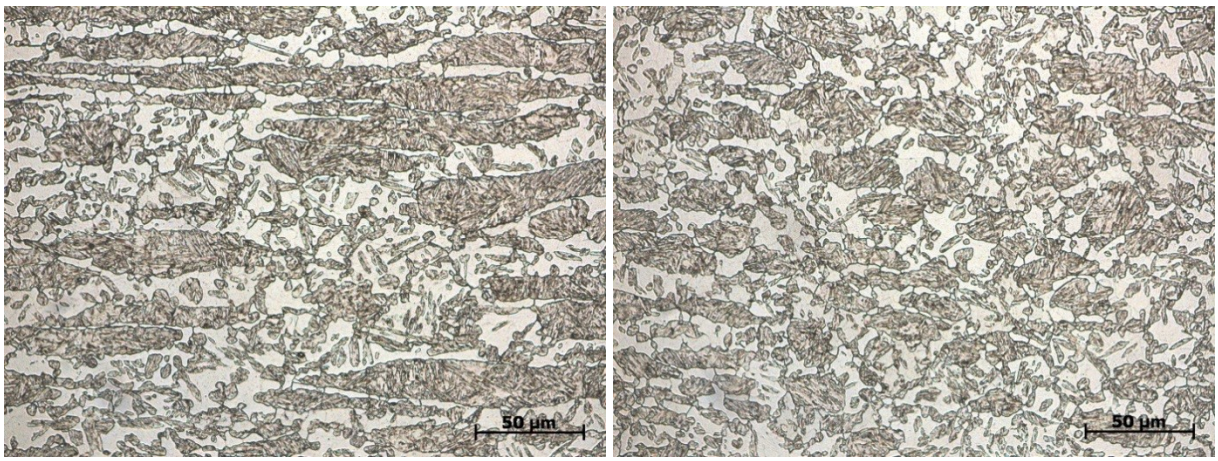

Figure 3.4: Bainitic-ferritic microstructure of 17Cr4Ni2Mo steel viewed on the longitudinal plane (left) and transversal plane (right), fine grain size between 20 and 50 µm

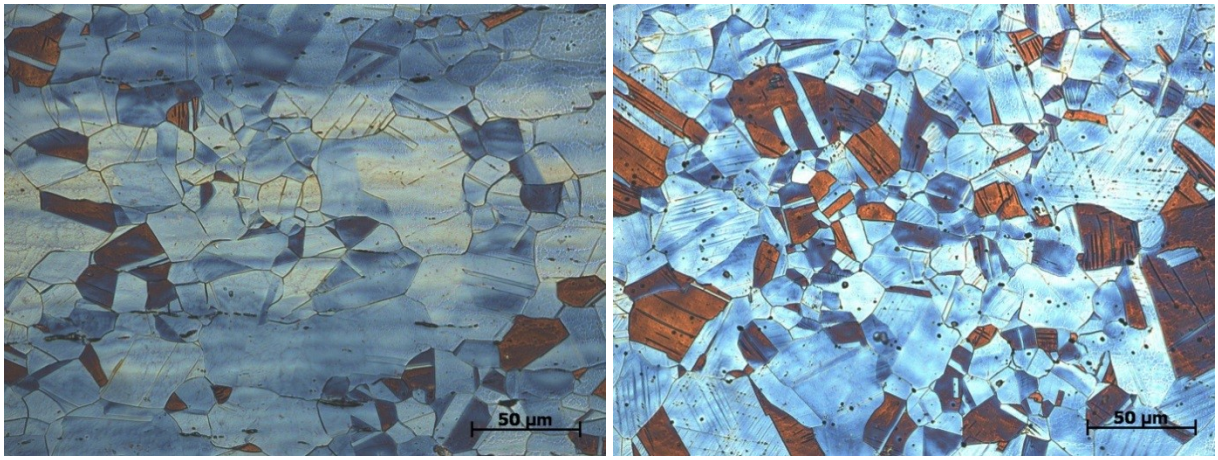

Figure 3.5: Austenitic microstructure of 17Cr12Ni2Mo steel viewed on the longitudinal plane (left) and transversal plane (right), fine grain size between 20 and 50 µm

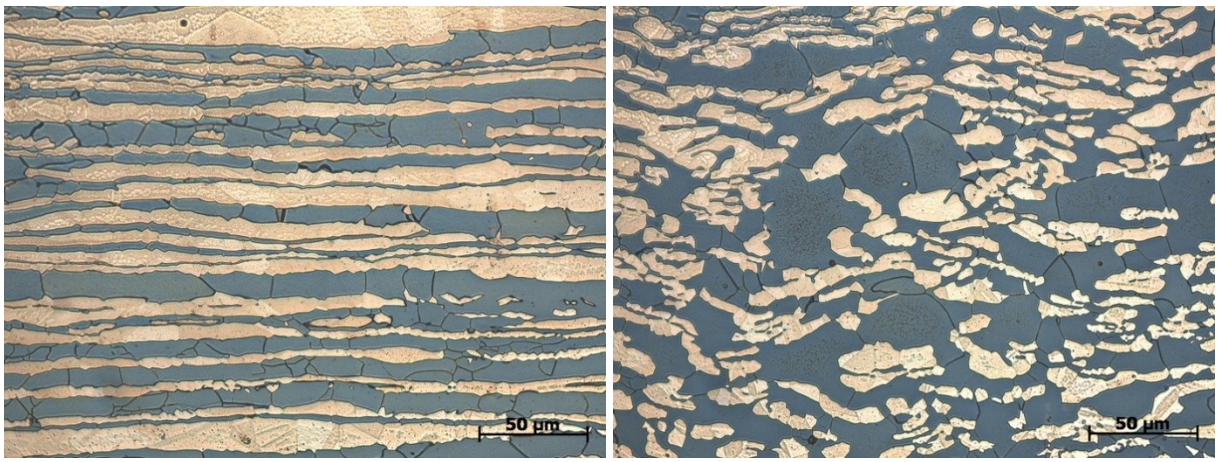

Figure 3.6: Duplex (austenite-ferrite) microstructure of 22Cr5Ni3Mo steel viewed on the longitudinal plane (left) and transversal plane (right), fine elongated grain size between 10 and 50 µm

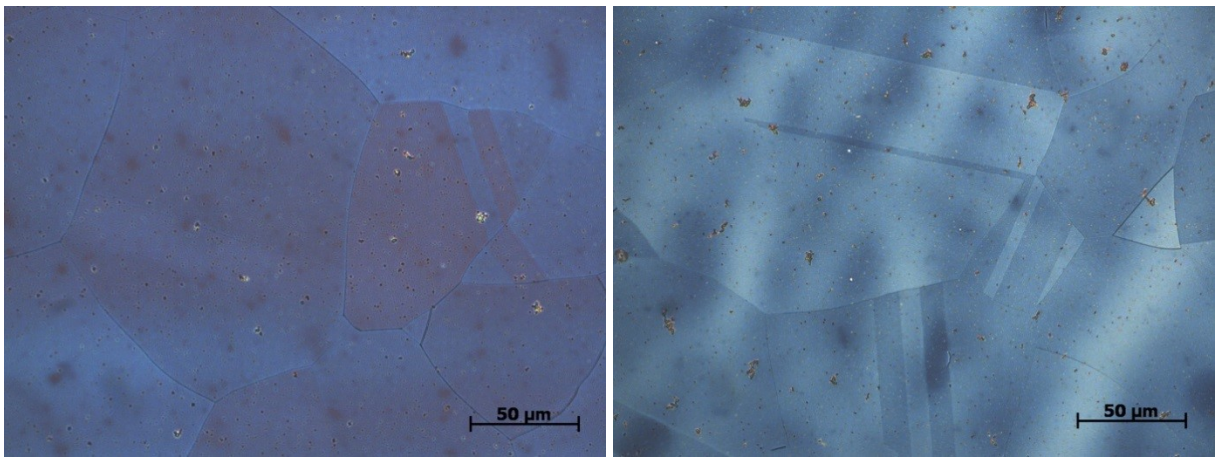

Figure 3.7: Austenitic microstructure of 20Cr25Ni6Mo steel viewed on the longitudinal plane (left) and transversal plane (right), usual coarse austenitic grain size between 100 and 400 µm

The 20Cr24Ni6Mo (Figure 3.7) is a superaustenitic stainless steel grade meaning it is austenitic in microstructure with very good corrosion resistance properties as a result of the high alloying content (superaustenites have a PREN > 40).

All steels show a fine grain size below 50 µm except the superaustenite, which has a grain size of a few 100 µm. This is for many austenitic stainless steels a usual grain size. The duplex stainless steel 22Cr5Ni3Mo shows elongated grains of α- and γ-phase.

Tensile specimens were made from the steels and were tested to determine the mechanical properties, namely tensile strength (R_m), yield strength ($R_{p0.2}$), fracture elongation (A_{25mm}) as well as reduction of area (Z) (Table 3.2). The two austenitic stainless steels showed a much higher fracture elongation than the martensitic and bainitic ones. All steels have a tensile strength between 700 and 1070 MPa, a yield strength between 510 and 1020 MPa and a reduction of area between 63 and 82 %.

Table 3.2: Mechanical properties of investigated stainless steel grades examined with tensile tests

Steel	Sample #	R_m [MPa]	$R_{p0.2}$ [MPa]	A_{25mm} [%]	Z [%]
13Cr	1	777.8	624.5	21.7	70.0
	2	781.0	627.3	22.4	70.5
13Cr6Ni2Mo	1	840.2	716.6	24.0	79.2
	2	838.7	713.3	23.8	79.3
15Cr6Ni2Mo	1	1065.0	1012.0	22.0	71.1
	2	1063.0	1009.0	21.2	70.2
17Cr4Ni2Mo	1	960.7	799.2	22.3	63.5
	2	959.8	797.0	23.2	67.5
17Cr12Ni2Mo	1	710.0	528.5	47.5	77.8
	2	708.9	513.7	47.2	77.7
22Cr5Ni3Mo	1	940.0	787.2	20.5	68.0
	2	941.4	793.7	19.2	68.5
20Cr24Ni6Mo	1	737.9	342.9	56.8	81.7
	2	738.3	345.3	56.9	81.8

3.2 Corrosion testing

In order to perform corrosion testing a medium is required, in which tests are performed. It was decided to perform all corrosion tests in NaCl brines with two salt concentrations (5 % NaCl and 0.00833% NaCl by weight) and two temperatures (30 °C and 80 °C). All experiments were performed in thoroughly deaerated brines, where dissolved oxygen content was maintained below 100 ppb.

3.2.1 Immersion tests

Immersion tests were performed on rectangular samples (size: 10 mm x 10 mm x 3 mm) with rounded edges in beakers containing 50 mL of solution, ensuring a solution to surface area ratio of at least 15 ml/cm^2. Each beaker was placed into a heating bath, ensuring the proper temperature of the solution in the beaker. All beakers (up to 8) were purged from one argon tank and the gas was forced into each beaker through tubes containing identical PTFE plugs with small holes, ensuring the same distribution of gas through each tube as well as creating a barrier, preventing most vapor from leaving the beakers at elevated temperatures. The experimental setup is shown in Figure 3.8.

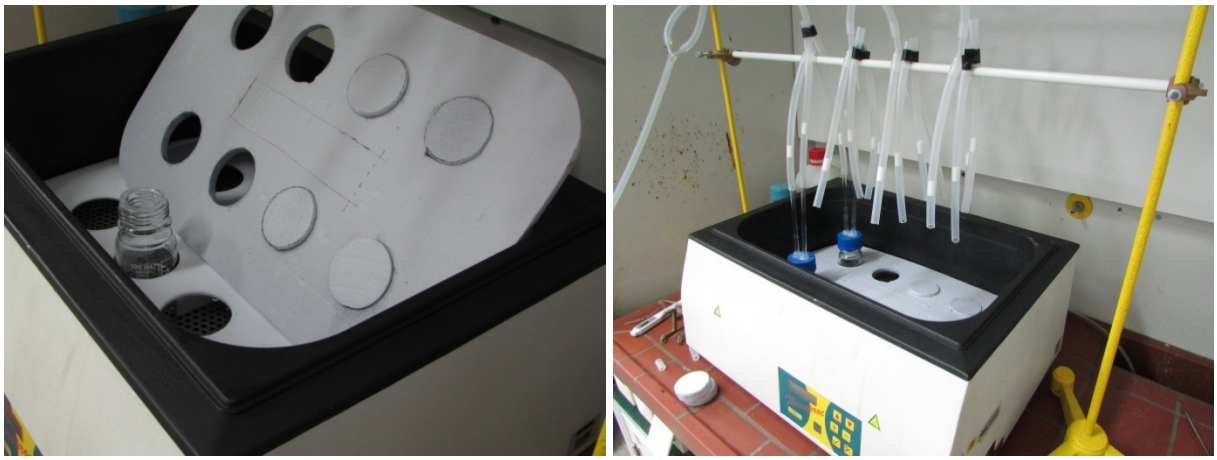

(a) (b)

Figure 3.8: Heating bath with PTFE holding plate placed inside bath and insulating polystyrene plate (a) and immersion test experimental setup with two beakers inside (b)

The samples were prepared by wet grinding with #600 abrasive SiC paper and storage in a desiccator for at least 24 hours to allow repassivation prior to exposure. The exposure of the

samples lasted for 24 hours before the samples were removed from the solution, rinsed with distilled water and cleaned with paper towels before additionally rinsing with distilled water and finally acetone to dry the samples off. After immersion testing, the samples were investigated by means of optical microscopy to determine the type of corrosion occurring in each specific case.

The solution was purged with argon for at least 1 hour prior to sample exposure as well as during exposure, to reduce the amount of dissolved oxygen to values in the range of 40 ppb (measured before and after immersion test). The pH of the solution was set to desired values (0, 1, 2,… ,6) by addition of HCl and was measured before and after each test. The HCl addition affected the chloride concentration of the solution as can be seen in Table 3.3.

Table 3.3: Chloride ion concentration in different NaCl solutions at pH values between 0 and 6, where the pH was adjusted by means of HCl addition

NaCl conc. [wt.%]	pH 0 [mg/l Cl^-]	pH 1 [mg/l Cl^-]	pH 2 [mg/l Cl^-]	pH 3 [mg/l Cl^-]	pH 4 [mg/l Cl^-]	pH 5 [mg/l Cl^-]	pH 6 [mg/l Cl^-]
5	62795	33578	30656	30364	30335	30332	30331
0.00833	35498	3595	405	86	54	51	51

3.2.2 Potentiodynamic tests

Potentiodynamic tests were performed on rectangular samples (size: 40 mm x 10 mm x 3 mm) with rounded edges in a corrosion cell (Figure 3.9). The samples were fully immersed in the solution along with the contact area (Pt contact). These experiments were performed in four solutions:

- 0.00833 % NaCl (wt.) at 30 °C,
- 0.00833 % NaCl (wt.) at 80 °C,
- 5 % NaCl (wt.) at 30 °C, and
- 5 % NaCl (wt.) at 80 °C.

As was the case with immersion tests, the samples for potentiodynamic tests were grinded with #600 abrasive SiC paper and stored for at least 24 hours in a desiccator to allow repassivation. The experiments were performed by the use of a Gamry Reference 600 potentiostat. An annealed Pt sheet was used as a counter electrode, while for the reference

electrode a saturated calomel electrode (SCE) at a potential of 241 mV_{SHE} was used (SHE … standard hydrogen electrode).

(a) (b)

Figure 3.9: Experimental setup (a) and corrosion cell (b) used to perform potentiodynamic tests

The open circuit potential (OCP) was measured for at least 1 hour prior to starting the potentiodynamic test, and a longer time was used in case OCP has not stabilized during this time. For the potentiodynamic measurement, the starting potential was set to 100 mV below OCP, the scan rate was set to 200 mV/h and the scan was reversed once a current density of 1 mA/cm^2 was reached or a potential of 2 V_{SCE} was reached. The test was ended once the cathodic polarization regime was reached again or once the potential reached -2 V (when experiments were left over night).

The solution was purged with CO_2 for at least one hour prior to starting the measurement and stopped after the measurement, which caused the pH to decrease to values between 4.3 and 3.8 during the measurement. The dissolved oxygen levels were measured. They were in the range of 70 ppb.

3.2.3 Scratch tests

Scratch tests were performed at open circuit potential in argon purged 5 % NaCl solutions with HCl addition to set pH to desired values (usually pH 3). The tests involved using two identical cylindrical electrodes (∅ = 5 mm, L = ~ 15 mm), where only one flat surface was exposed to the solution. The electrodes were prepared with wet grinding using #2500 abrasive SiC paper. During grinding, the edge was chamfered (~ 0.5 mm x 45 °) to allow easier movement of the

diamond stylus across the surface by reducing the chance of the diamond tip leaving the surface upon contact and creating an interrupted scratch by jumping over the surface. Immediately after grinding the electrodes were introduced into the prepared solution, connected with an insulated nickel wire and left for a period of 20 hours to obtain a steady state, before performing the scratch. During the scratch, the two working electrodes WE1 and WE2 were connected with a zero resistance ammeter (ZRA) to measure the current flowing between them while working electrode 1 (WE1 – the scratched electrode) was also connected to a reference electrode through a high impedance voltmeter (HRU). The reference electrode used was either a SCE for experiments performed at 30 °C or a Ag/AgCl electrode for experiments performed at 80 °C. Data acquisition rate was set to 500 Hz with a current range of up to 1 mA and potential range of up to 1 V.

Since the current is only measured between the two identical working electrodes, the current flowing from the scratched area of WE1 into the passive area of WE1 is not measured, meaning that the entire current created by the scratched area is not measured but only a certain portion. The scratch area projection was measured with an optical microscope, allowing the calculation of the actual scratch area according to the diamond tip shape. The measured current transient was deducted from the average current in the last 5 seconds before creating the scratch and this current difference was divided with the scratch area to obtain the current density flowing from the scratch to WE2. A schematic and an image of the experimental setup are shown in Figure 3.10.

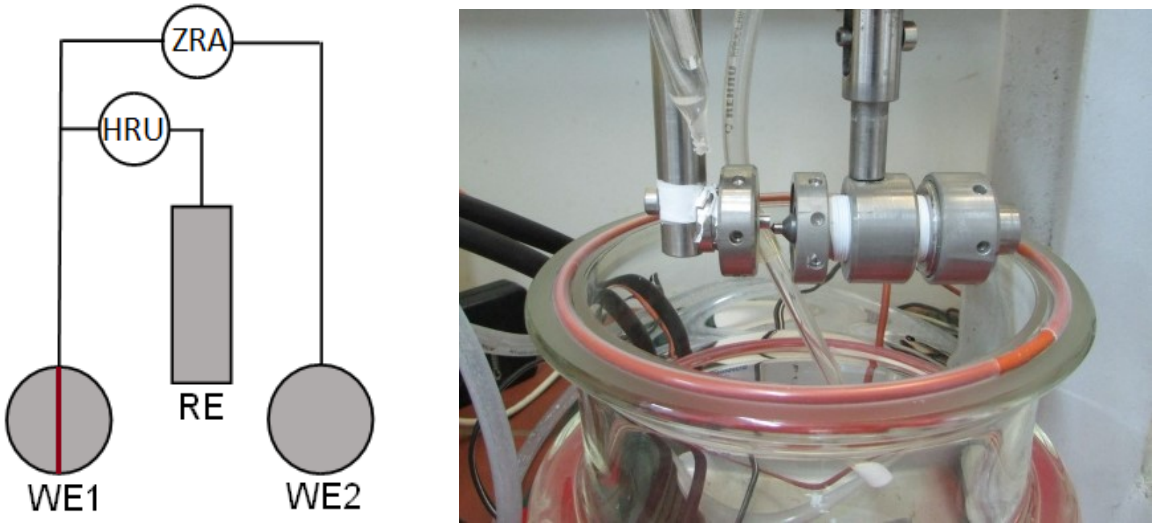

(a) (b)

Figure 3.10: Schematic of scratch test (a) and scratch test experimental setup (b)
ZRA … Zero resistance ammeter
HRU… High resistivity voltmeter

3.2.4 Chemical depassivation tests

The chemical depassivation test is a new experimental method (Figure 3.11), developed specifically to investigate the difference between activation and repassivation pH values. The idea behind this setup is to slowly decrease the pH of the solution in contact with investigated samples until the passive layer fails due to the increased solution aggressiveness, followed by an increase of pH until repassivation occurs. Once the passive layer fails a large amount of corrosion can be expected to occur, which will also change the composition of the solution. Therefore it was decided to perform these experiments in a flow cell. Three large solution containers (1 300 L container and 2 130 L containers) were used, which were filled with 5 % NaCl at different pH values, where the pH ranged between 5 and 1, depending on the investigated steels. All three solution containers were thoroughly deaerated by means of argon purging for a period of 24 hours before starting the experiment, ensuring a level of dissolved oxygen well below 100 ppb. While the exact amount of dissolved oxygen would vary between the solution containers and across different experiments, it was usually in the range between 20 and 70 ppb.

The solution was pumped from these containers using precise membrane pumps in different ratios into a mixing chamber, obtaining the desired pH value of the solution flowing into the cell. Viton tubing was used, which was immersed into a thermostated heating bath to obtain the desired temperature of the solution before it would enter the insulated flow cell. The flow cell itself was additionally purged with argon to ensure the amount of dissolved oxygen would not increase.

The pH of the solution was measured inside the flow cell before the solution reached the sample block and the solution would leave the cell after flowing past the sample block, flowing into a waste solution container. The flow was set to a rate of 2 L/h and the cross section of the area where the solution flowed past the samples was approximately 15 cm^2, ensuring a slow flow velocity which should not affect corrosion rate. The volume of the flow cell was approximately 0.5 L, meaning it would take 15 minutes to completely change the solution inside the cell.

The samples used for these experiments had the same shape as the ones used for scratch tests (∅ = 5 mm, l = ~ 15 mm). Rubber tubing was placed around the samples, which were then placed into a 3 mm thick PTFE sheet with holes made to accommodate them. The samples were placed in such a way that the lowest alloyed 13Cr steel was closest to the flow cell outlet, while the highest alloyed steel 20Cr24Ni6Mo was placed closest to the electrolyte inlet of the flow cell. This shall ensure that the dissolved metallic ions from the already

corroding samples do not affect the samples that are still passive. The PTFE sheet was then placed at the bottom of large molds (60 mm x 60 mm x 60 mm) which were filled with an epoxy resin in several stages, forming sample blocks (Figure 3.12).

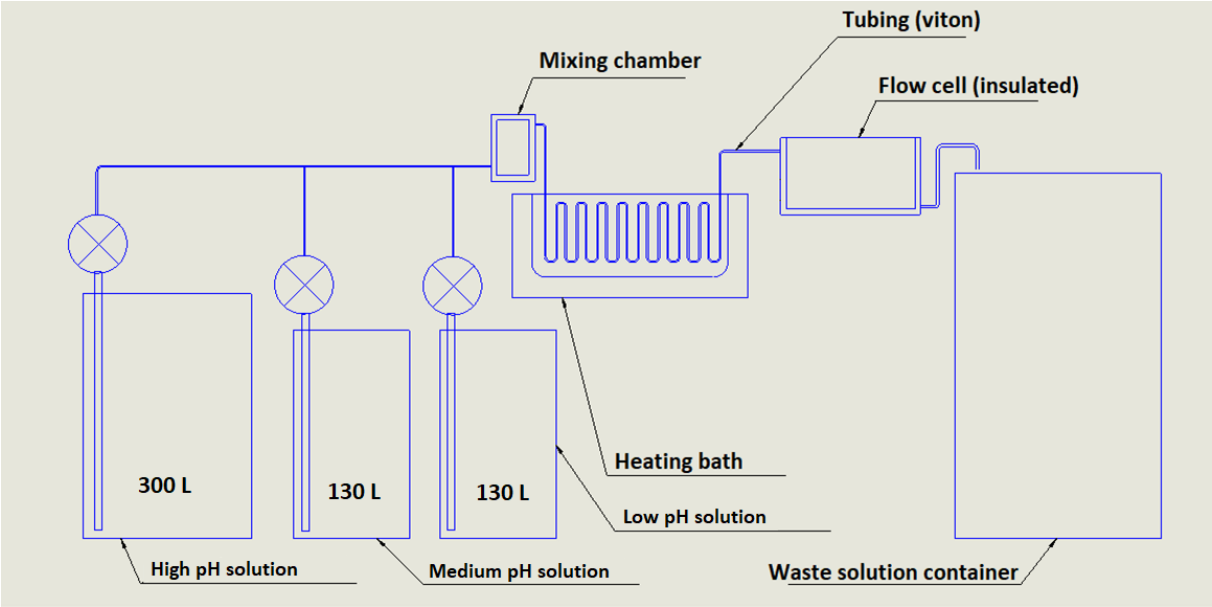

(a)

(b)

Figure 3.11: (a) Schematic of chemical depassivation test and (b) chemical depassivation test experimental setup

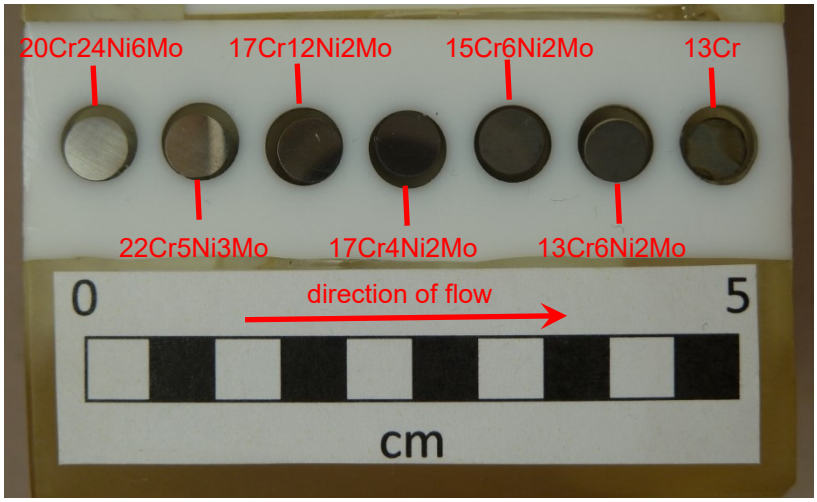

Figure 3.12: Prototype sample block with embedded seven investigated materials (contact at back side, not visible) for simultaneous evaluation in the chemical depassivation test

The samples were connected to a multiplexer (34972A LXI Data Acquisition/Switch Unit, produced by Keysight), measuring the potential of each sample and recording it every 15 seconds with the help of either a SCE reference electrode during 30 °C tests or a Ag/AgCl reference electrode during 80 °C tests. Prior to immersion, the sample blocks were wet grinded with #2500 abrasive SiC paper, ensuring a flat and smooth surface when the samples were in contact with the solution. The oxygen probe and the pH electrode were connected to a M200 transmitter, which logged concentration of dissolved oxygen in the largest solution tank as well as pH and temperature inside the flow cell every 15 seconds. Additionally, a camera was placed at the bottom of the flow cell, taking images of the exposed samples every 15 minutes.

The experiment involved reducing the pH inside the cell eight times in 0.25 pH steps, followed by increasing the pH inside the cell eight times in 0.25 pH steps, returning to the original pH value. The sample block was exposed to this solution for a total of 204 hours, with a constant pH level for 12 h each (to maintain near equilibrium conditions).

3.3 Sample evaluation and analytics

To examine the passive films formed on different steels additional immersion tests were done. Argon purged 5 % NaCl solution was used at 30 °C and the samples were introduced into the solution immediately after grinding, without storing them for 24 hours in a desiccator. After 24 hour of exposure the samples were removed from the solution, rinsed with distilled water and dried with laboratory towels.

The samples were then stored in small containers that were purged with argon to remove oxygen, which might have changed the passive layer over time. The containers were sent to IJS (Institute Jožef Stefan) in Ljubljana, where XPS and ToF-SIMS analysis were made. The prepared samples were:

- 13Cr steel passivated in air for 24 hours
- 13Cr steel passivated in 5 % NaCl, pH 5, 30 °C solution for 24 hours
- 17Cr4Ni2Mo steel passivated in air for 24 hours
- 17Cr4Ni2Mo steel passivated in 5 % NaCl, pH 5, 30 °C solution for 24 hours
- 17Cr4Ni2Mo steel passivated in 5 % NaCl, pH 3, 30 °C solution for 24 hours
- 17Cr12Ni2Mo steel passivated in air for 24 hours
- 17Cr12Ni2Mo steel passivated in 5 % NaCl, pH 5, 30 °C solution for 24 hours
- 17Cr12Ni2Mo steel passivated in 5 % NaCl, pH 1, 30 °C solution for 24 hours

3.3.1 XPS

XPS (X-ray Photoelectron Spectroscopy) was performed on a "PHI-TFA XPS" spectrometer, produced by Physical Electronics Inc, using Al- monochromatic source, Al- and Mg- standard source. This method provides information about the chemical composition on the surface, the type of oxides present and the oxide thickness.

3.3.2 ToF-SIMS

ToF-SIMS (Time of Flight Secondary Ion Mass Spectroscopy) was performed with a "TOF SIMS 5" produced by ION TOF. This method provides information about the oxide depth profile as well as the depth of the oxide layer. The samples were investigated by use of Cs^+ ion

sputtering beam of 0.5 keV energy, across an area of 400 µm x 400 µm, and a Bi^+ ion analysis beam of 30 keV energy, scanning across an area of 100 µm x 100 µm. The sputtering rate of the technique is approximately 0.020 nm/s for Cr_2O_3 oxides.

4 Results

4.1 Immersion tests

The immersion tests were performed in three solutions, differing in aggressiveness:

- 0.00833 % NaCl solution, 30 °C (low aggressiveness)
- 5 % NaCl solution, 30 °C (medium aggressiveness)
- 5 % NaCl solution, 80 °C (high aggressiveness)

After each experiment all samples were cleaned and investigated by optical microscope to observe the type of corrosive attack.

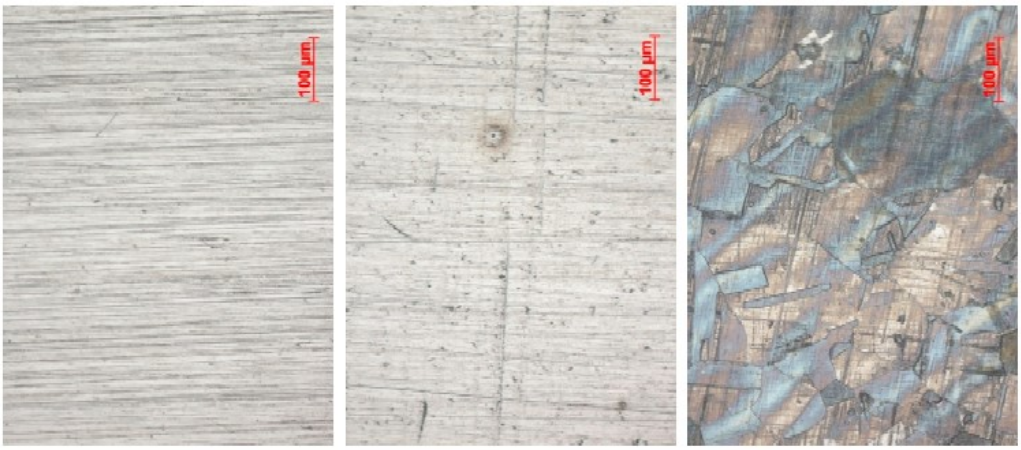

(a) (b) (c)

Figure 4.1: Optical image of corrosive attack of austenitic stainless steel 17Cr12Ni2Mo after exposure to different pH in 30,000 ppm Cl^- at 30 °C for 24 h, pH adjustment with HCl, (a) pH 4: no corrosion, (b) pH 3: pitting corrosion, (c) pH 0: uniform corrosion, published in [98]

Immersion tests have shown different types of attack such as uniform corrosion and pitting corrosion. Specimens tested under milder conditions (higher pH values) showed no corrosive attack. Figure 4.1 [98] gives an example of three specimens with different appearance after the immersion tests.

In the 0.00833 % NaCl solution uniform corrosion occurred only at pH 2 or lower while pitting corrosion only occurred at pH 3 or lower (Table 4.1). The steels with higher PREN values resulted in uniform corrosion occurring at lower pH values. Pitting corrosion similarly occurred at lower pH values for steels with a higher PREN value, with the exception of 22Cr5Ni3Mo steel, where it occurred at a higher pH value (pH 2) compared to the less alloyed 17Cr12Ni2Mo steel (pH 1). Table 4.1 shows the type of attack for all steels occurring in the least aggressive solution, in relation to pH value.

Table 4.1: Type of corrosive attack after 24 hour immersion in 0.00833 % NaCl solution at 30 °C with HCl addition. Legend: u – uniform corrosion, p – pitting corrosion, n – no corrosion

Steel	pH 0	pH 1	pH 2	pH 3	pH 4	pH 5	pH 6	PREN
13Cr		u	u	p	n	n	n	12.7
13Cr6Ni2Mo	u	u	p	n	n	n		19.9
15Cr6Ni2Mo	u	u	p	n	n			21.4
17Cr4Ni2Mo	u	p	p	n	n			25.3
17Cr12Ni2Mo	u	p	n	n	n			26.0
22Cr5Ni3Mo	u	p	p	n				34.5
20Cr24Ni6Mo	u	n	n					42.5

The pH values where uniform and pitting corrosion occurs were expected to change as the solution aggressiveness increases. The first increase in solution aggressiveness was a higher salt concentration, which directly increased the chloride concentration of the solution. Table 3.3 shows the increase of chloride concentration of the NaCl solutions as the pH is decreased by means of HCl addition. The chloride concentration of 0.00833 % NaCl solution has not significantly changed until reaching pH 2, followed by an increase by approximately one order of magnitude for each pH decrease. The 5 % NaCl solution results in a significant increase of chloride concentration only upon reaching pH 0.

Table 4.2 shows the type of corrosion found on specimens after immersion in 5 % NaCl at 30 °C. As was the case with the immersion tests in 0.00833 % NaCl solution at 30 °C, higher alloyed steels had a better resistance to uniform corrosion, always resulting in uniform corrosion at lower pH values compared to less alloyed steels. Pitting corrosion generally occurred at pH 3, with the exceptions of 13Cr steel, where pitting occurred at pH 4, 15Cr6Ni2Mo steel, where pitting occurred at pH 2 and 20Cr24Ni6Mo steel, where pitting was not detected in after immersion in any of the tests. Comparing the results from Tables 4.1 and 4.2 one can see that the increase in chloride content resulted in an increase of solution pH value required for uniform and/or pitting corrosion to occur in most cases (the exceptions being 15Cr6Ni2Mo and 20Cr24Ni6Mo steels).

Table 4.2: Type of corrosive attack after 24 hour immersion in 5 % NaCl solution at 30 °C with HCl addition. Legend: u – uniform corrosion, p – pitting corrosion, n – no corrosion

Steel	pH 0	pH 1	pH 2	pH 3	pH 4	pH 5	pH 6	PREN
13Cr		u	u	u	p	n		12.7
13Cr6Ni2Mo	u	u	u	p	n			19.9
15Cr6Ni2Mo	u	u	p	n				21.4
17Cr4Ni2Mo	u	u	p	p	n			25.3
17Cr12Ni2Mo	u	p	p	p	n			26.0
22Cr5Ni3Mo	u	p	p	p	n			34.5
20Cr24Ni6Mo	u	n	n					42.5

Table 4.3 shows the type of corrosion found on specimens after immersion in 5 % NaCl at 80 °C. In these conditions uniform corrosion again appears at lower pH values for more alloyed steel, with the exception of 22Cr5Ni3Mo versus 20Cr24Ni6Mo, where the less alloyed duplex steel suffers from uniform corrosion only at pH 0 while the more alloyed superaustenitic steel suffers from uniform corrosion already at pH 1. Pitting corrosion seems to also appear at higher pH values for less alloyed steels, with the exception of 13Cr steel, which shows no corrosion at pH 5 (only rouging) while 13Cr6Ni2Mo and 15Cr6Ni2Mo resulted in pitting at pH 5. Comparing data obtained from immersion tests performed in 5 % NaCl solutions at 30 and 80 °C (Tables 4.2 and 4.3), we can see that uniform and/or pitting corrosion usually occurred at higher pH values in the case of an increase in temperature.

Table 4.3: Type of corrosive attack after 24 hour immersion in 5 % NaCl solution at 80 °C with HCl addition. Legend: u – uniform corrosion, p – pitting corrosion, n – no corrosion

Steel	pH 0	pH 1	pH 2	pH 3	pH 4	pH 5	pH 6	PREN
13Cr			u	u	p	n	n	12.7
13Cr6Ni2Mo			u	p	p	p	n	19.9
15Cr6Ni2Mo		u	p	p	p	p	n	21.4
17Cr4Ni2Mo		u	p	p	n			25.3
17Cr12Ni2Mo	u	u	p	p	n			26.0
22Cr5Ni3Mo	u	p	p	n	n			34.5
20Cr24Ni6Mo	u	u	n					42.5

Table 4.4: pH before and after each immersion test in 0.00833 % NaCl solution at 30 °C

Steel	pH	pH 0	pH 1	pH 2	pH 3	pH 4	pH 5	pH 6
13Cr	before		1.02	1.98	3.02	4.02	4.96	5.60
	after		1.41	2.24	3.15	4.37	5.23	5.53
13Cr6Ni2Mo	before	0.01	1.00	1.99	3.00	3.99	5.00	
	after	0.10	1.05	2.00	3.00	4.02	5.31	
15Cr6Ni2Mo	before	0.03	0.99	2.00	3.01	3.99		
	after	0.02	1.00	2.00	3.00	4.02		
17Cr4Ni2Mo	before	0.03	1.00	2.01	3.02	4.02		
	after	0.03	1.00	2.00	3.00	4.04		
17Cr12Ni2Mo	before	0.00	1.01	1.99	3.00	3.99		
	after	-0.02	0.99	1.88	3.00	3.98		
22Cr5Ni3Mo	before	0.01	0.97	1.98	3.00			
	after	0.02	0.96	2.00	2.65			
20Cr24Ni6Mo	before	0.00	1.01	1.99				
	after	-0.02	0.98	2.00				

In the case of the 22Cr5Ni3Mo steel at 80 °C, pitting was detected at a lower pH value than at 30 °C, showing the stochastic nature of pit nucleation and the drawback of short term immersion tests.

Although changing sodium chloride concentration from 0.0083 to 5 % (Table 4.1 to 4.2) and increasing temperature form 30 to 80 °C (Table 4.2 to 4.3) mean also certain steps towards more aggressive conditions this did not always result in a certain type of corrosion occurring at a higher pH value. Consequently the Tables 4.1 to 4.3 have to be interpreted by tendencies. For pitting there is a certain initiation time and for uniform corrosion there is also a certain delay of initial attack since the passive layer has to be dissolved before the alloy is attacked. The consequence of these delays and initiation times, along with inhomogeneous alloys and conditions are inconsistent results, especially during short term experiments.

The pH values of the solutions were measured before and after testing. Tables 4.4, 4.5 and 4.6 show the pH values before and after each immersion test.

Table 4.5: pH before and after each immersion test in 5 % NaCl solution at 30 °C

Steel	pH	pH 0	pH 1	pH 2	pH 3	pH 4	pH 5	pH 6
13Cr	before		0.97	No data	No data	No data	4.98	
	after		1.00	No data	No data	No data	5.86	
13Cr6Ni2Mo	before	-0.05	1.02	1.96	2.99	3.96		
	after	0.01	1.39	2.11	3.03	3.99		
15Cr6Ni2Mo	before	0.04	0.94	1.96	2.95			
	after	0.01	1.01	1.96	2.97			
17Cr4Ni2Mo	before	0.00	0.97	2.00	3.00	3.94		
	after	0.03	1.36	1.99	3.00	4.05		
17Cr12Ni2Mo	before	0.01	0.99	2.00	3.00	3.94		
	after	0.03	0.95	1.99	3.00	4.05		
22Cr5Ni3Mo	before	0.01	0.99	2.00	2.99	3.94		
	after	0.04	0.96	1.98	2.95	4.05		
20Cr24Ni6Mo	before	-0.05	1.02	1.96				
	after	0.00	1.03	1.97				

Table 4.6: pH before and after each immersion test in 5 % NaCl solution at 80 °C

Steel	pH	pH 0	pH 1	pH 2	pH 3	pH 4	pH 5	pH 6
13Cr	before			1.99	2.99	4.01	5.02	5.90
	after			3.80	5.00	5.17	5.64	6.11
13Cr6Ni2Mo	before			1.98	2.98	3.99	5.00	5.92
	after			2.00	3.00	4.30	5.39	5.97
15Cr6Ni2Mo	before		1.01	1.98	2.97	3.99	5.02	5.97
	after		1.61	1.97	2.97	3.97	5.47	6.02
17Cr4Ni2Mo	before		1.03	1.97	2.99	4.01		
	after		1.34	1.96	2.98	4.09		
17Cr12Ni2Mo	before	-0.04	0.99	1.94	3.05	3.98		
	after	-0.01	1.02	1.96	2.95	3.97		
22Cr5Ni3Mo	before	-0.02	1.01	1.99	2.98	4.01		
	after	-0.01	0.99	1.93	2.95	3.98		
20Cr24Ni6Mo	before	-0.04	0.99	1.94				
	after	0.00	1.03	1.96				

In most experiments the pH value remained unchanged. Large pH changes (> 0.3) were almost always an increase in pH (alkalization) with the exception of 22Cr5Ni3Mo in 0.00833 % NaCl at pH 3, where a decrease of pH was logged. In most of the cases, where the solution pH changed during the test some type of corrosion has taken place (either pitting or uniform corrosion). The largest pH changes occurred at the elevated temperature of 80 °C (Table 4.6). Particularly large pH changes were logged with immersion of 13Cr at pH 2, pH 3 and pH 4, which may be explained due to corrosion. When metal dissolution takes place at the anodic site, the corresponding cathode will result in an increase of pH according to H^+ consumption.

Some similar effect may have occurred during immersion of 13Cr at pH 5 and pH 6 – although no pitting corrosion was found on the surface, the sample has undergone rouging, which in essence means deposition of oxides.

At 80 °C apart from the cases described above and where 15Cr6Ni2Mo and 17Cr4Ni2Mo were corroding uniformly, the changes to the electrolyte pH occurred for 13Cr6Ni2Mo at pH 4 and

pH 5 as well as 15Cr6Ni2Mo at pH 5. In all three cases a strong local corrosive attack was present at the corner or edge of the specimen.

Figure 4.2 shows an optical microscopy image along with three SEM images made on 13Cr6Ni2Mo sample after immersion in pH 5 solution.

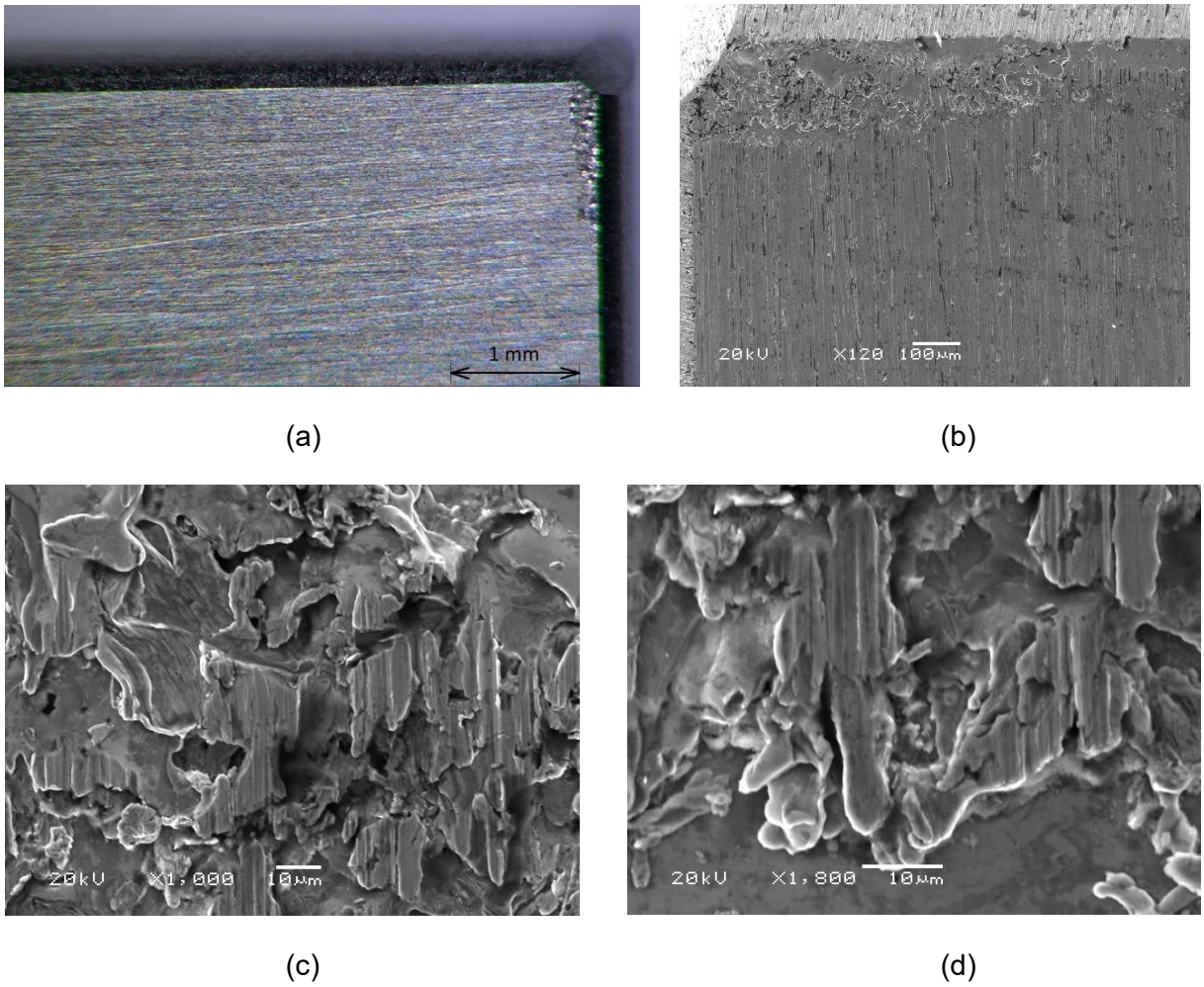

Figure 4.2: Optical microscopy image (a) and SEM images at 120x magnification (b), 1000x magnification (c) and 1800x magnification (d) of 13Cr6Ni2Mo sample after immersion in 5 % NaCl solution at 80 °C, pH 5, 24 h

The corrosion that appeared at the edge of the sample shown in Figure 4.2 is the only place, where corrosion has occurred and similar corrosive attacks have occurred in the other two cases (13Cr6Ni2Mo at pH 4, 15Cr6Ni2Mo at pH 5) where uniform corrosion was not present and the solution pH changed. The present moderate corrosive attack results in an increase of pH from 4 or 5 towards 4.5 or 5.5. A corrosive attack that looks quite similar was reported by Moshaweh and Burstein after 100 ks of potentiostatic cathodic polarization [99]. Still, since

most of the surface remained unaffected it is obviously a localized attack, which is, why it was decided to mark it as pitting corrosion in Table 4.3.

4.2 Potentiodynamic tests

Potentiodynamic tests allow extraction of many electrochemical parameters, which describe corrosion properties of a metal in a certain electrolyte. The data obtained are usually used to interpret the corrosion behavior in a single metal/electrolyte combination. In the following, special focus is paid on comparing the results among different stainless steels and under different electrolyte conditions. Electrochemical parameters are used as a guideline to perform other experiments and to compare with results gained from other experiments as well as with reported literature data.

Figures 4.3, 4.4, 4.5 and 4.6 are collections of polarization curves obtained for all steels in the four mentioned media (low – high chloride concentration, low – high temperature). In each of these figures the seven investigated stainless steels are comparably shown. Figures 4.3 to 4.6 are all drawn with same scales of axis to enable good comparability between different media.

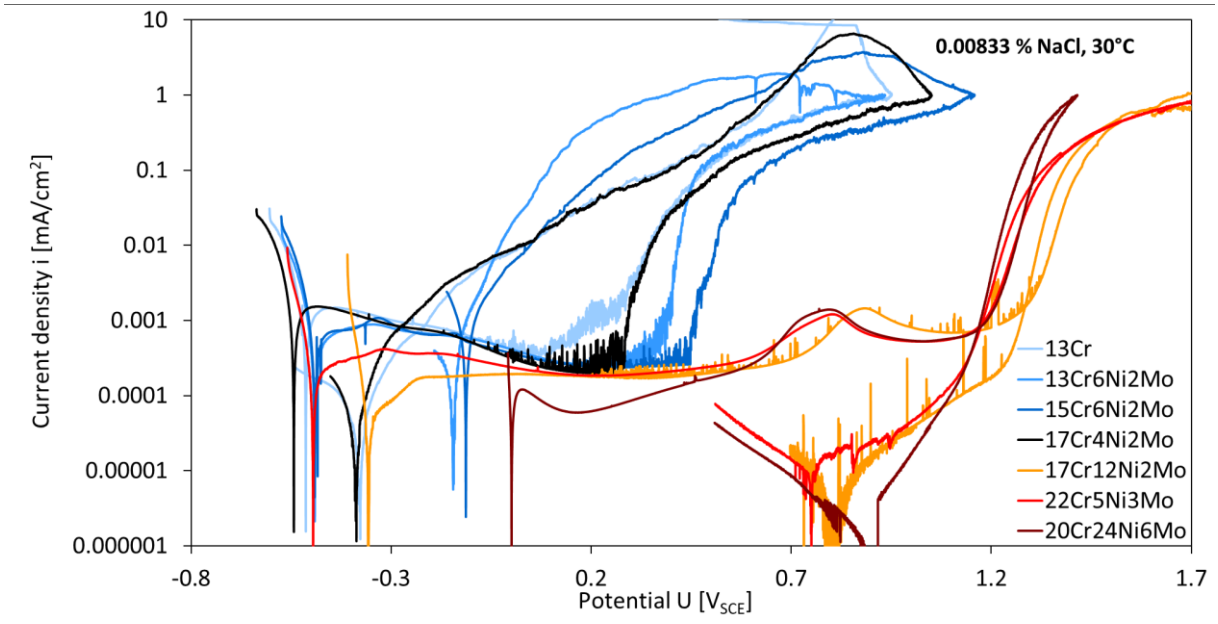

Figure 4.3: Potentiodynamic polarization curves of all investigated steels in 0.00833 % NaCl solution at 30 °C, 1 bar CO_2

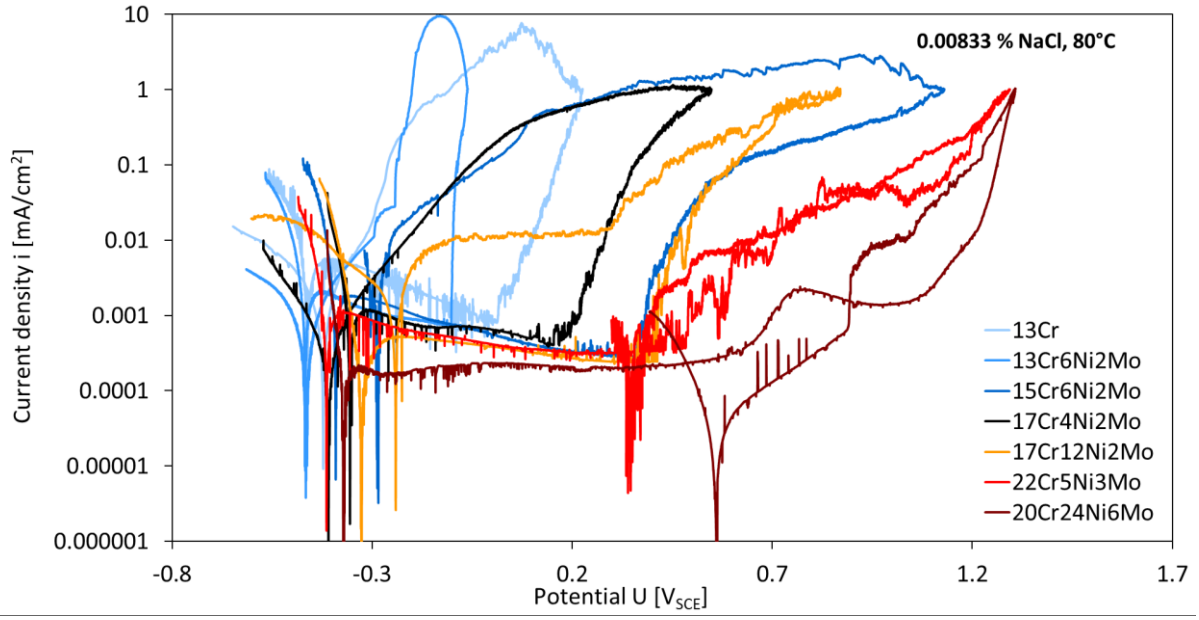

Figure 4.4: Potentiodynamic polarization curves of all investigated steels in 0.00833 % NaCl solution at 80 °C, 1 bar CO_2

Figure 4.3 shows measurements from tests performed on all steels in a 0.00833 % NaCl brine at 30 °C, purged with CO_2. One can see all steels have a similar passive current density. Stainless steels 13Cr, 13Cr6Ni2Mo, 15Cr6Ni2Mo and 17Cr4Ni2Mo steels show a more narrow passivity range than the other three steels. While the latter three (austenitic and duplex stainless steels) show no hysteresis indicating electrolyte decomposition or uniform corrosion at very high potentials, the 13Cr stainless steel and the three heat treated modified variants show pronounced pitting with a hysteresis. The hysteresis is a good indicator for acidification inside the pits.

Comparing Figure 4.3 to Figure 4.4 one can notice that passivity ranges of some alloys have narrowed, namely for 13Cr, 13Cr6Ni2Mo, 17Cr12Ni2Mo and 22Cr5Ni3Mo. Additionally, the passive current density of 13Cr has increased, particularly close to the corrosion potential (small peak right of OCP for 13Cr).

With an increase of chloride concentration the curves change to a larger extent. Comparing Figure 4.5 to Figure 4.3 it can be seen that the effect of chloride content is quite severe on all steels. The 13Cr steel shows a very short passive range as well as a very high passive current density, increasing with potential. There is a small narrowing of the passive range for 13Cr6Ni2Mo, 15Cr6Ni2Mo and 17Cr4Ni2Mo and a large narrowing for 17Cr12Ni2Mo. Only steels 22Cr5Ni3Mo and 20Cr24Ni6Mo remain almost unaffected by the temperature increase.

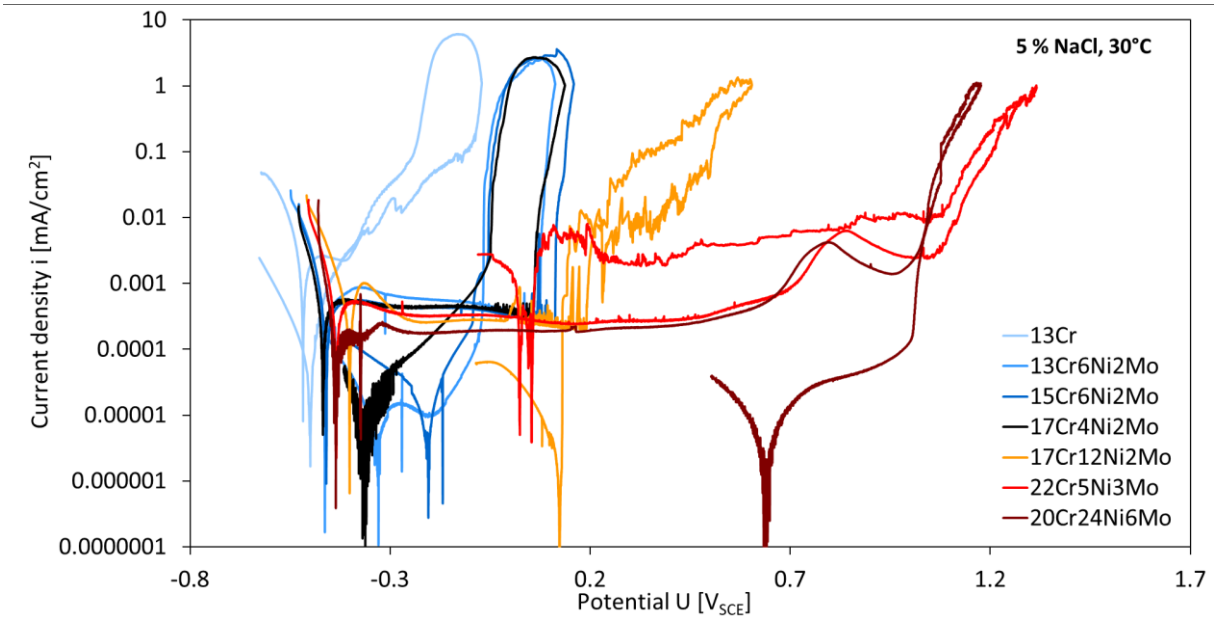

Figure 4.5: Potentiodynamic polarization curves of all investigated steels in 5 % NaCl solution, 30 °C, 1 bar CO_2

In Figure 4.6 polarization scans of all steels in the high chloride, high temperature conditions are shown. Compared to the lower temperature 5 % NaCl solution, we can see a further increase in the passive current density of 13Cr.

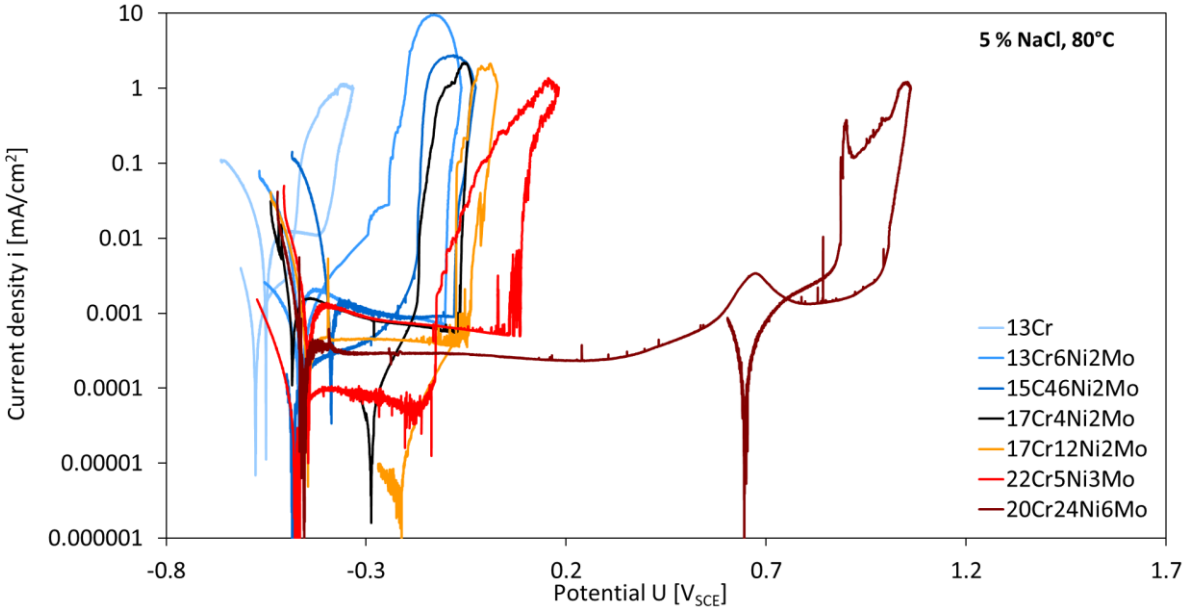

Figure 4.6: Potentiodynamic polarization curves of all investigated steels in 5 % NaCl solution, 80 °C, 1 bar CO_2

The passive ranges of 13Cr6Ni2Mo, 15Cr6Ni2Mo, 17Cr4Ni2Mo and 17Cr12Ni2Mo become even narrower and the passive ranges of 22Cr5Ni3Mo narrows significantly from formerly ~1.45 V at 30 °C to ~0.5 V at 80 °C. Finally, a small increase in passive current density of 13Cr6Ni2Mo, 15Cr6Ni2Mo, 17Cr4Ni2Mo and 22Cr5Ni3Mo is noticeable. Superaustenitic stainless steel 20Cr24Ni6Mo is the only investigated material, which remains fully corrosion resistant under these conditions, although a small hysteresis is noticeable.

The main electrochemical parameters are compiled in Tables 4.7 to 4.9, where:

- E_{corr} is the corrosion potential – the potential at which the cathodic current changed into an anodic current,
- i_{corr} is the corrosion current density, obtained with the help Tafel slopes,
- E_{pp} is the primary passivation potential – close to the corrosion potential, this is the potential at which the anodic current density begins decreasing until a passive current density is reached,
- E_b is the breakthrough potential – this is the potential at which the anodic current density begins sharply increasing and it marks the end of the passive potential range,
- E_{rep} is the repassivation potential – this is the potential where the "backward" scan curve intersects the "forward" scan curve inside the passive potential range. Since the current density is decreased below the passive current density at this potential, it is considered that all pitting corrosion, which occured during the experiment has repassivated once this potential was reached,
- ΔE is the passive potential interval – the difference between breakthrough potential and passivation potential. A large passive potential interval indicates good resistance to corrosion
- $E_{rep} – E_{corr}$ is the difference between the repassivation potential and corrosion potential. This difference indicates how resistant the steel is to pitting corrosion in the given environment, with a large difference indicating good resistance.

The corrosion potential in the 0.00833 % NaCl solution at 30 °C was very high in the case of 20Cr24Ni6Mo steel – despite repeating this measurement several times the same result was obtained. Despite this, the other parameters show very good resistance to the given environment. All steels show a very large passive potential interval (above 700 mV) and a large difference between repassivation and corrosion potentials (above 250 mV).

Table 4.7: Electrochemical parameters obtained from all investigated steels during potentiodynamic tests in 0.00833 % NaCl solution at 30 °C, deaerated with CO_2

Steel	E_{corr} [mV_{SCE}]	i_{corr} [$\mu A/cm^2$]	E_{pp} [mV_{SCE}]	E_b [mV_{SCE}]	E_{rep} [mV_{SCE}]	ΔE [mV]	$E_{rep} - E_{corr}$ [mV]
13Cr	-514	0,68	-560	263	-220	823	294
13Cr6Ni2Mo	-491	0,34	-342	385	-125	727	366
15Cr6Ni2Mo	-492	0,59	-334	449	-101	783	391
17Cr4Ni2Mo	-543	0,79	-483	278	-275	761	268
17Cr12Ni2Mo	-357	0,04	-220	1305	1283	1525	1640
22Cr5Ni3Mo	-495	0,14	-317	1187	1175	1504	1670
20Cr24Ni6Mo	0	0,11	25	1201	1169	1176	1168

In Table 4.8 the steels containing nickel and molybdenum all show good corrosion resistance. The 13Cr steel exhibits a relatively high corrosion current density, as well as a very short passive potential interval and a small difference between repassivation and corrosion potentials, indicating the steel would suffer from pitting corrosion in such conditions.

Table 4.8: Electrochemical parameters obtained from all investigated steels during potentiodynamic tests in 5 % NaCl solution at 30 °C, deaerated with CO_2

Steel	E_{corr} [$mV_{Ag/AgCl}$]	i_{corr} [$\mu A/cm^2$]	E_{pp} [$mV_{Ag/AgCl}$]	E_b [$mV_{Ag/AgCl}$]	E_{rep} [$mV_{Ag/AgCl}$]	ΔE [mV]	$E_{rep} - E_{corr}$ [mV]
13Cr	-518	1.45	-482	-401	-422	81	96
13Cr6Ni2Mo	-464	0.28	-377	74	-69	451	395
15Cr6Ni2Mo	-460	0.31	-387	112	-93	499	367
17Cr4Ni2Mo	-468	0.29	-424	57	-128	481	340
17Cr12Ni2Mo	-402	0.35	-373	189	130	562	532
22Cr5Ni3Mo	-435	0,3	-390	1063	59	1453	494
20Cr24Ni6Mo	-436	0,14	-318	990	1077	1308	1340

Table 4.9 shows that an increase in temperature further affects electrochemical parameters. The corrosion current density of 13Cr steel is further increased compared to the result of the 30 °C experiment, while the passive potential interval and difference between repassivation and corrosion potential remains mostly unchanged. The 13Cr6Ni2Mo and 15Cr6Ni2Mo steels retained a respectable passive potential interval (around 300 mV), while the difference between repassivation and corrosion potential has decreased significantly in comparison to the data obtained from their respective 30 °C tests. Thus, we can expect good corrosion resistance of the passive layer, however pitting corrosion is expected to occur.

Table 4.9: Electrochemical parameters obtained from all investigated steels during potentiodynamic tests in 5 % NaCl solution at 80 °C, deaerated with CO_2

Steel	E_{corr} [mV_{SCE}]	i_{corr} [$\mu A/cm^2$]	E_{pp} [mV_{SCE}]	E_b [mV_{SCE}]	E_{rep} [mV_{SCE}]	ΔE [mV]	E_{rep} - E_{corr} [mV]
13Cr	-550	5,8	-509	-404	-480	105	70
13Cr6Ni2Mo	-468	1,25	-436	-102	-411	334	57
15Cr6Ni2Mo	-388	1,14	-364	-80	-229	284	159
17Cr4Ni2Mo	-485	0,86	-456	-66	-190	390	295
17Cr12Ni2Mo	-445	0,31	-415	-46	-75	369	370
22Cr5Ni3Mo	-445	0,75	-405	86	-125	491	320
20Cr24Ni6Mo	-455	0,283	-419	985	750	1404	1205

4.3 Scratch tests

Since the HRU/ZRA system used for measurements is reliant upon a 220 V 50 Hz AC power supply, it introduces noise into the current measurements with a 50 Hz frequency. While these fluctuations are in the small range of ± 0.5 µA when using a current range of 1 mA (required to record entire scratch transient), the scratch area is very small (approximately 0.7 mm^2 in average). This means the small current fluctuations translates into relatively large current density changes (± 0.07 mA/cm^2). To reduce the amount of noise a Savitzky-Golay filter was employed. A typical current measurement before and after filtering is seen in Figure 4.7.

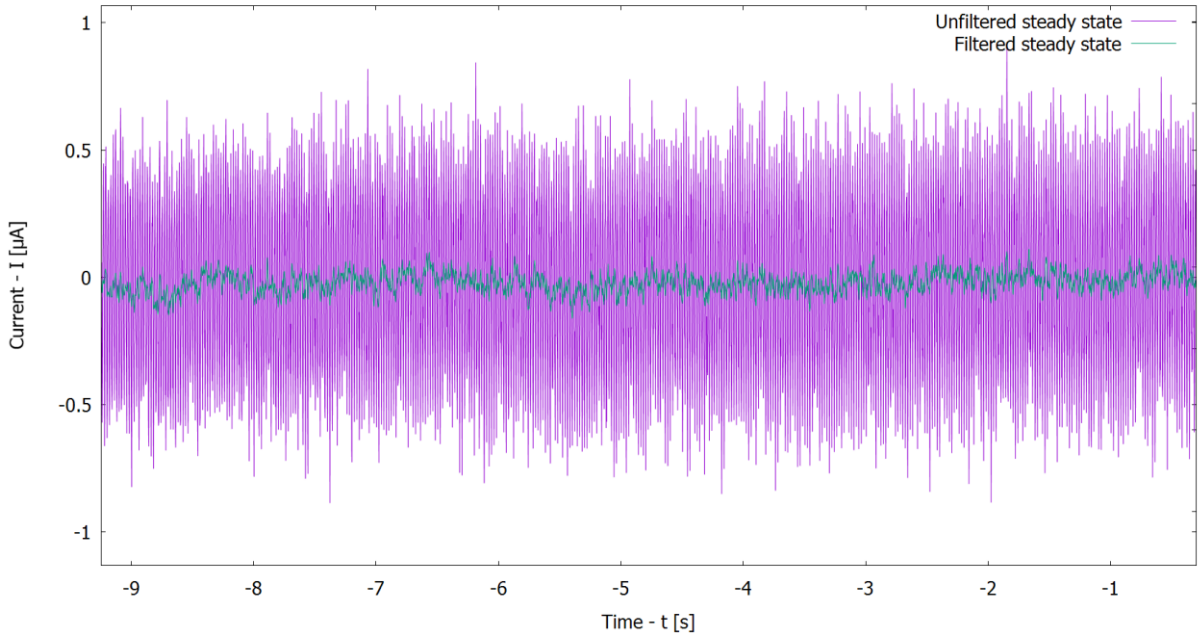

Figure 4.7: Current versus time diagram immediately before scratch creation. Purple line represent unfiltered data and green line represent data after applying a Savitzky-Golay filter

To investigate the current transient created by the scratch event, it was decided to combine an unfiltered current peak with a filtered current decay after the scratch event. This was done at a time when there is a small difference between the unfiltered and filtered current value during the current decay after scratch creation. Since most scratch events lasted less than 30 ms and the measurements should be plotted in a log (i) vs log (t) diagram to effectively examine the results, it was decided to plot the current measurements in such a way that the scratch event ends at a time of t = 0.030 s. This would mean that the unfiltered current was observed to a time betweeen 0.050 s and 0.060 s. Figure 4.8 shows a filtered and unfiltered current measurement obtained by a scratch test, along with the point, where the two measurements were combined to create a final curve. This procedure was done for all measurements and results presented in this work will contain only current density values obtained from such a combined current transient.

All following results of scratch tests are presented as double logarithmic current density - time graphs. The slope of the current density decrease (α in equation 12) indicates repassivation kinetics, the far right "final" current density the stadium that is reached after 100 s of repassivation. As Burstein and Daymond have inadvertently discovered during their study about the effect of temperature cycling on the passivity of 316L grade stainless steel in sulphuric acid solution, it is still unsure, what a final state of passivity actually is [100]. Due to this, the "final" current density is simply decided to be at a time well above the time required

for the current density to decrease significantly after the scratch event but short enough to allow relatively small file sizes and fast data processing.

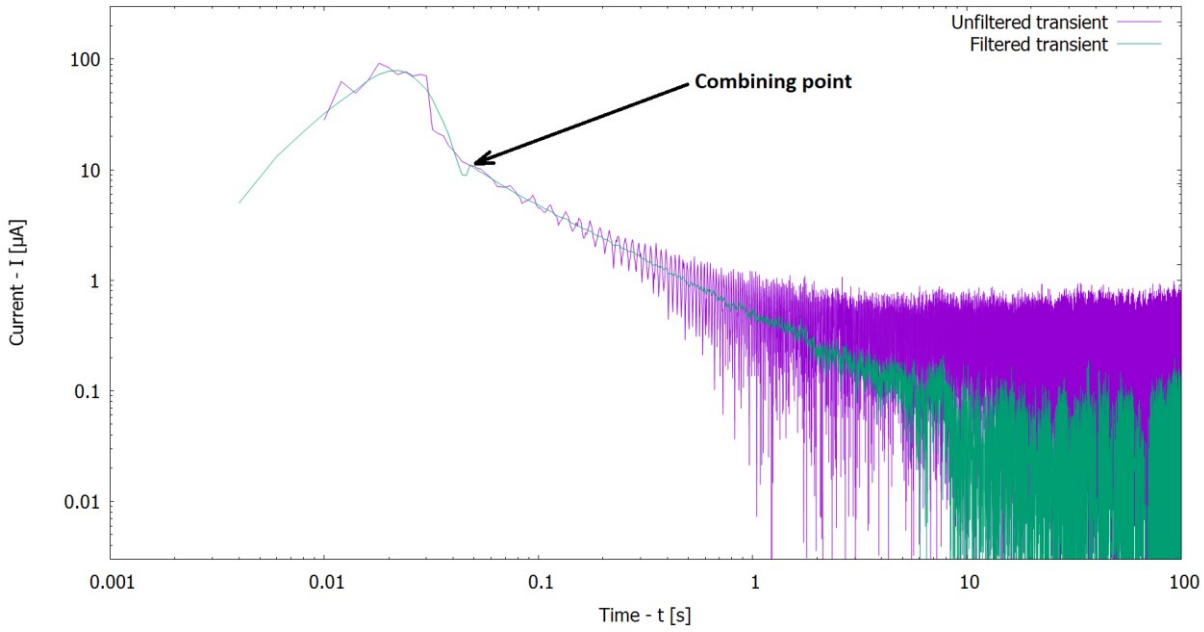

Figure 4.8: Current versus time diagram during and after scratch creation, purple line represents unfiltered data and green line represents data after applying a Savitzky-Golay filter. Unfiltered data are used until reaching combining point, after which filtered data are used

The 13Cr steel is the lowest alloyed steel investigated, containing no nickel or molybdenum to (beside 13 % Cr further) improve corrosion resistance. As such, the steel is expected to repassivate slower in comparison to other steels (hypothesis).

Figures 4.9 and 4.10 show current and potential changes of 13Cr steel in 5 % NaCl solution at 30 °C with the pH of the solution set to 5 and 4, respectively. In these cases the current density did not reach a value close to 0 within the 100 seconds of measurement and the repassivation slope during the current decay changed over time. The potential decreased during the scratch event indicating activation. However, it did not change much during the current decay phase. This steel has shown very little difference in the maximum current peak across all experiments and the kinetics of the current decay was similar for all cases regardless of the solution pH value. This is valid for both pH levels showing also repeatability of results. It seems that 13Cr stainless steel under these conditions cannot fully repassivate within the 100 s measurement, since the decrease of corrosion current density does not progress but seems to level out between 10^{-5} and 10^{-4} A/cm^2.

For means of complete data presentation the potential during scratching is shown in the figures, but due to the minor importance they are not discussed in detail in the following text. The potential measurements are marked with thin lines and are color coded to match their corresponding current density curves.

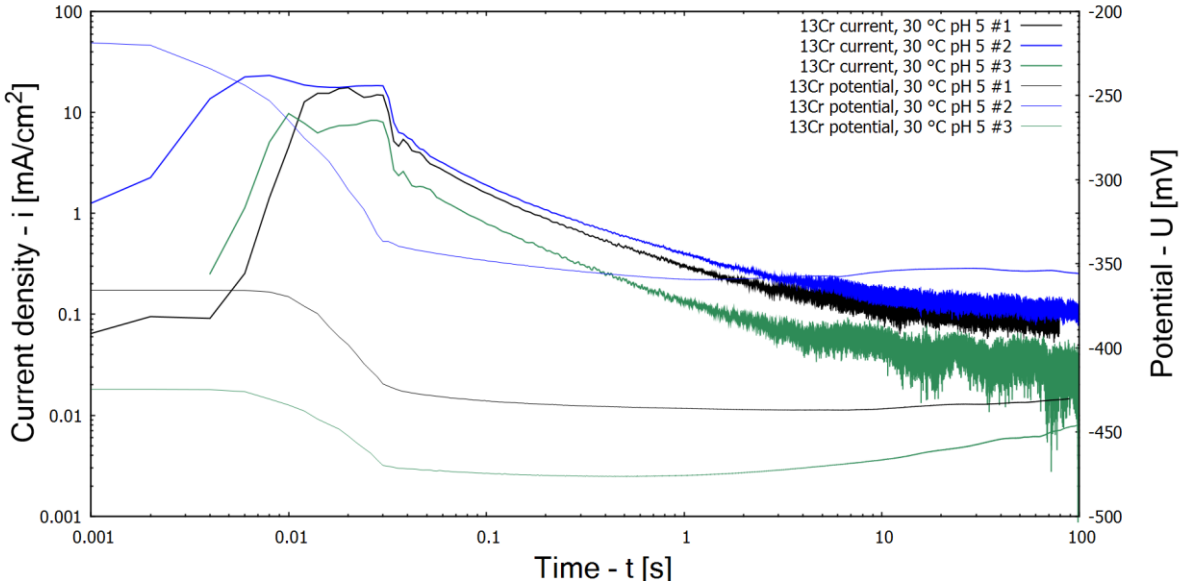

Figure 4.9: Current density (thick lines) and potential (thin lines) transients obtained from scratching 13Cr steel in 5 % NaCl solution at 30 °C, pH 5, 1 bar Ar

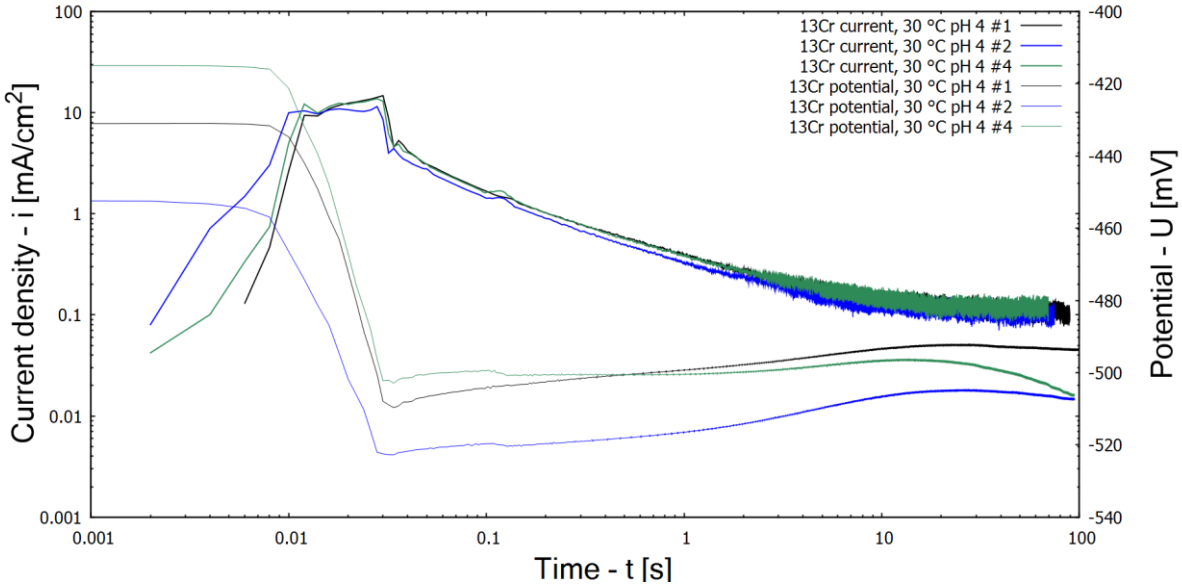

Figure 4.10: Current density and potential transients obtained from scratching 13Cr steel in 5 % NaCl solution at 30 °C, pH 4, 1 bar Ar

Unlike the 13Cr steel, the 13Cr6Ni2Mo steel contains some alloying elements other than chromium, which should improve repassivation. Figure 4.11 shows a set of measurements obtained by scratching this steel grade in pH 3 solution at 30 °C, which has resulted in a decrease of current density to very low values within the 100 s measurement. Along with the current density decrease, the potential increased close to the values before scratching, after the initial decrease during the scratch event. These two factors combined indicate a high degree of repassivation of the scratched areas within the 100 seconds of measurement. In the case of 13Cr6Ni2Mo steel the current decay slope (α) is not the same for all experiments. Current density after 100 s of repassivation reaches a value of 10^{-5} A/cm^2 or lower.

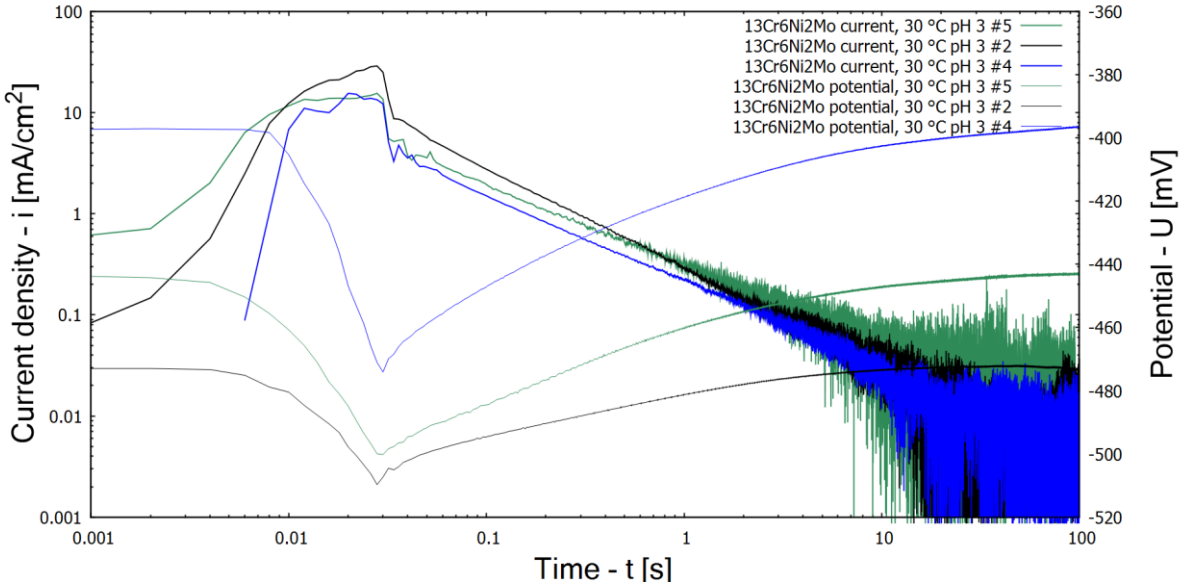

Figure 4.11: Current density and potential transients obtained from scratching 13Cr6Ni2Mo steel in 5 % NaCl solution at 30 °C, pH 3, 1 bar Ar

Figures 4.12, 4.13, 4.14 and 4.15 show sets of measurements performed on 15Cr6Ni2Mo, 17Cr4Ni2Mo, 17Cr12Ni2Mo and 22Cr5Ni3Mo steels in pH 3 solutions at 30 °C. It can be seen that all of the steels act similarly in regards to current peaks and current decay slopes varying in between individual experiments. Even the potential change during scratch creation varies on a case by case basis.

Current densities after 100 s of repassivation time are 10^{-5} A/cm^2 or lower for 15Cr6Ni2Mo, 17Cr4Ni2Mo, 17Cr12Ni2Mo and 22Cr5Ni3Mo steels.

The 20Cr24Ni6Mo steel has been scratched only once in pH 3 solution and several times in pH 2 solution. Figure 4.16 shows the scratches performed on 20Cr24Ni6Mo steel in pH 2 solution at 30 °C.

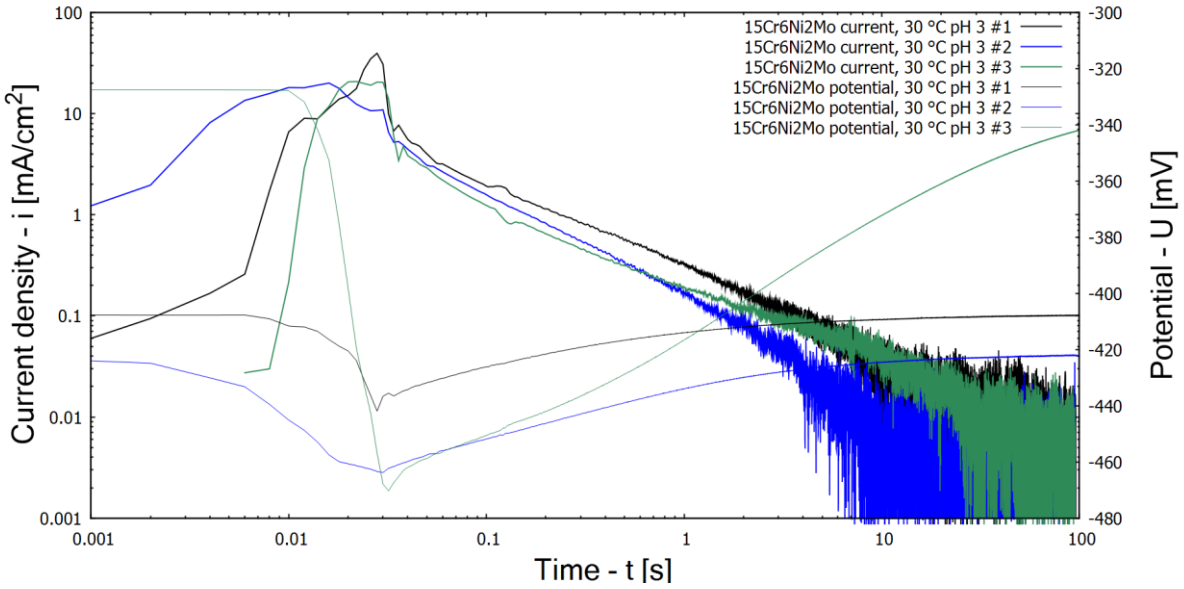

Figure 4.12: Current density and potential transients obtained from scratching 15Cr6Ni2Mo steel in 5 % NaCl solution at 30 °C, pH 3, 1 bar Ar

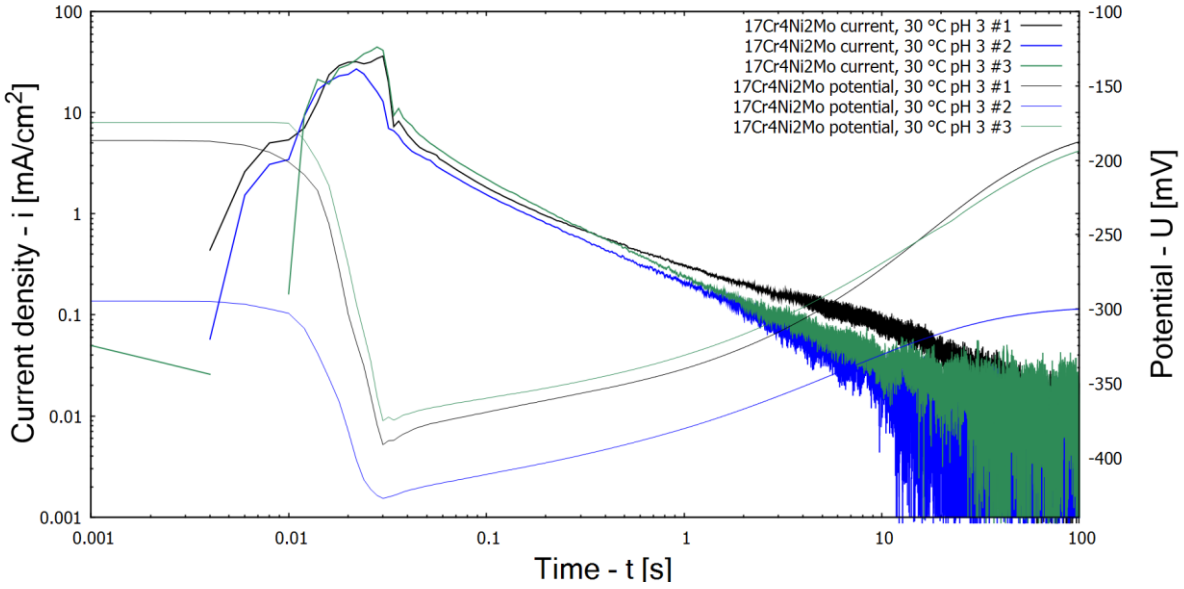

Figure 4.13: Current density and potential transients obtained from scratching 17Cr4Ni2Mo steel in 5 % NaCl solution at 30 °C, pH 3, 1 bar Ar

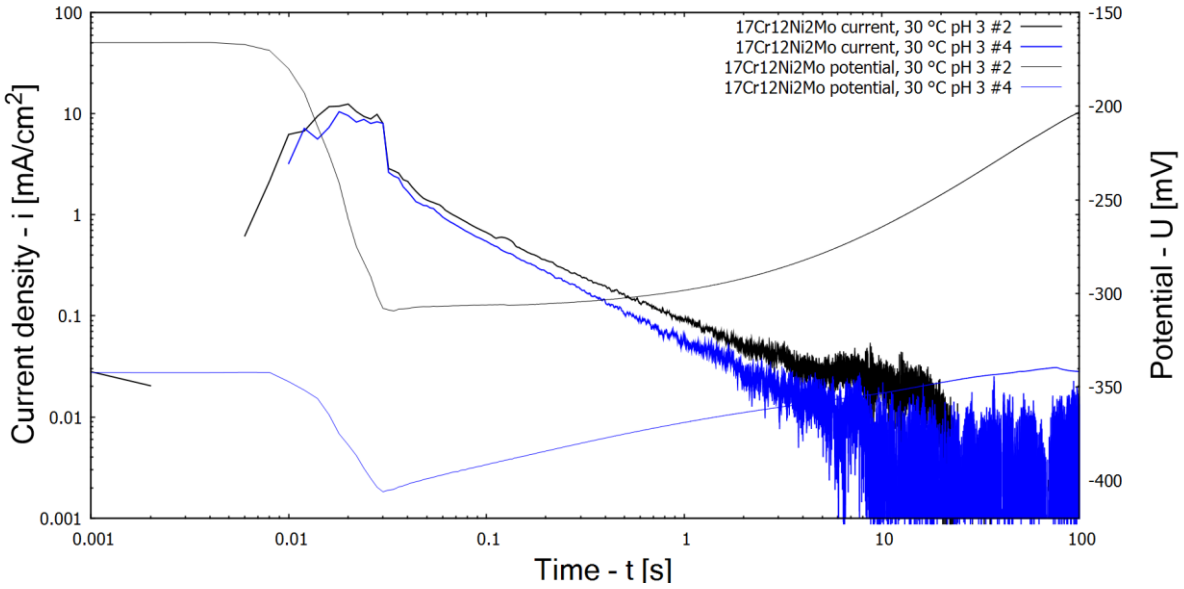

Figure 4.14: Current density and potential transients obtained from scratching 17Cr12Ni2Mo steel in 5 % NaCl solution at 30 °C, pH 3, 1 bar Ar

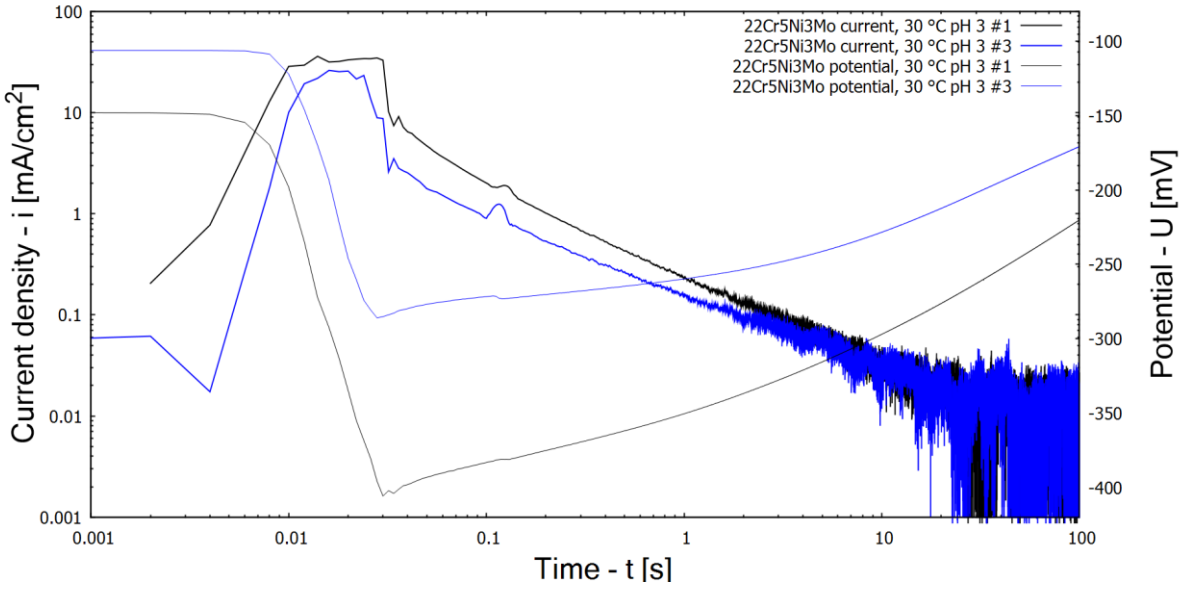

Figure 4.15: Current density and potential transients obtained from scratching 22Cr5Ni3Mo steel in 5 % NaCl solution at 30 °C, pH 3, 1 bar Ar

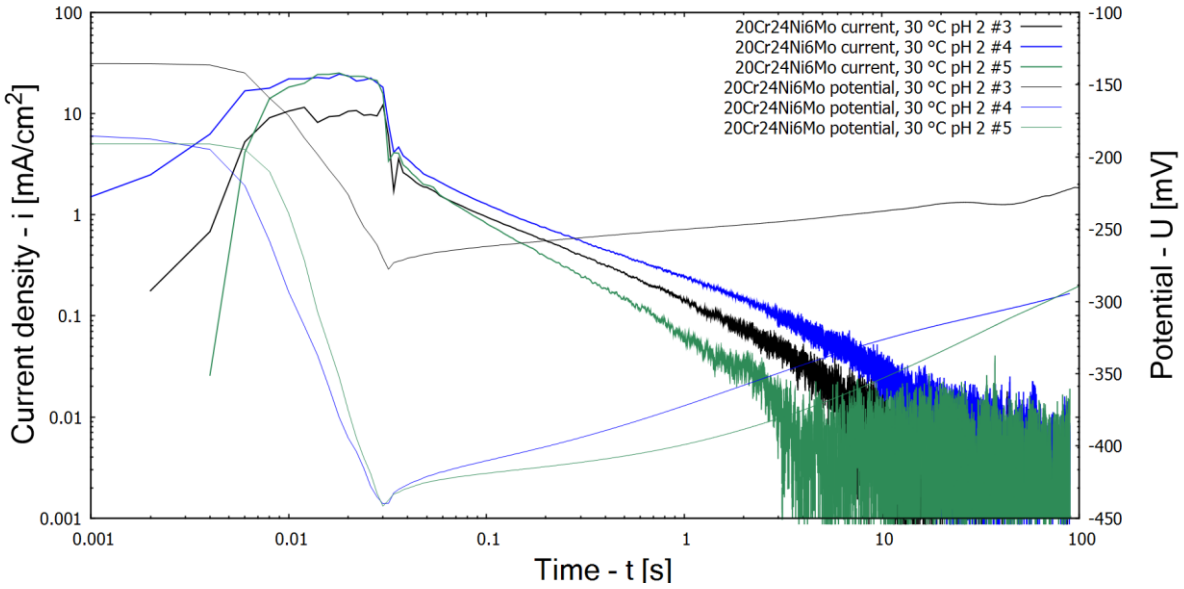

Figure 4.16: Current density and potential transients obtained from scratching 20Cr24Ni6Mo steel in 5 % NaCl solution at 30 °C, pH 2, 1 bar Ar

Both the current and potential acted very similar to all other measurements on steels containing nickel and molybdenum scratched in pH 3 solution, with usual variations in current peaks, current decay slopes and potential drops during scratch events. Even in this more aggressive solution the highest alloyed superaustenitic steel reached a current density of 10^{-5} A/cm^2 or lower within 100 s after the scratch event.

Table 4.10 details the current decay slopes (quantified as α in equation 12) between times 0.1 s < t < 1 s obtained from scratch tests shown in Figures 4.11 to 4.16. The reason for taking this time frame, although measured data are available until 100 s is that at low current densities below 10^{-4} A/cm^2 (times longer than 1 s) the measurement system is reaching its limits and the scatter of current density data becomes relatively large. Further argumentation is published in [98] and is also part of the discussion in chapter 5.

For all materials the current decay slope presented in Table 4.10 is similar and no clear distinction between materials can be made. This means that all materials repassivate at very similar rates. The Figures 4.11 to 4.16 show the same kinetics of repassivation within the first second after the scratch. For some materials there is finally a fade out of the repassivation process as can be seen for 13Cr already after 0.1 to 1 s. It seems that the highest alloyed superaustenitic stainless steel still has a better repassivation behavior at longer times, reaching lower current densities.

Table 4.10: Values of α obtained from scratch tests performed on 13Cr6Ni2Mo, 15Cr6Ni2Mo, 17Cr4Ni2Mo, 17Cr12Ni2Mo, 22Cr5Ni3Mo and 20Cr24Ni6Mo steels in 5 % NaCl solutions at 30 °C

Steel – solution pH	α_1	α_1	α_1	Mean α	PREN
13Cr6Ni2Mo – pH 3	0.8	0.83	0.97	0.867	19.9
15Cr6Ni2Mo – pH 3	0.78	0.78	0.97	0.843	21.4
17Cr4Ni2Mo – pH 3	0.78	0.86	0.96	0.867	25.3
17Cr12Ni2Mo – pH 3	0.86	0.98	-	0.92	26.0
22Cr5Ni3Mo – pH 3	0.78	0.93	-	0.855	34.5
20Cr24Ni6Mo – pH 2	0.70	0.82	1.07	0.863	42.5

Figure 4.17 shows the results of the scratch tests done at pH 2 (1 material in pH 3 solution) performed in 30 °C solution (potential was omitted in favor of a less cluttered graph). Namely, these were 15Cr6Ni2Mo steel in pH 2 solution, 17Cr4Ni2Mo steel in pH 2 solution, 17Cr12Ni2Mo steel in pH 2 solution, 22Cr5Ni3Mo steel in pH 2 solution and 20Cr24Ni6Mo steel in pH 3 solution (1 of each). It can be seen that the current transients produced from each steel grade are similar to their counterparts in a different pH solution.

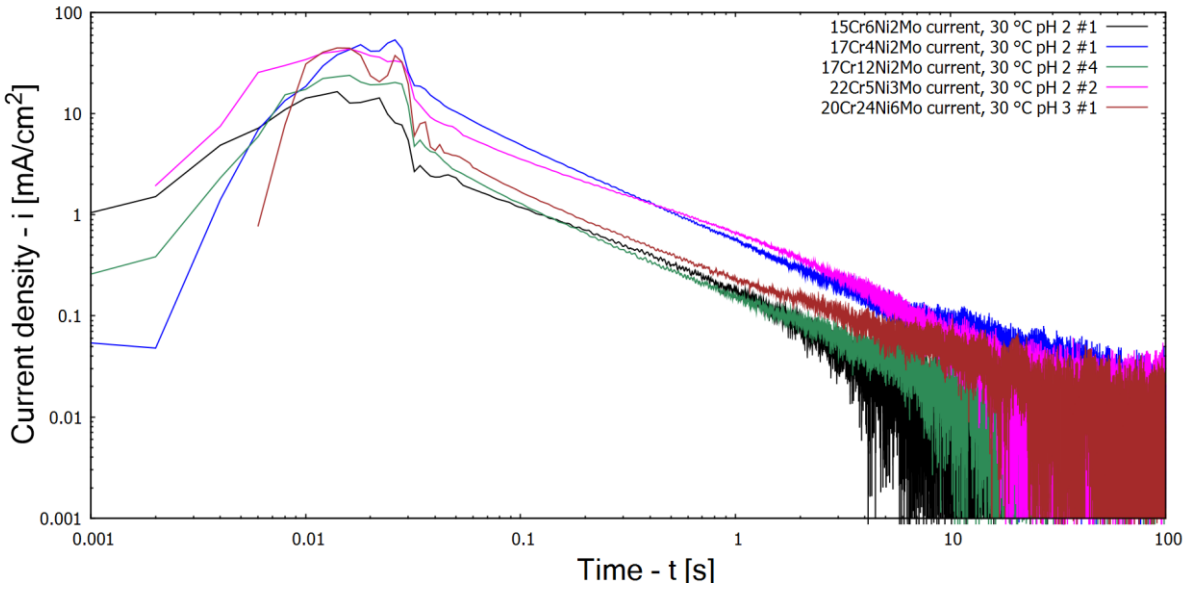

Figure 4.17: Current density transients obtained from scratching 15Cr6Ni2Mo, 17Cr4Ni2Mo, 17Cr12Ni2Mo and 22Cr5Ni3Mo steels in 5 % NaCl solution at 30 °C, pH 2 and 20Cr24Ni6Mo steel in 5 % NaCl solution at 30 °C, pH 3, 1 bar Ar

Selected scratches were performed in 80 °C solution, namely on 13Cr6Ni2Mo steel in pH 3 solution (3 scratches) and the superaustenitic 20Cr24Ni6Mo steel in pH 3 solution (1 scratch).

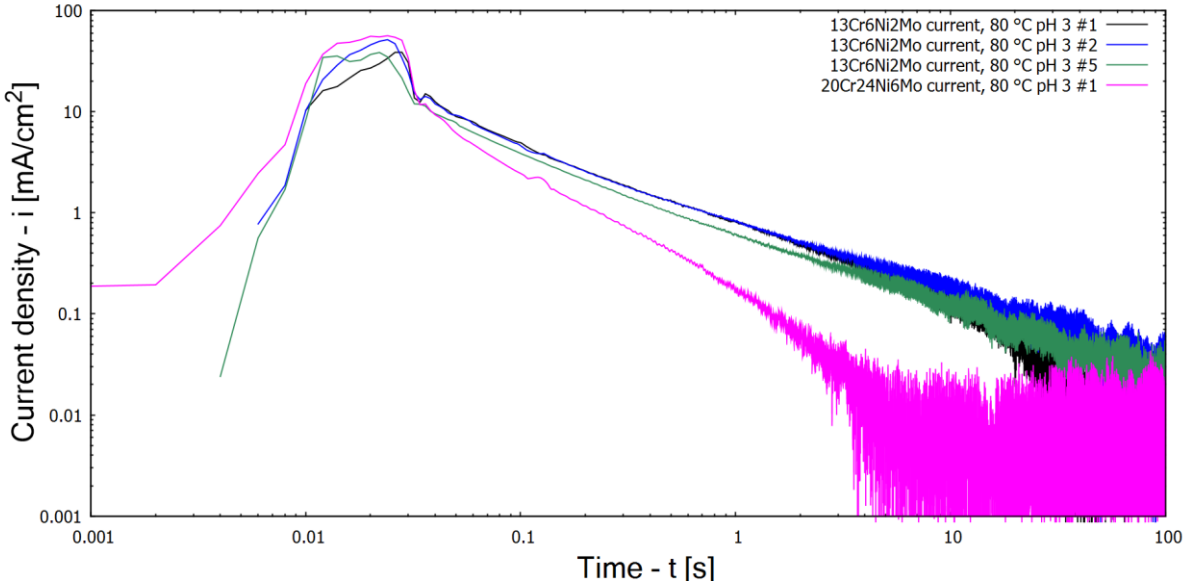

Figure 4.18: Current density transients obtained from scratching 13Cr6Ni2Mo and 20Cr24Ni6Mo steels in 5 % NaCl solution at 80 °C, pH 3, 1 bar Ar

Figure 4.18 shows the current transients obtained from these tests. In general the current peaks seem to be higher at this elevated temperature, leading to longer repassivation times. Only the superaustenitic material 20Cr24Ni6Mo still shows a fast repassivation rate, and reaching a current density of 10^{-4} A/cm^2 after 1 s and 10^{-5} to 10^{-6} A/cm^2 after 100 s. The other investigated materials reached within 1 s after the scratch a current density of 10^{-3} A/cm^2, so a one order of magnitude higher dissolution current density than for the superaustenitic material.

This result is also very compatible with the polarization tests, which have been performed in 1 bar CO_2 purged solution at a pH close to 3 (Figure 4.6, Table 4.9). Only the 20Cr24Ni6Mo superaustenite shows under these conditions a full passive behavior. All other materials result in pitting at rather low potentials (E_{rep}) and passive current densities are somewhat higher than for the superaustenite.

4.4 Chemical depassivation tests

Five chemical depassivation tests were made. Two tests examined only 13Cr steel while changing the pH from 5 to 3 and back to 5 at 30 °C and 80 °C, two examined 13Cr6Ni2Mo, 15Cr6Ni2Mo and 17Cr4Ni2Mo steels while changing the pH from 4 to 2 and back to 4 at 30 °C and 80 °C and one test examined 17Cr12Ni2Mo, 22Cr5Ni3Mo and 20Cr24Ni6Mo steels while changing the pH from 2 to 0 and back to 2 at 30 °C. The potential diagrams obtained are presented for each steel and solution temperature individually for better readability. Potential decrease indicates chemical depassivation while the potential increase indicates repassivation. Additionally the sample surfaces were observed for H_2 gas formation, indicating an active state.

The potential measurements obtained from 13Cr steel in 5 % NaCl solution at 30 °C are shown in Figure 4.19, along with the pH measurement inside the cell (potential on left y-axis, pH on right y-axis). During the measurement the dissolved oxygen was measured inside the largest solution container and was kept between 8.5 and 15 ppb while the temperature inside the flow cell varied between 29.4 °C and 30.4 °C. The potential decreased upon reaching pH 3.25 and started to increase once pH 3.5 was reached approximately 36 hours later. The depassivation and repassivation pH gained from observing potential corresponds to H_2 gas formation.

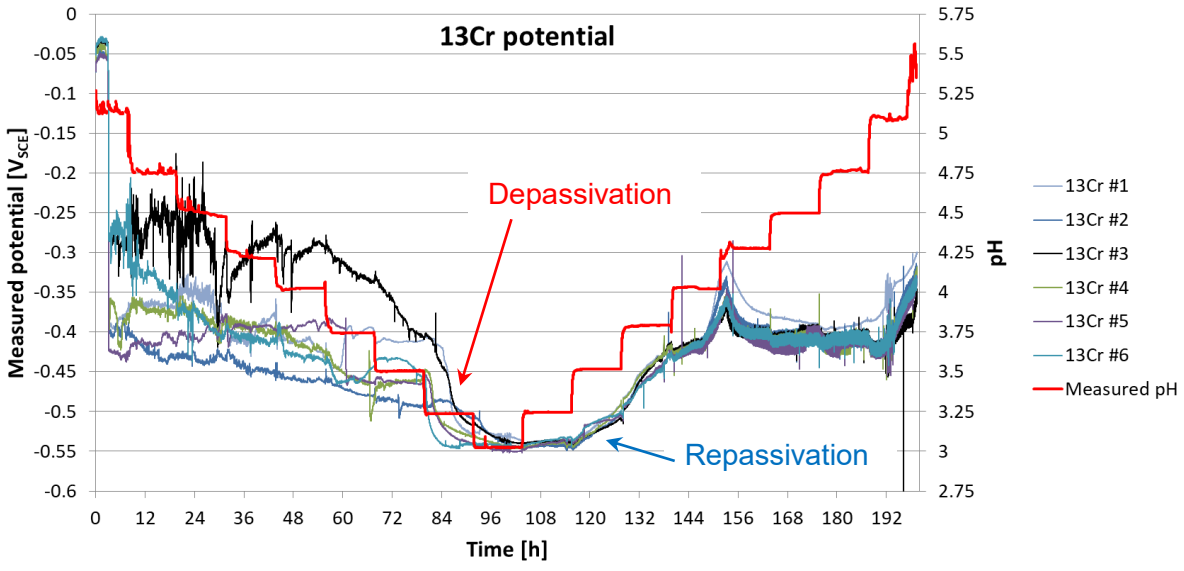

Figure 4.19: Measured potential during exposure of 13Cr steel to 5 % NaCl solution at 30 °C, Ar purged

The second chemical depassivation test was performed on samples from 13Cr6Ni2Mo, 15Cr6Ni2Mo and 17Cr4Ni2Mo steels. To avoid damaging the dissolved oxygen sensor,

dissolved oxygen was measured at the beginning and end of the experiment inside the large solution container, where the measured values fluctuated between 17.8 and 43.8 ppb. Throughout the experiment the temperature was maintained between 29.9 °C and 30.5 °C, with an exception between times t_{PO} = 105.8 h (time when power outage occurred) and t_{TS} = 109.6 h (time when temperature stabilized at 30 °C). In between T_{PO} and T_{TS}, the temperature decreased to 27.1 °C at time t = 107.6 h and increased to 31.7 °C at time t = 108.2 h before decreasing again to the desired values.

Figure 4.20 shows the potential measurements obtained from testing the 13Cr6Ni2Mo steel in 5 % NaCl solution at 30 °C. The potential decreased between pH 1.75 and pH 1.5 indicating depassivation. However there was no clear potential increase indicating repassivation. The H_2 gas formation has indicated a more precise depassivation pH of 1.5 and repassivation at pH of 2.25.

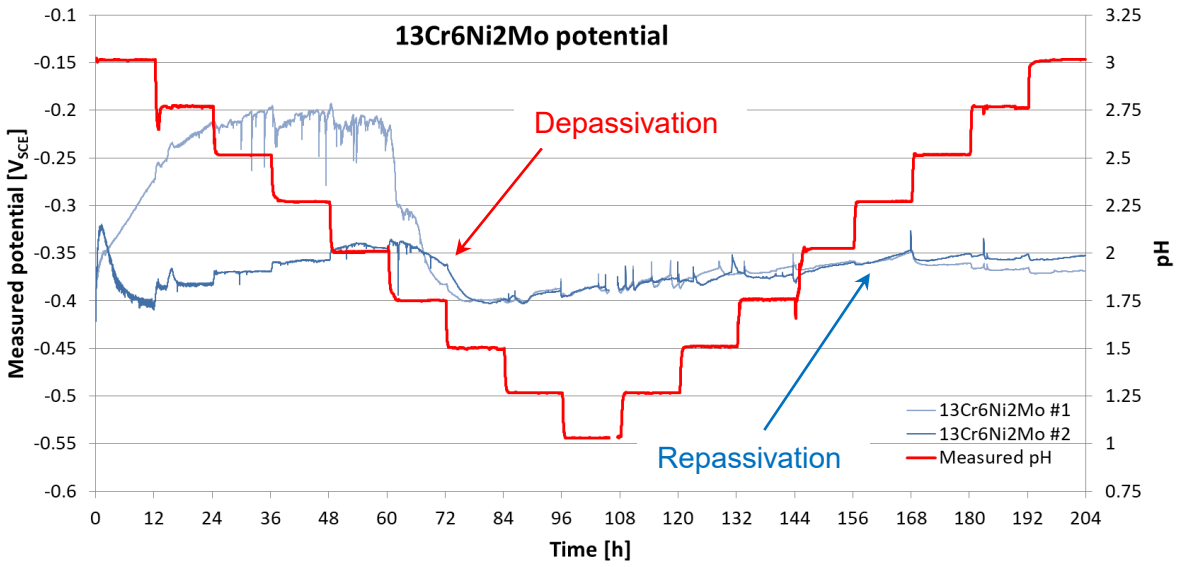

Figure 4.20: Measured potential during exposure of 13Cr6Ni2Mo steel to 5 % NaCl solution at 30 °C, Ar purged

The potential measurement of 15Cr6Ni2Mo steel in 5 % NaCl solution at 30 °C is displayed in Figure 4.21. The potential decrease at pH 1 corresponds to depassivation, while the potential increase at pH 1.75 corresponds to repassivation. The potential increase on sample #1 at pH 1.5 is an artefact, which appeared due to the formation of a large gas bubble covering most of the surface of the sample. The gas bubble was removed, when the pH was adjusted.

The potential measurement of 17Cr4Ni2Mo steel in 5 % NaCl solution at 30 °C is displayed in Figure 4.22. Observing the potential it is possible to see a decrease on sample #1 during the

pH 1 step and an increase at pH 1.5, indicating these are the depassivation and repassivation pH values respectively, while sample #2 has not had a potential decrease indicating depassivation. Observing H_2 gas formation we could confirm the pH values for sample #1, while sample #2 has shown gas formation already at pH 1.25 and the gas stopped forming at pH 1.5.

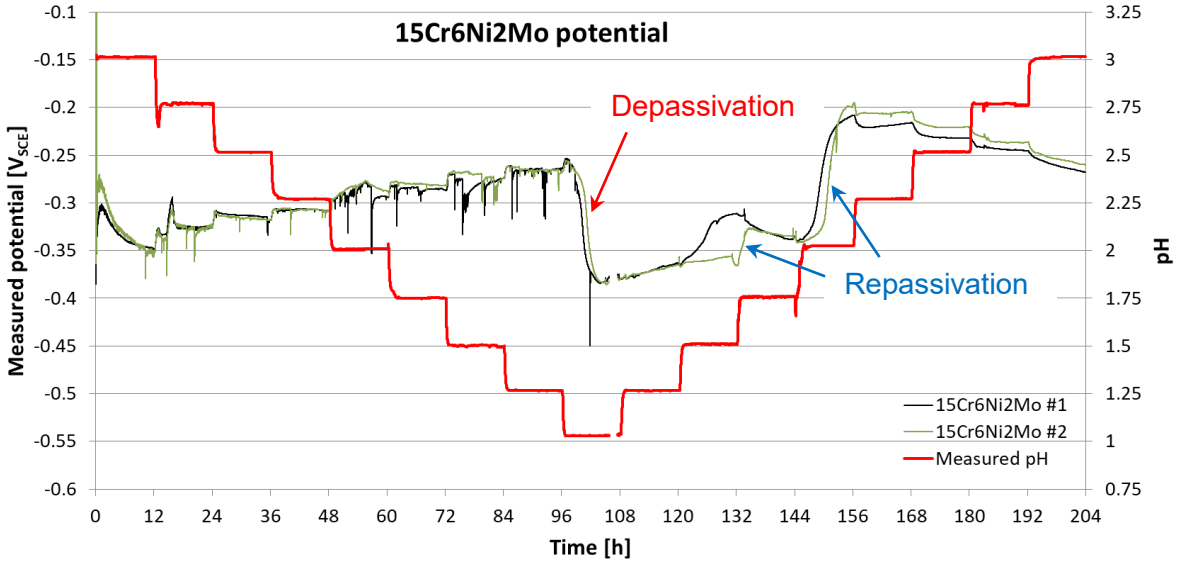

Figure 4.21: Measured potential during exposure of 15Cr6Ni2Mo steel to 5 % NaCl solution at 30 °C, Ar purged

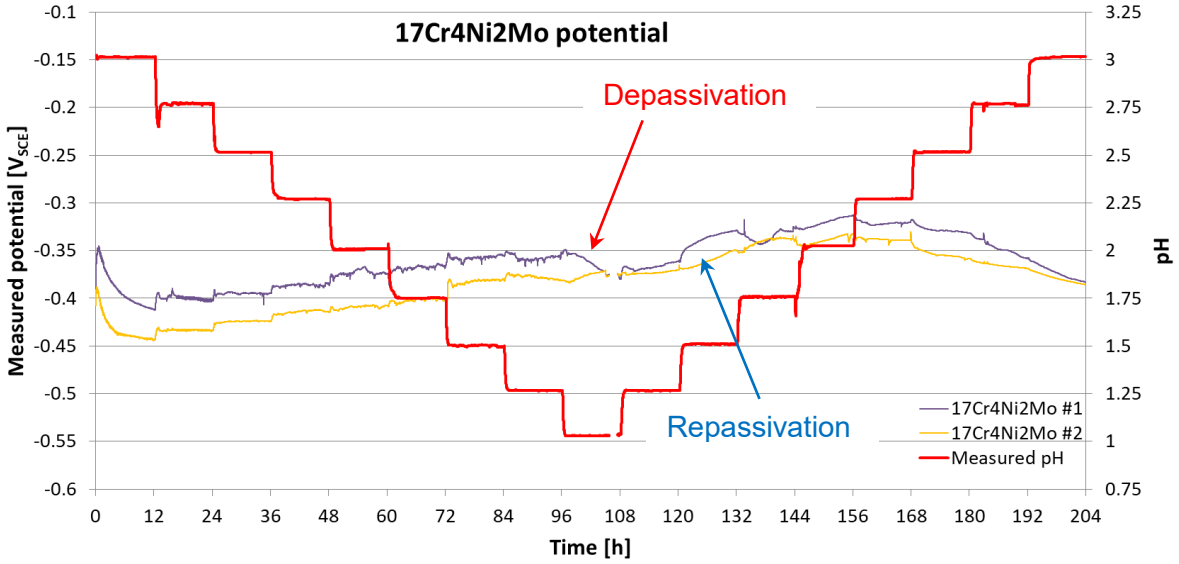

Figure 4.22: Measured potential during exposure of 17Cr4Ni2Mo steel to 5 % NaCl solution at 30 °C, Ar purged

The third experiment at 30 °C was performed on 17Cr12Ni2Mo, 22Cr5Ni3Mo and 20Cr24Ni6Mo steel grades. The pH measurement shows values below pH 1 to be higher than the set value. Thus, samples of the solution were taken during pH 0.75, pH 0.5, pH 0.25 and pH 0 steps and compared to pH 2 buffer solution after dilution of each solution with distilled water (dilution ratio of water to solution was 55.23:1, 30.62:1, 16.88:1 and 9:1 respectively). It was confirmed that the set pH is the actual pH of the solution (± 0.03 pH) and the pH sensor used for measurement is inaccurate below pH 1 with the calibration used (based on pH 7 and pH 4.01 buffers). The temperature inside the cell was maintained between 29.6 °C and 30.3 °C.

Figure 4.23 displays the measured potential on the 17Cr12Ni2Mo steel samples. Sample #1 had a potential decrease indicating depassivation during the pH 0.75 step, while sample #2 had a potential decrease indicating depassivation during the pH 0.5 step. Both samples then followed the same potential behavior until the shift to pH 1.75, while the potential increase at pH 1.5 indicates repassivation. The same depassivation and repassivation pH values were confirmed by H_2 gas formation on sample surfaces.

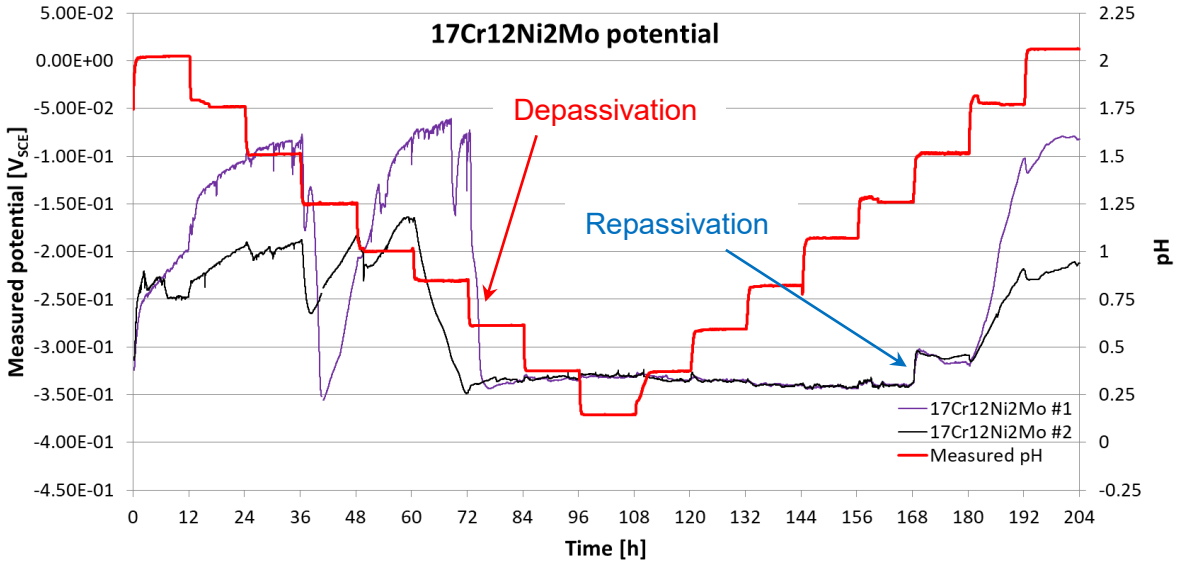

Figure 4.23: Measured potential during exposure of 17Cr12Ni2Mo steel to 5 % NaCl solution at 30 °C, Ar purged

Figure 4.24 displays the measured potential on the 22Cr5Ni3Mo steel samples. All three samples had a potential decrease at pH 0.25 indicating depassivation. Samples #1 and #3 had a potential increase indicating repassivation at pH 0.75 while sample #2 had the potential increase indicating repassivation occured at pH 1. The H_2 gas formation confirms these depassivation and repassivation pH values.

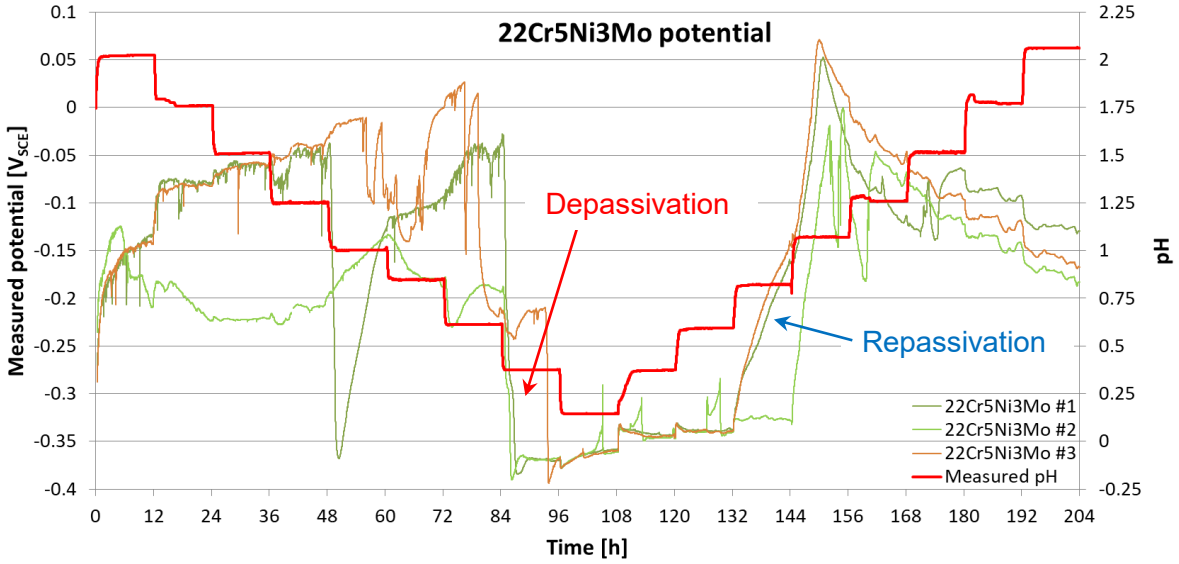

Figure 4.24: Measured potential during exposure of 22Cr5Ni3Mo steel to 5 % NaCl solution at 30 °C, Ar purged

Figure 4.25 displays the potential measurement on a 20Cr24Ni6Mo steel sample in 5 % NaCl 30 °C solution, which indicates depassivation at pH 0 and repassivation at pH 0.75. These values were confirmed by observing H_2 gas formation.

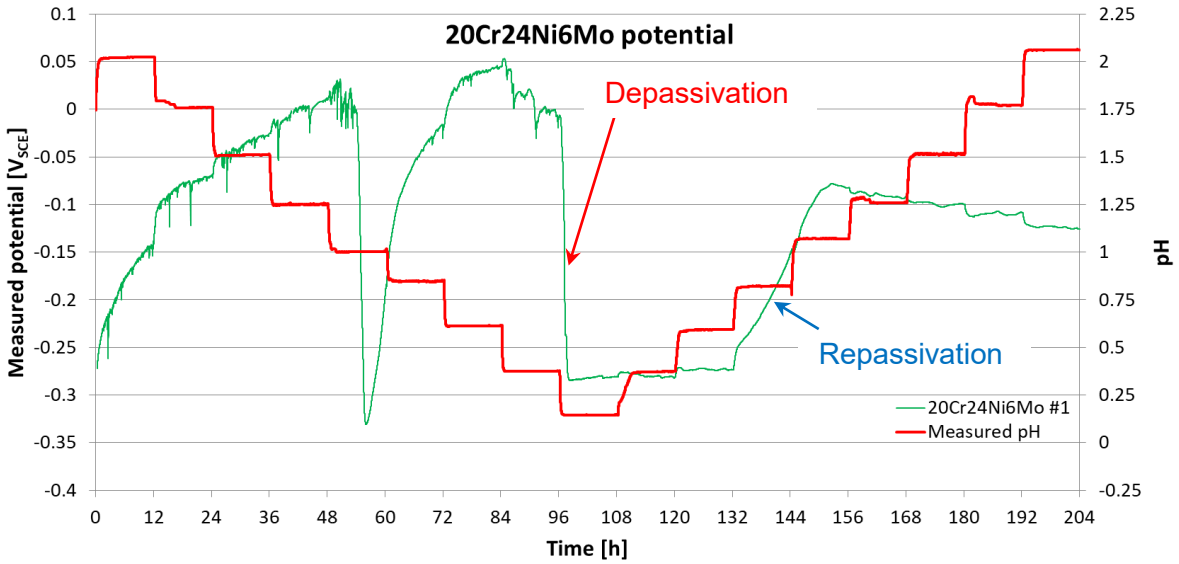

Figure 4.25: Measured potential during exposure of 20Cr24Ni6Mo steel to 5 % NaCl solution at 30 °C, Ar purged

The temperature of the following experiments was set to 80 °C, to see the temperature effect. To avoid damaging equipment, no tests were performed on the austenites and duplex steels at this elevated temperature.

The fourth chemical depassivation test was performed on 13Cr steel samples in 5 % NaCl solution at 80 °C. The dissolved oxygen was maintained between 29.6 and 58.7 ppb in the large solution container and the temperature was kept between 74.4 °C and 80.4 °C. Initially the pH was too high however this has not affected depassivation and repassivation pH values.

The potential measurements of the 13Cr samples are shown in Figure 4.26. Determining the depassivation and repassivation pH of the steel was quite difficult from the potential. Upon examining H_2 gas formation depassivation could be determined at pH 3.0 and repassivation at pH 3.25 – values very similar to the ones that were obtained in 30 °C tests (pH 3.25 and 3.5 respectively) .

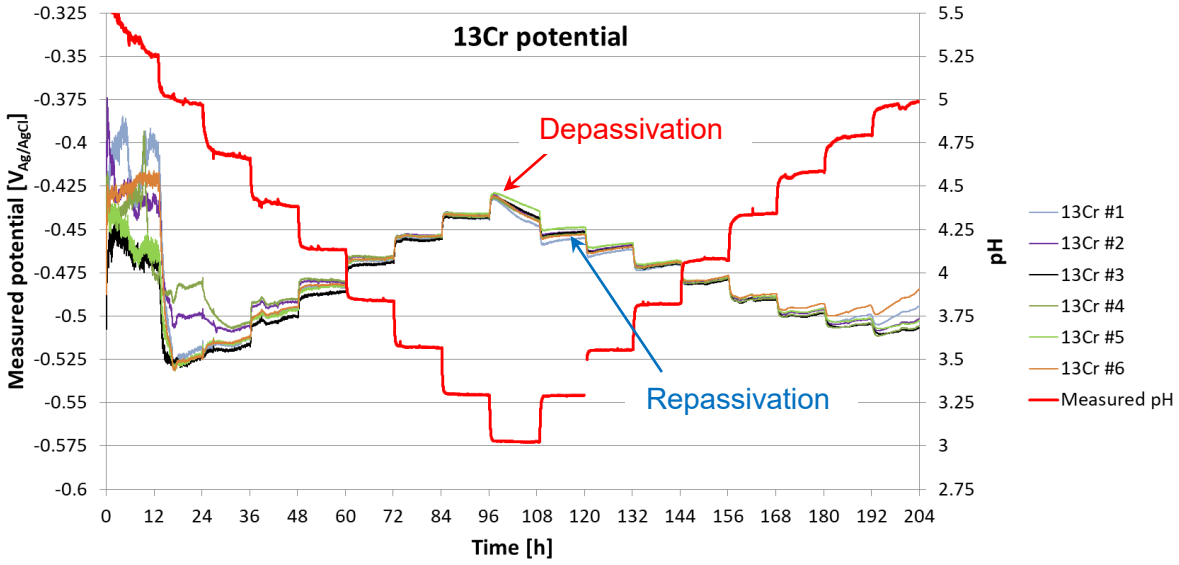

Figure 4.26: Measured potential during exposure of 13Cr steel to 5 % NaCl solution at 80 °C, Ar purged

The fifth and last chemical depassivation test was performed on 13Cr6Ni2Mo, 15Cr6Ni2Mo and 17Cr4Ni2Mo steel grades in 5 % NaCl solution at 80 °C. The temperature was maintained between 75.4 °C and 80.9 °C. The dissolved oxygen content was not measured.

The potential measurements of 13Cr6Ni2Mo steel samples in 5 % NaCl solution at 80 °C are shown in Figure 4.27. The potential decreased at pH 1.5 indicating depassivation, while repassivation pH could not be determined from the potential measurement. Upon observing H_2 gas formation the depassivation pH was confirmed to be 1.5 and the repassivation pH was determined to be 2.5.

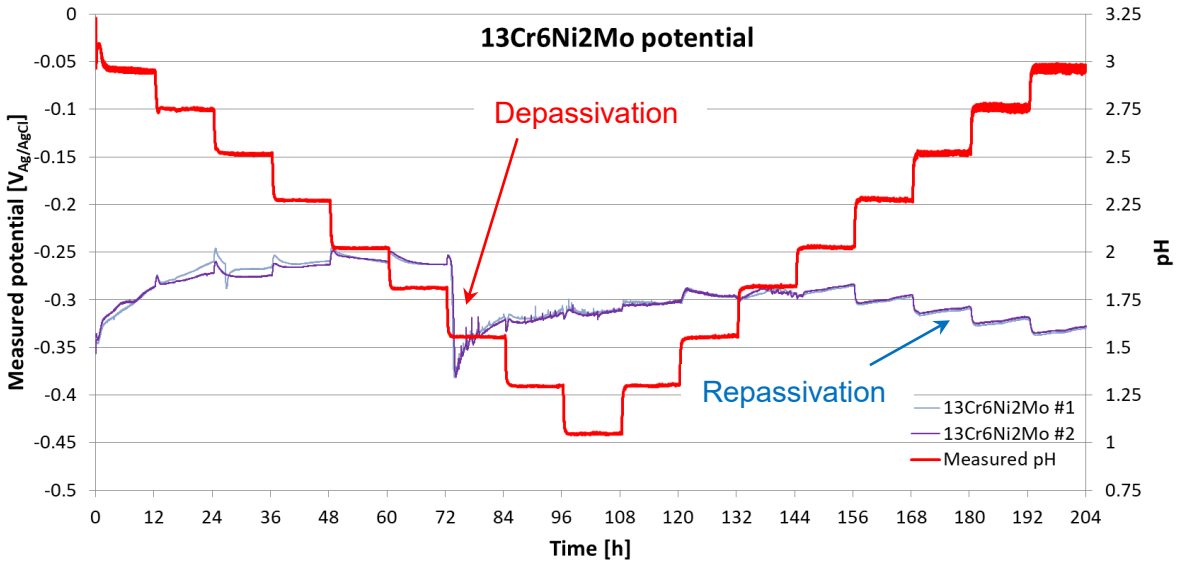

Figure 4.27: Measured potential during exposure of 13Cr6Ni2Mo steel to 5 % NaCl solution at 80 °C, Ar purged

The potential measurement of 15Cr6Ni2Mo steel in 5 % NaCl solution at 80 °C is displayed in Figure 4.28. The potential decrease at pH 1 corresponds to depassivation, while the potential increased at pH 1.75 corresponds to repassivation – values identical to the ones obtained during the 30 °C test. The formation of H_2 gas confirmed the depassivation and repassivation pH values.

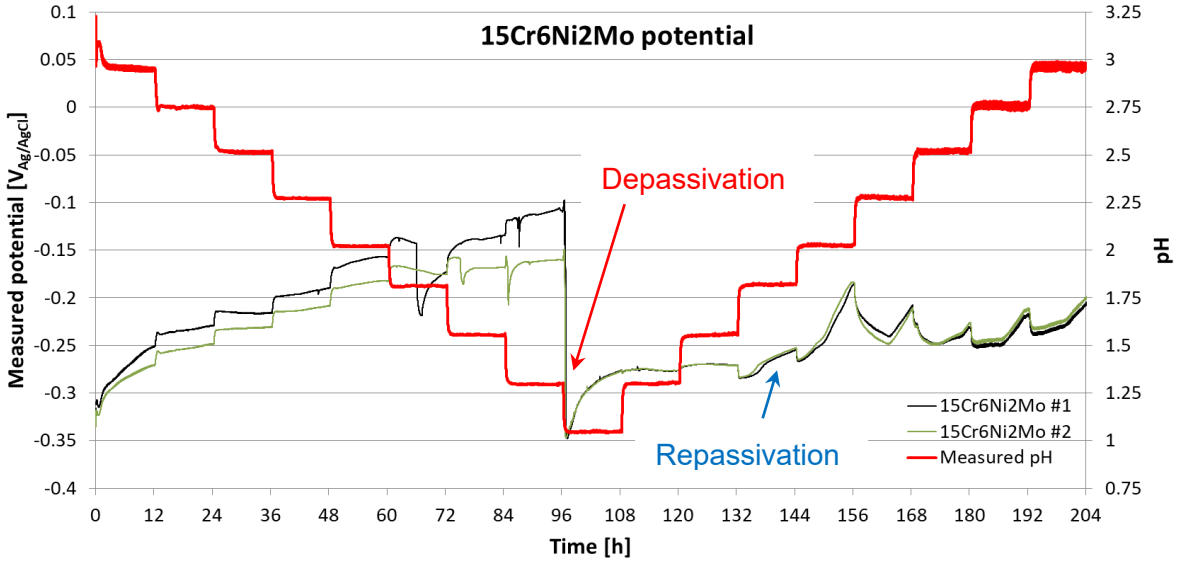

Figure 4.28: Measured potential during exposure of 15Cr6Ni2Mo steel to 5 % NaCl solution at 80 °C, Ar purged

Figure 4.29 shows the potential measurements of 17Cr4Ni2Mo steel samples in 5 % NaCl solution at 80 °C. Sample #1 shows a potential decrease at pH 1 indicating depassivation and a potential increase at pH 1.25 indicates repassivation, which corresponds to H_2 gas formation. Sample #2 did not depassivate during the test and thus it did not yield any usable data. Obviously the steel is close to its depassivation limit at or slightly below pH 1.

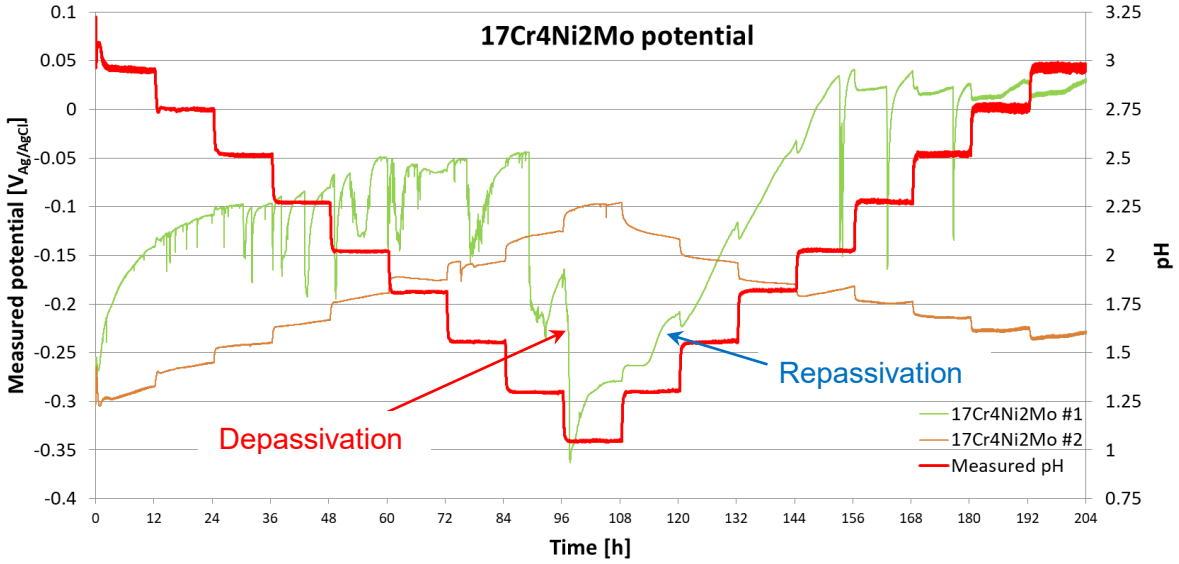

Figure 4.29: Measured potential during exposure of 17Cr4Ni2Mo steel to 5 % NaCl solution at 80 °C, Ar purged

All depassivation and repassivation values obtained from experiments have been compiled into Tables 4.11 and 4.12 (values obtained from tests performed in 30 °C and 80 °C solutions respectively).

The data show that both tests, the immersion test and the chemical depassivation test result in highly consistent data and the three groups of materials 13Cr on the one side, the heat treatable martensitic and bainitic CrNiMo steels on the other side and the higher alloyed austenites and duplex steels on the third side show a repassivation pH that differs by ~ 1 pH from the next higher alloyed group. All materials under all conditions show a difference between depassivation and repassivation pH. The difference ΔpH was for all measurements between 0.25 and 1 pH, mainly between 0.5 and 0.75 pH.

Table 4.11: Values obtained from immersion tests and chemical depassivation tests performed at 30 °C – highest pH where uniform corrosion occurred during immersion test ($pH_{uniform}$), depassivation pH (pH_{depass}), repassivation pH (pH_{repass}) and difference between depassivation and repassivation pH (ΔpH)

Steel	**$pH_{uniform}$**	**pH_{depass}**	**pH_{repass}**	**ΔpH**
13Cr	3	3.25	3.5	0.25
13Cr6Ni2Mo	2	1.5	2.25	0.75
15Cr6Ni2Mo	1	1	1.75	0.75
17Cr4Ni2Mo	1	1.25/1	1.5	0.25/0.5
17Cr12Ni2Mo	0	0.75/0.5	1.5	0.75/1
22Cr5Ni3Mo	0	0.25	0.75/1	0.5/0.75
20Cr24Ni6Mo	0	0	0.75	0.75

Table 4.12: Values obtained from immersion tests and chemical depassivation tests performed at 80 °C – highest pH where uniform corrosion occurred during immersion test ($pH_{uniform}$), depassivation pH (pH_{depass}), repassivation pH (pH_{repass}) and difference between depassivation and repassivation pH (ΔpH)

Steel	**$pH_{uniform}$**	**pH_{depass}**	**pH_{repass}**	**ΔpH**
13Cr	3	3	3.25	0.25
13Cr6Ni2Mo	2	1.5	2.5	1
15Cr6Ni2Mo	1	1	1.75	0.75
17Cr4Ni2Mo	1	1/<1	1.25/NA	0.25/NA

4.5 Passive layer chemistry

Although the investigated specimens have been already described in Chapter 3.3 they are summarized once more in Table 4.13 for XPS and ToF-SIMS analysis. The XPS investigations were performed on the surface of each sample and in addition after removing of approximately 2 nm of material by sputtering (aim: to investigate the chemical composition of the passive layer at the surface and near the passive film/metal interface). The different pH values were chosen, to investigate passive layers at their very edge of stability.

Figure 4.30 shows the measured atomic percentage of oxygen, chromium, iron, nickel and molybdenum in all 16 cases. Comparing all of the surface XPS measurements one can see a similar amount of oxygen found in all 8 samples.

Table 4.13: Specimens investigated by XPS and ToF-SIMS after passivation for 24 h

Passivating Medium	Material		
	13Cr	17Cr4Ni2Mo	17Cr12Ni2Mo
Air, RT	X	X	X
5 % NaCl, pH 5, 30 °C	X	X	X
5 % NaCl, pH 3, 30 °C		X	
5 % NaCl, pH 1, 30 °C			X

XPS was done on surface and in 2 nm depth
ToF-SIMS was done as depth profile measurement

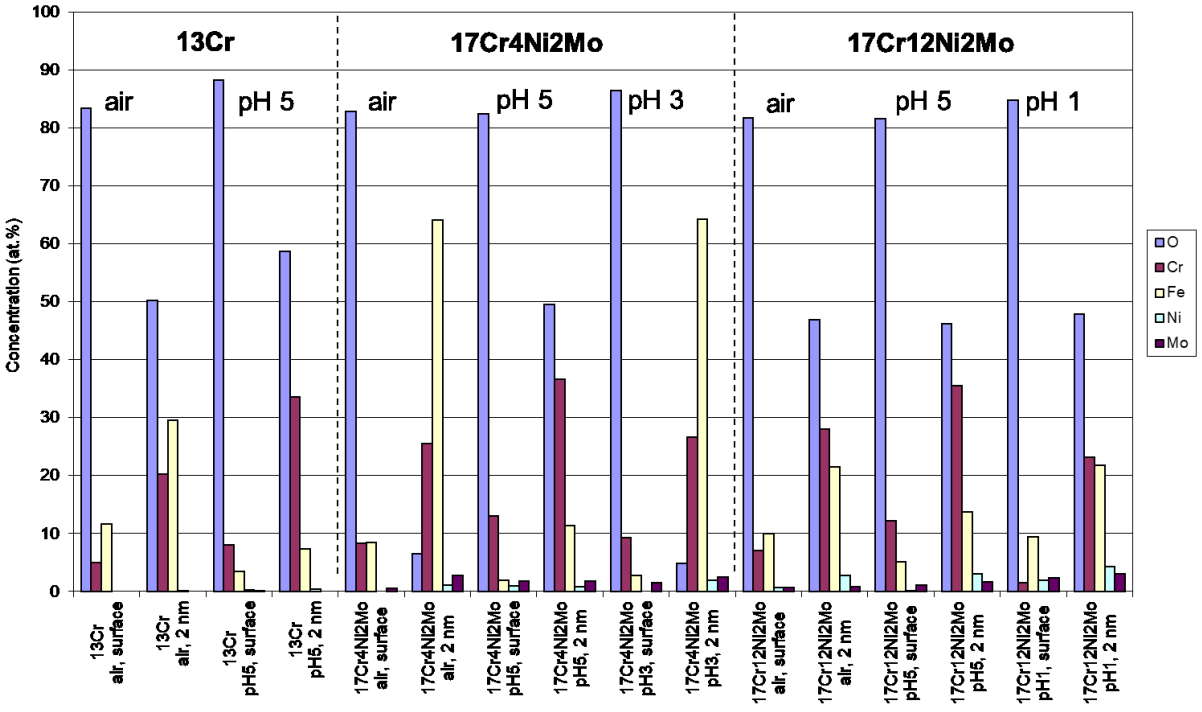

Figure 4.30: XPS chemical composition analysis on sample surface and after sputtering approximately 2 nm of material on 8 investigated samples after passivation in air and in 5 %NaCl at given pH and 30 °C, all samples exposed for 24 h

Of these 8 measurements one can see that all three air passivated samples contain more iron than chromium (or the same amount in case of the 17Cr4Ni2Mo sample) and nearly no nickel or molybdenum.

The three samples passivated in pH 5 solution, however show more chromium than iron, indicating some of the iron has been dissolved from the surface if compared to air passivated samples. The same is true for the 17Cr4Ni2Mo sample passivated in pH 3 solution, while the 17Cr12Ni2Mo sample passivated in pH 1 solution shows, that the surface contains much more iron than chromium, as well as an increased amount of nickel and molybdenum.

When comparing the measurements after sputtering to remove approximately 2 nm of material, one can see that the 17Cr4Ni2Mo sample passivated in air and the 17Cr4Ni2Mo sample passivated in pH 3 solution have a very small atomic percentage of oxygen. This indicates these two measurements were performed on the actual metal and not the passive layer, meaning they should be disregarded. All others show close to 50 at.-% oxygen, indicating the measurements were still made in the oxide layer but close to the passive film/metal interface, which was the desired outcome. Of the 6 remaining measurements, 2 were passivated in air, 3 were passivated in pH 5 solution and 1 was passivated in pH 1 solution. Comparing the results from the samples passivated in pH 5 solution a large amount of chromium is found in comparison to iron. Naturally, molybdenum and nickel are only found in 17Cr4Ni2Mo and 17Cr12Ni2Mo samples and the nickel concentration is higher in the case of 17Cr12Ni2Mo – this is in accordance to the steel chemical compositions. The air passivated 13Cr sample shows a large amount of iron in comparison to chromium, similar to the ratio between the two found at the surface of the sample, while the air passivated 17Cr12Ni2Mo shows a higher amount of chromium in comparison to the iron concentration, as well as some nickel and molybdenum. Finally, the 17Cr12Ni2Mo sample passivated in pH 1 solution contains a similar amount of iron and chromium (a bit higher in iron) and the highest amount of nickel and molybdenum of all 6 samples investigated at the passive film/metal interface.

In general the results of the XPS analysis show a similar passive layer found on all air passivated samples. There is a passive layer consisting of chromium and iron oxides/hydroxides at the surface. In 2 nm depth the Cr/Fe ratio increases to a certain extent and the O content decreased indicating proximity to the oxide/metal interface or being partially already in the metal. After immersion in pH 5 and pH 3 solution, large portions of Fe have been dissolved from the surface. The passive layer formed in pH 1 solution is different from the ones formed in pH 5 and pH 3 solution, as the chromium content is depleted across it, particularly at the surface.

The ToF-SIMS analyses performed on the 8 samples have provided depth profiles of several different anions. The diagrams presented have had the time as x-axis and this was changed into a depth profile x-axis by multiplying the measurement time with the sputtering rate h [nm] = 0.020 [nm/s] · t [s]. To determine the thickness of the passive layers a sum of FeO^-, CrO^-, MoO^{3-}, MoO^{2-}, NiO^-, OH^- and O^{2-} anion counts was examined. The point, where the sum of all the above mentioned anion counts was reduced to 50 % of their maximum value, was taken to determine the location of the interface between the passive film and the underlying metal and the passive layer thickness as such. The thicknesses are presented in Table 4.12.

Table 4.12: Thickness of passive layers after exposure in air and 5 % NaCl at various pH levels by ToF-SIMS profiles.

Exposure medium	Thickness of passive layer of material [nm]		
	13Cr	17Cr4Ni2Mo	17Cr12Ni2Mo
Air, RT	2.13	2.16	2.10
5 % NaCl, pH 5, 30 °C	6.68	2.32	2.63
5 % NaCl, pH 3, 30 °C		2.07	
5 % NaCl, pH 1, 30 °C			3.32

Thickness of passive films is approximately 2 nm in the air passive state. There is a tendency of thickness increase, when layers are grown in a medium. Especially aggressive media result in thicker films (pH 5 solution for 13Cr, pH 1 solution for 17Cr12Ni2Mo).

Figures 4.31, 4.32 and 4.33 show the ToF-SIMS depth profiles obtained from 13Cr, 17Cr4Ni2Mo and 17Cr12Ni2Mo samples exposed to air at room temperature.

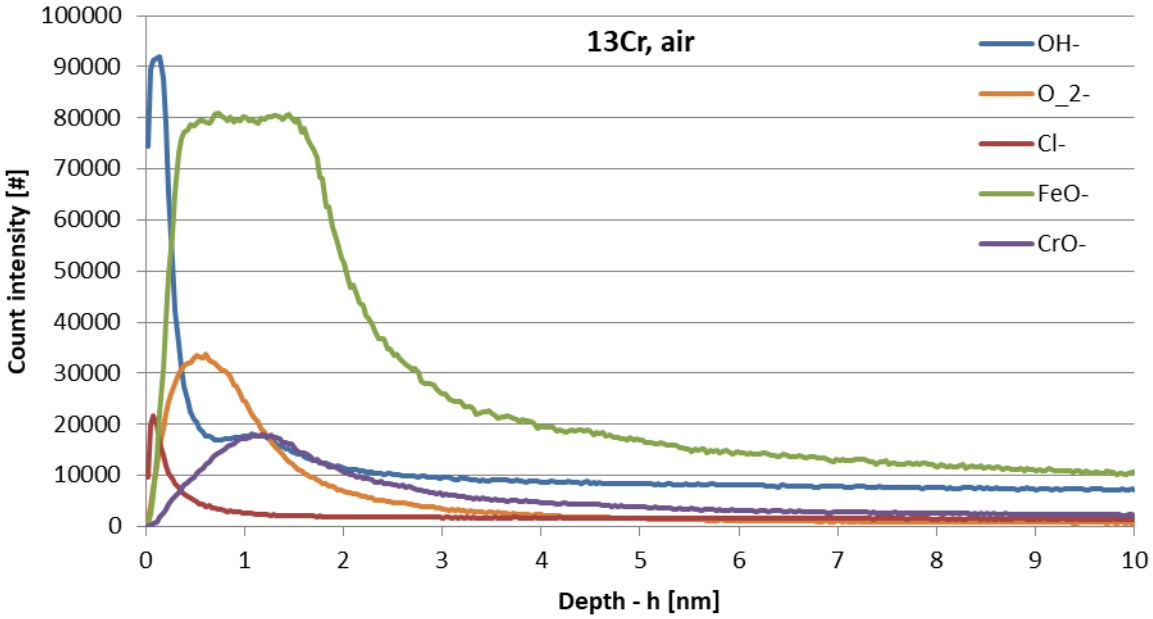

Figure 4.31: SIMS depth profile on 13Cr steel after 24 h exposure to air, room temperature

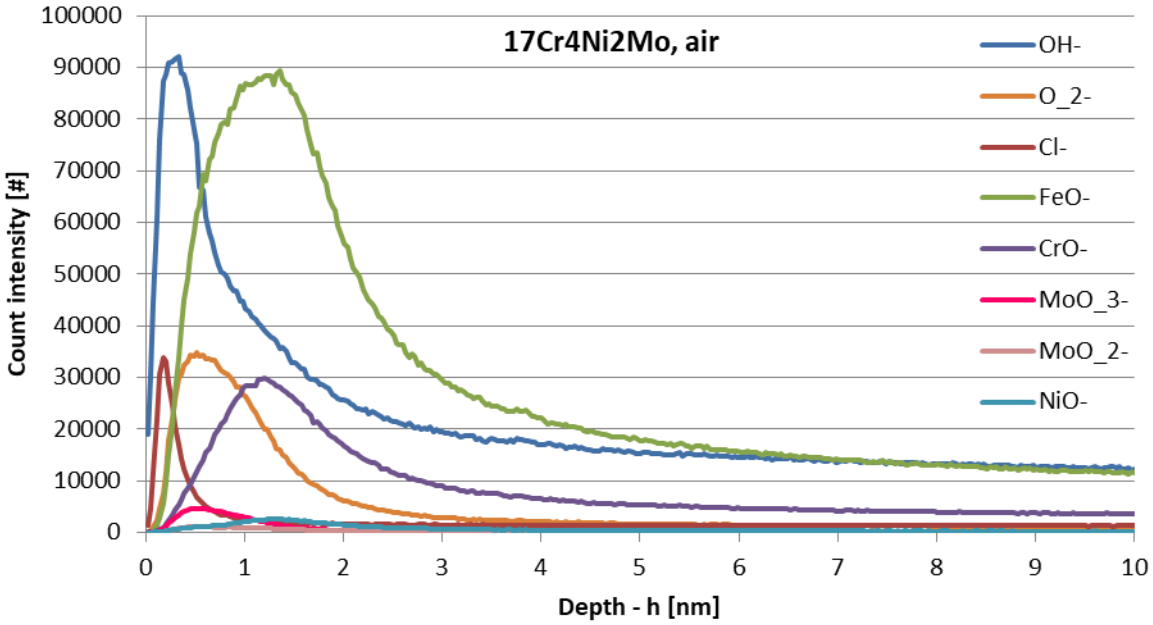

Figure 4.32: SIMS depth profile on 17Cr4Ni2Mo steel after 24 h exposure to air, room temperature

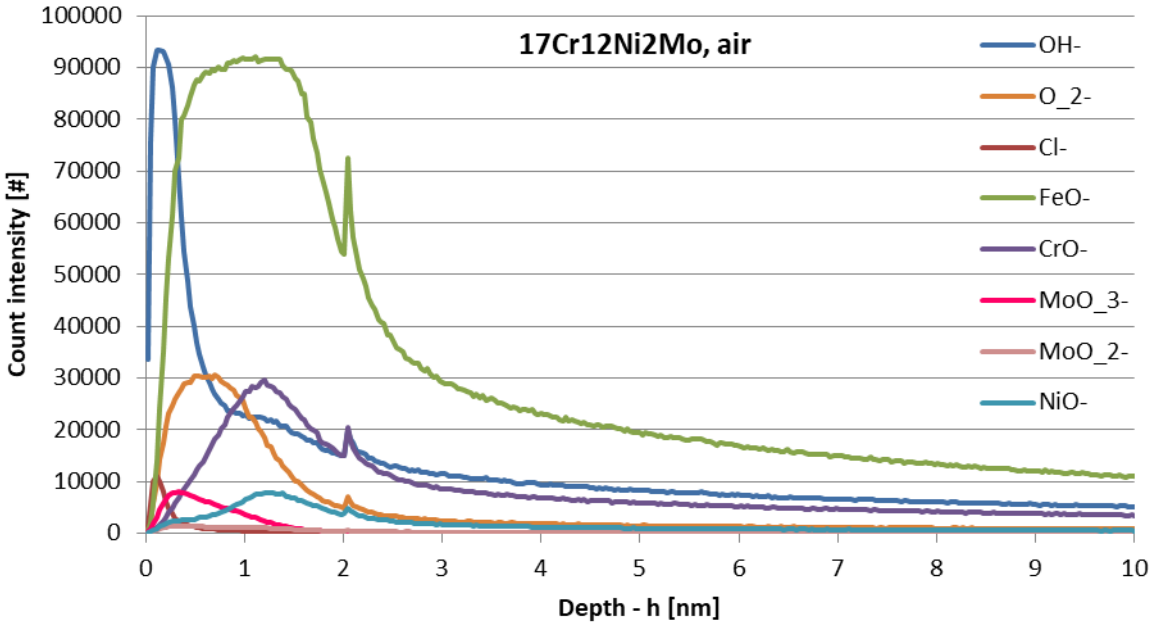

Figure 4.33: SIMS depth profile on 17Cr12Ni2Mo steel after 24 h exposure to air, room temperature

A large intensity of FeO^- was found in these cases across the entire passive layer thickness. CrO^- ions were depleted at the film surface and somewhat enriched deeper in the film. MoO^{3-} and NiO^- were found at the film surface and film/metal interface respectively in the cases of 17Cr4Ni2Mo and 17Cr12Ni2Mo. Small amounts of Cl^- were found near the surface, which was attributed to contamination during sample handling.

Figures 4.34, 4.35 and 4.36 show the ToF-SIMS depth profiles obtained from 13Cr, 17Cr4Ni2Mo and 17Cr12Ni2Mo samples exposed to pH 5 solutions. Compared to air passivated samples, there is a strong depletion of FeO^- - the surface was particularly depleted of this anion however a decrease in the count intensity is also noticeable deeper in the film. CrO^- ion count intensity is increased – approximately 50 % more ions are found across the depth of the film in comparison to films formed in air. A large amount of Cl^- ions are found at the surface of the passive films, which was to be expected considering the large chloride content of the medium used for exposure.

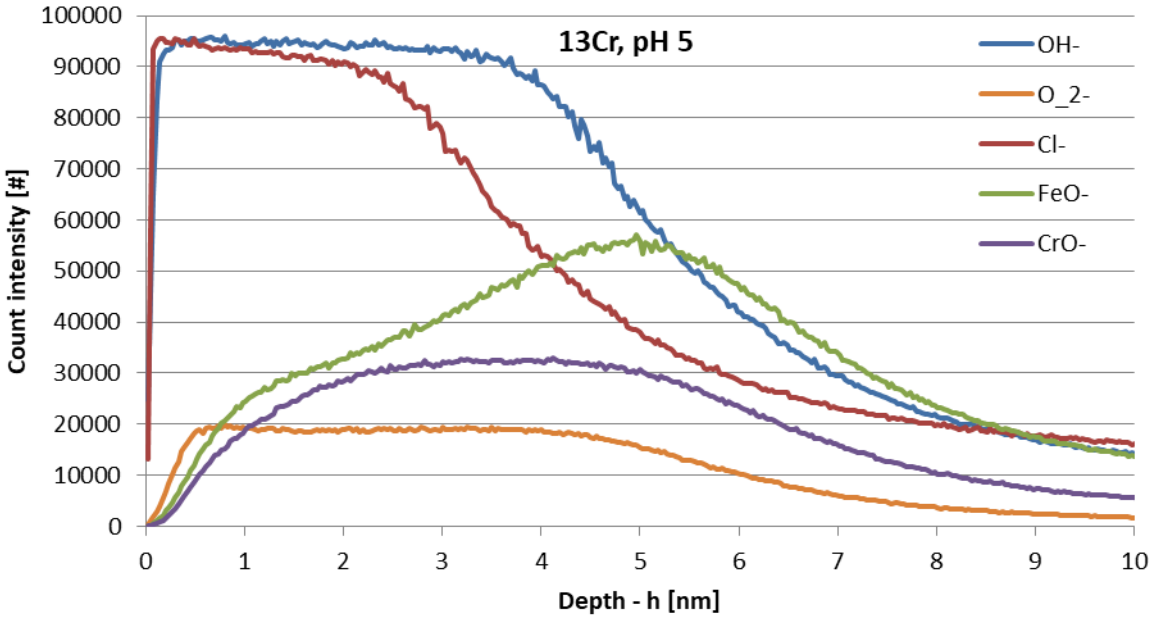

Figure 4.34: SIMS depth profile on 13Cr steel after 24 h exposure to 5 % NaCl, at pH 5 solution, 30 °C

Observing 17Cr4Ni2Mo and 17Cr12Ni2Mo samples, the NiO^- intensity seems mostly unaffected while the MoO^{3-} and MoO^{2-} counts are markedly higher after exposure to pH 5 solutions, particularly in the case of 17Cr12Ni2Mo. Again, nickel and molybdenum oxides were found in the film/metal interface and near the surface respectively.

Figure 4.37 shows the depth profile gained from the 17Cr4Ni2Mo sample exposed to pH 3 solution. Comparing this to Figure 4.35 one can see very similar depth profiles from both 17Cr4Ni2Mo samples exposed to pH 5 and pH 3 solutions.

The main differences between pH 3 and pH 5 immersion are a somewhat reduced film thickness and an increase of Cl^- ion depth penetration in case of exposure to pH 3 solution. The depth profile of the 17Cr12Ni2Mo sample exposed to pH 1 is presented in Figure 4.38. In this case one can see a large penetration of Cl^- ions into the passive film and a strong enrichment of MoO^{3-} and MoO^{2-} ions in the layer. Compared to the exposure of the same material in pH 5 solution, a depletion of CrO^- and an enrichment of FeO^- along with an increase of passive layer thickness is obtained. NiO^- count intensity is somewhat reduced however the sum of the ion counts is greater due to a thicker passive film.

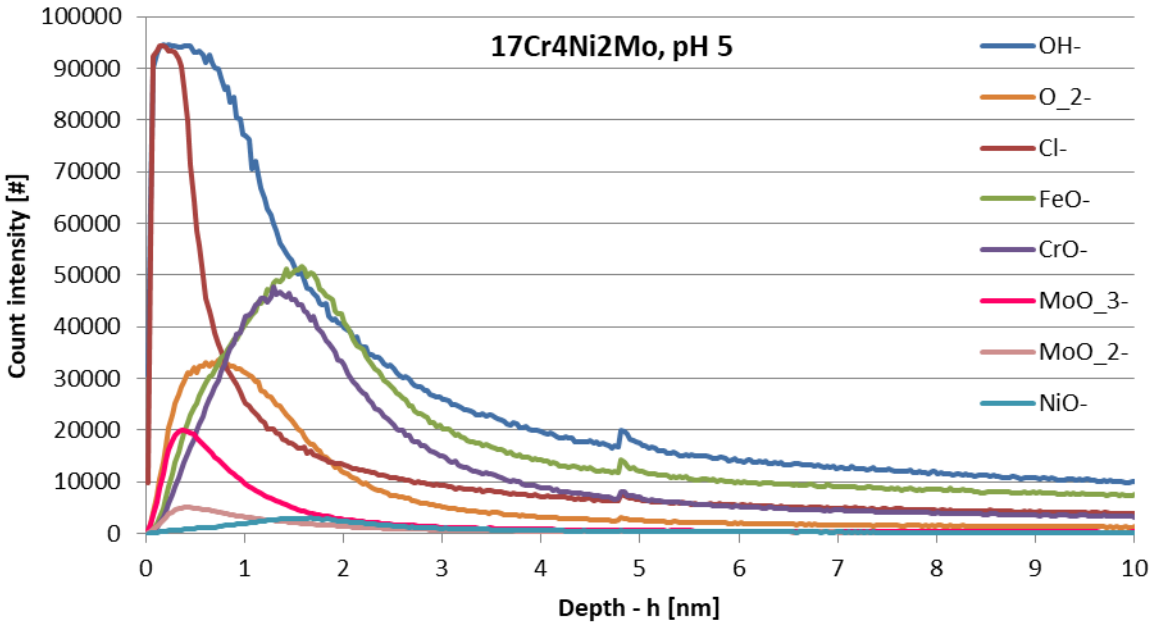

Figure 4.35: SIMS depth profile on 17Cr4Ni2Mo steel after 24 h exposure to 5 % NaCl, at pH 5 solution, 30 °C

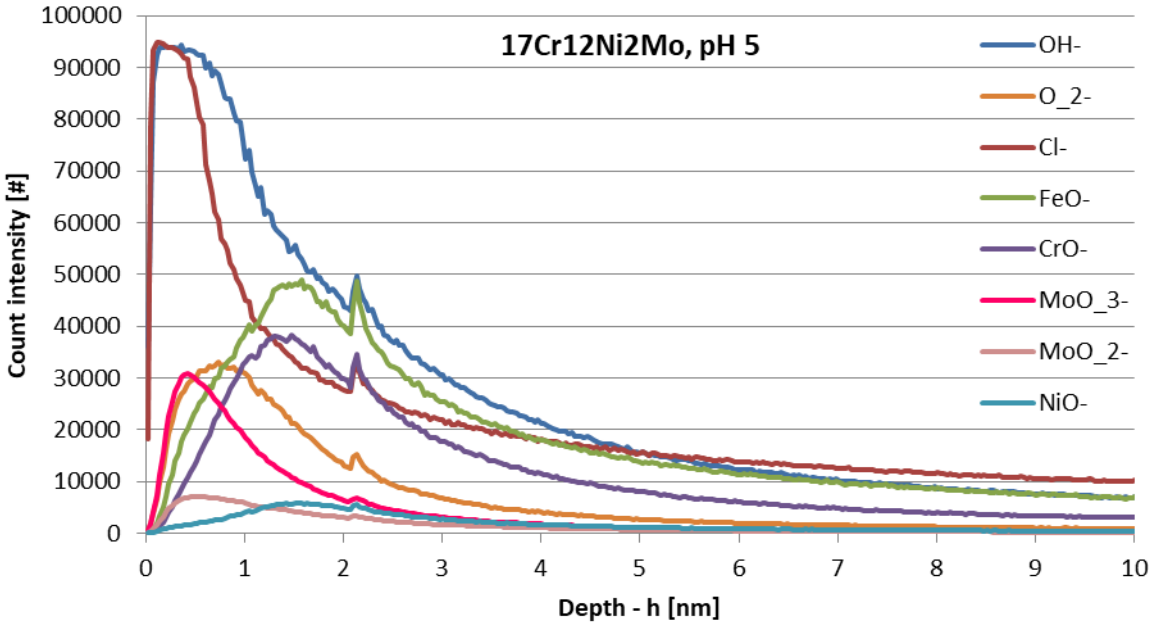

Figure 4.36: SIMS depth profile on 17Cr12Ni2Mo steel after 24 h exposure to 5 % NaCl, at pH 5 solution, 30 °C

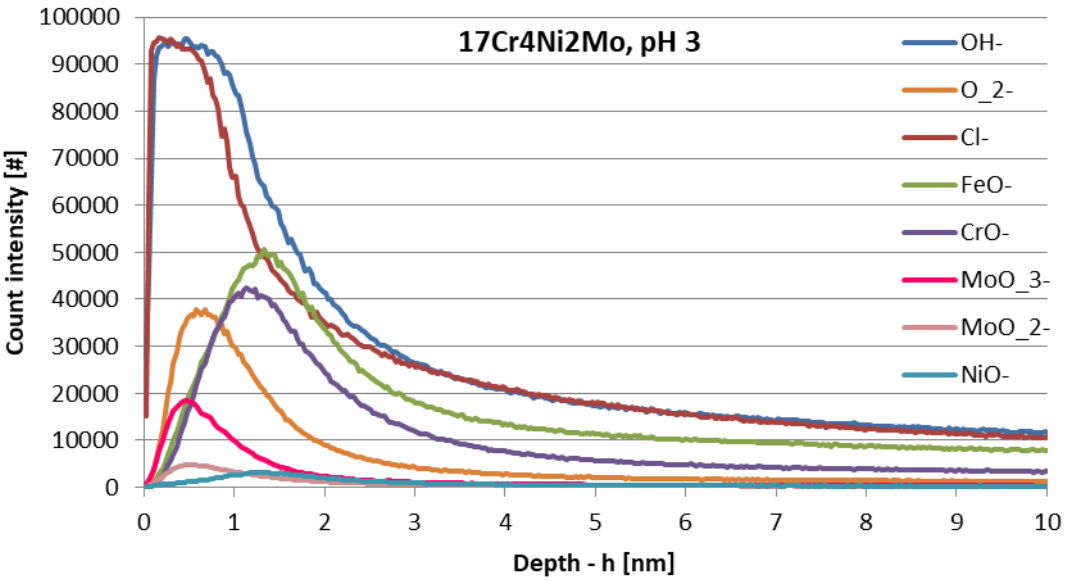

Figure 4.37: SIMS depth profile on 17Cr4Ni2Mo steel after 24 h exposure to 5 % NaCl, at pH 3 solution, 30 °C

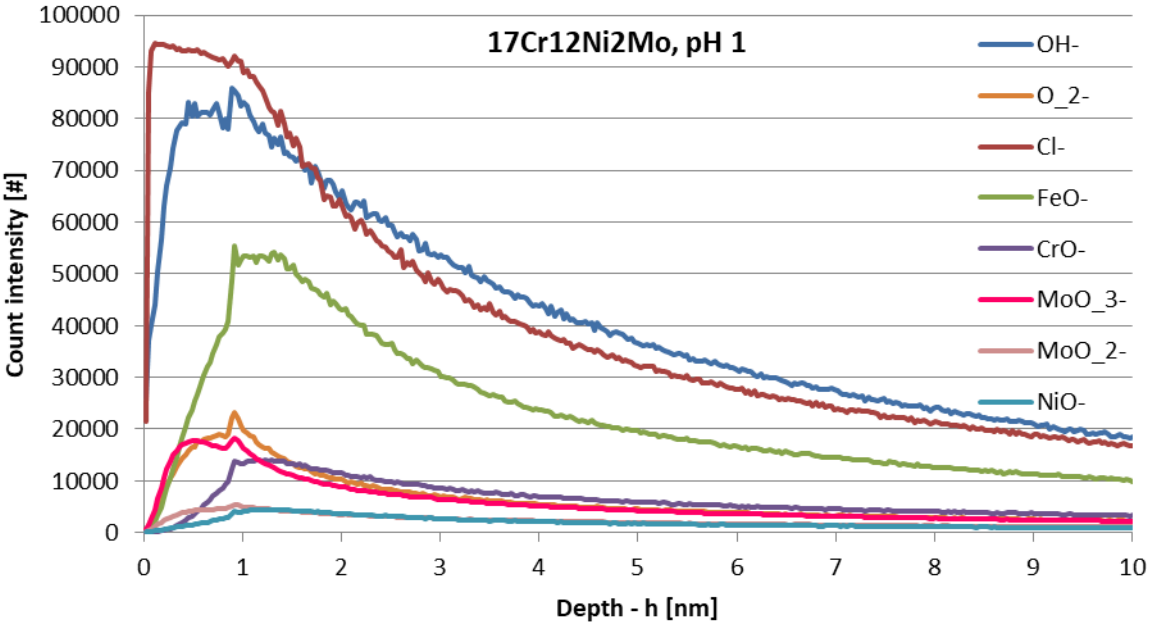

Figure 4.38: SIMS depth profile on 17Cr12Ni2Mo steel after 24 h exposure to 5 % NaCl, at pH 1 solution, 30 °C

Table 4.15 contains the integrals of FeO^-, CrO^-, MoO^{3-}, MoO^{2-} and NiO^- ions during the 1000 s testing time for all samples (approximately 20 nm sputtering depth). This table does not represent the exact amount of each element found in the passive layer but only gives a rough estimate of the chemical composition.

Table 4.15: Integral of ion counts within 1000s for all investigated samples in SIMS

Sample	FeO^-	CrO^-	MoO^{3-}	MoO^{2-}	NiO^-
13Cr air	11828884	2522647	-	-	-
13Cr pH 5	13535824	7530293	-	-	-
17Cr4Ni2Mo air	12154599	3666246	198336	112280	286398
17Cr4Ni2Mo pH 5	7440050	4805128	860952	347491	306346
17Cr4Ni2Mo pH 3	7189472	4260604	794091	324758	311774
17Cr12Ni2Mo air	12403587	3481836	261550	140350	705754
17Cr12Ni2Mo pH 5	7378571	4530550	1491645	570873	673814
17Cr12Ni2Mo pH 1	9352271	2718894	2297818	917922	791677

Figures 4.39, 4.40, 4.41 and 4.42 show the depth profiles of ratios between CrO^- and FeO^- across the investigated samples. Figures 4.39 and 4.40 show these profiles after exposure to air and pH 5 solutions respectively, while Figures 4.41 and 4.42 show the ratio profiles for 17Cr4Ni2Mo and 17Cr12Ni2Mo samples after exposure to different pH solutions respectively.

Comparing Figures 4.39 and 4.40 shows a large enrichment of chromium compared to iron in the passive layer after exposure to pH 5 solutions. This is in complete agreement with XPS results. Apart from the 13Cr sample having a much thicker passive layer in pH 5 solution compared to other steels, the ratio profiles seem very similar and in line with the steel chemical compositions.

Figure 4.41 indicates that the passive layer formed in pH 3 solution is very similar to the passive layer formed in pH 5 solution, while Figure 4.42 indicates that a passive layer formed in pH 1 solution will have a strong chromium depletion and is not comparable to a passive layer formed in pH 5 solution.

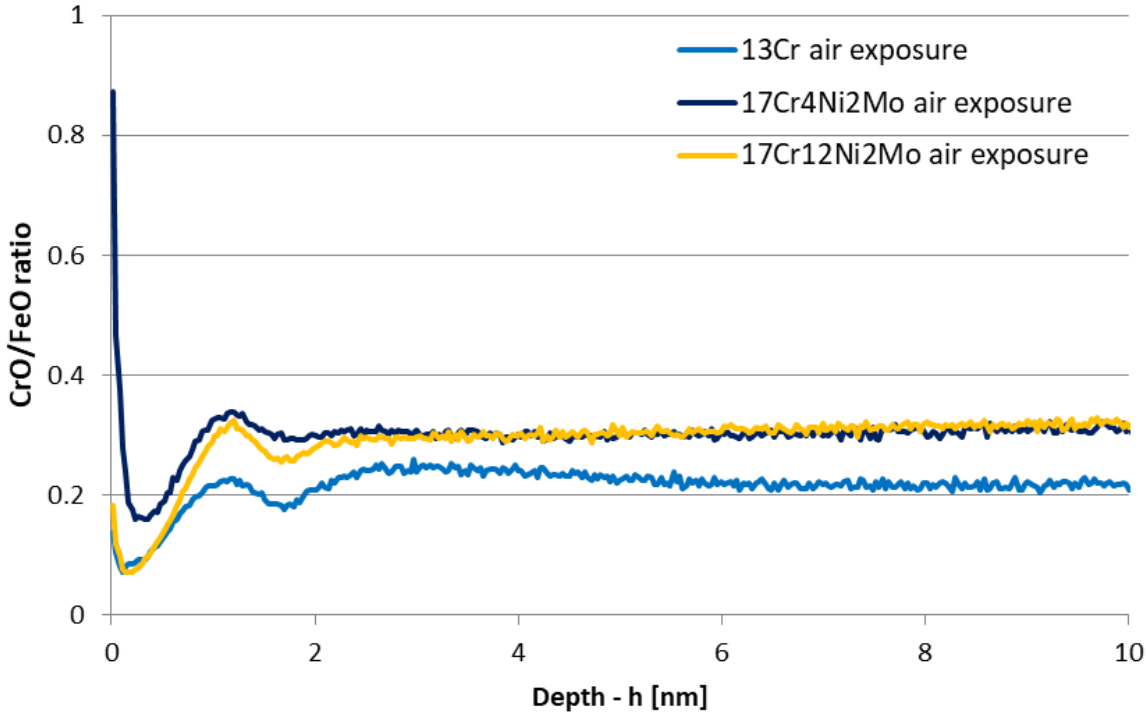

Figure 4.39: CrO^-/FeO^- ratio profiles obtained from 13Cr, 17Cr4Ni2Mo and 17Cr4Ni2Mo steel samples after exposure to air

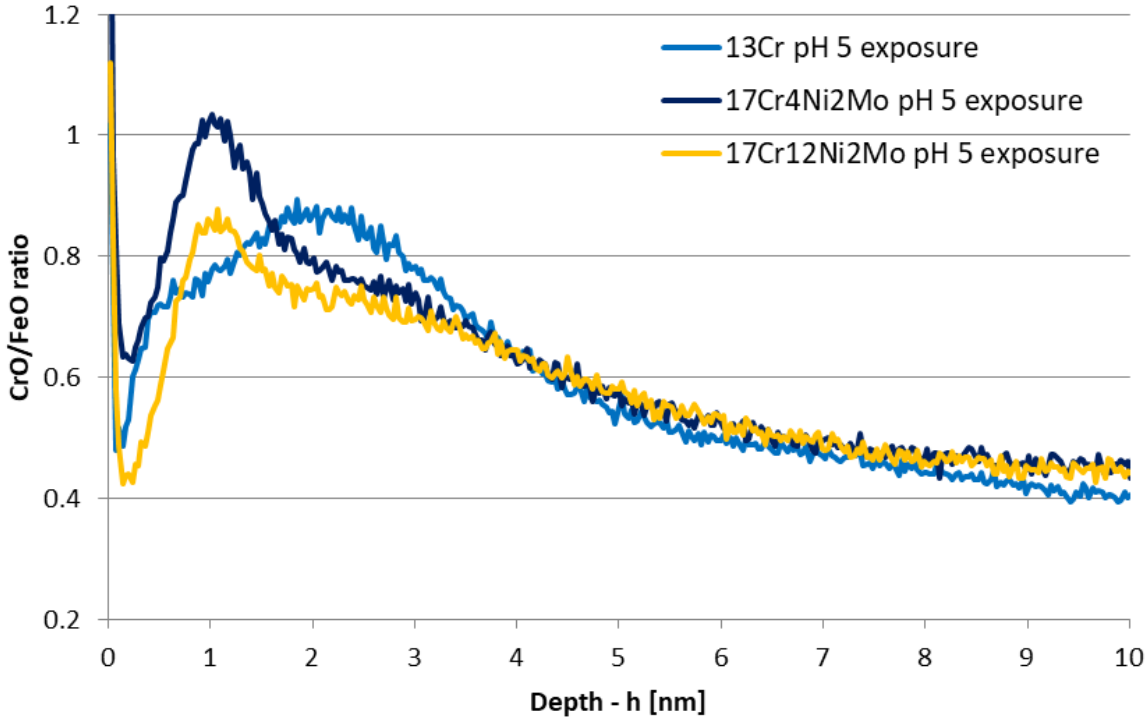

Figure 4.40: CrO^-/FeO^- ratio profiles obtained from 13Cr, 17Cr4Ni2Mo and 17Cr4Ni2Mo steel samples after exposure to pH 5 solution

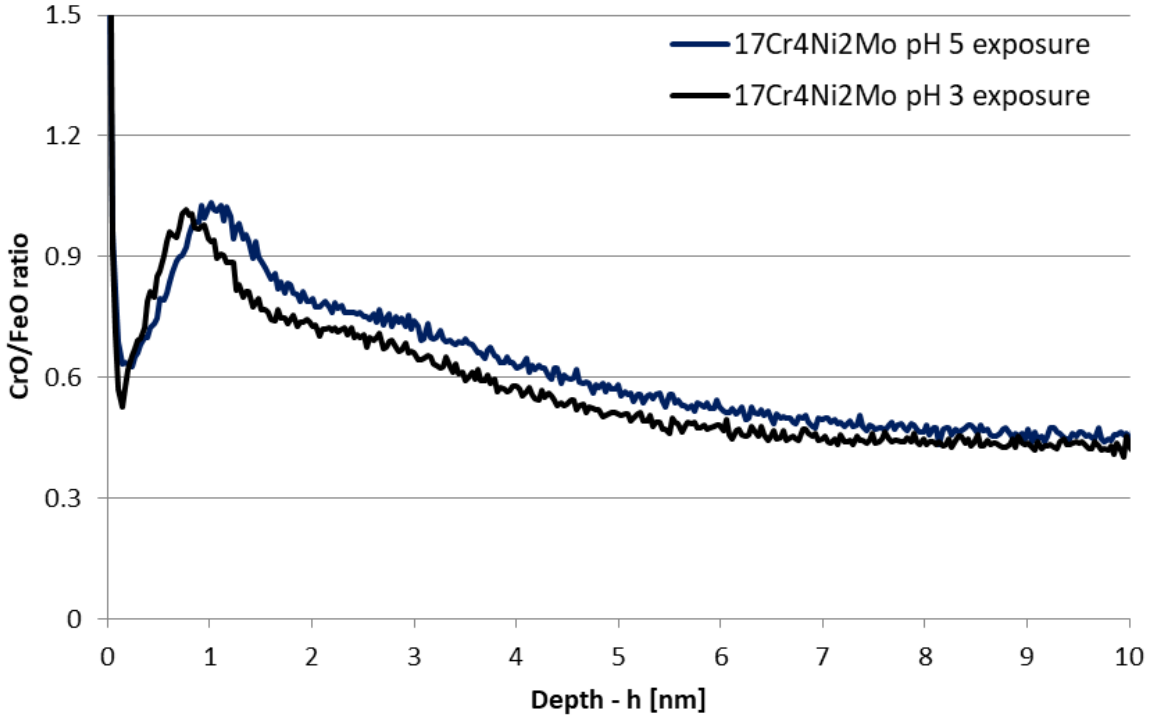

Figure 4.41: CrO^-/FeO^- ratio profiles obtained from 17Cr4Ni2Mo steel samples after exposure to pH 5 and pH 3 solutions

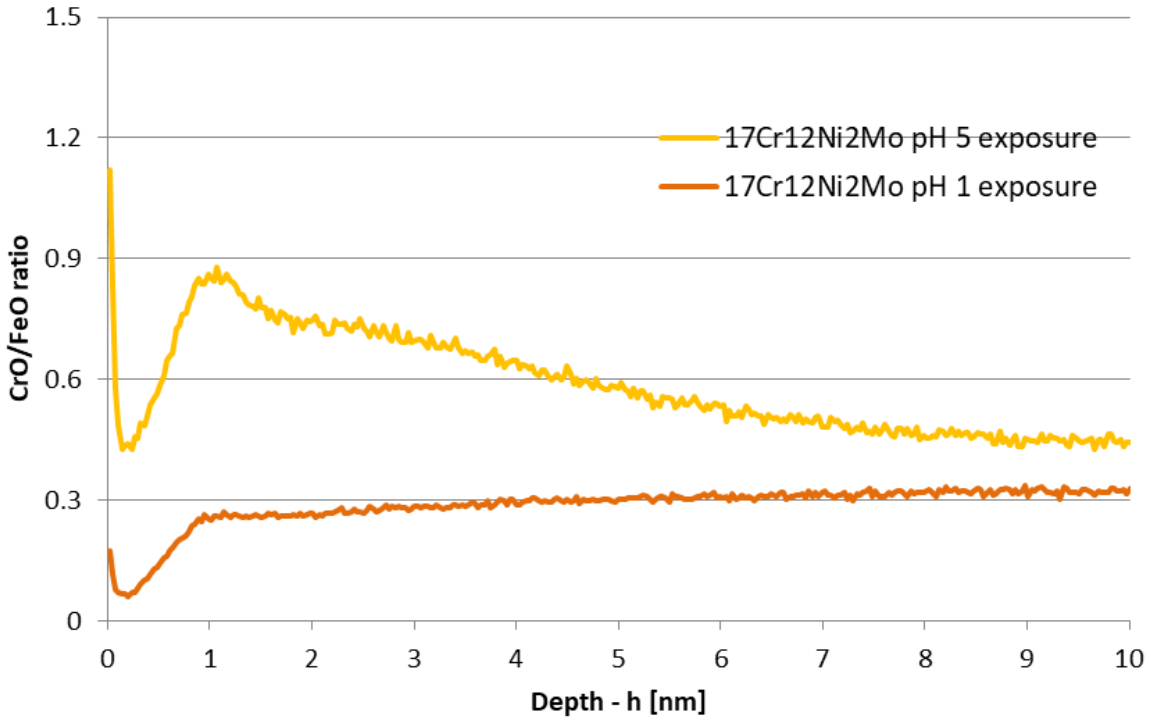

Figure 4.42: CrO^-/FeO^- ratio profiles obtained from 17Cr12Ni2Mo steel samples after exposure to pH 5 and pH 1 solutions

5 Discussion

5.1 Effect of chemical composition of stainless steels

Several different experiments detailed in this work have confirmed that the chemical composition of stainless steel has a significant effect on its corrosion resistance. While PREN is certainly a good quantitative indicator of the resistance of stainless steels to pitting (and crevice) corrosion, it does not fully explain all other effects of alloying, such as resistance to depassivation due to decreased solutrion pH levels or the effect of nickel on corrosion resistance.

The immersion tests performed showed that the amount of chromium, molybdenum and nickel has a strong effect on the corrosion resistance of stainless steel, both with regard to pitting and uniform corrosion. This is particularly apparent when comparing the results obtained from 13Cr, 13Cr6Ni2Mo and 15Cr6Ni2Mo steels, where the 13Cr steel is enhanced by adding Ni and Mo and is enhanced further by adding Cr. As a result, uniform corrosion occurs at lower pH values for the two more highly alloyed steels. Chemical depassivation tests show that a passive film created on 17Cr4Ni2Mo steel cannot withstand as aggressive a solution as a film created on 17Cr12Ni2Mo steel, despite their PREN values being nearly identical. On the contrary, the two steels require the same conditions for repassivation to occur, indicating that the increase in nickel content (either due to chemical composition or the resulting austenitic microstructure) causes the formed passive film to be more resistant to the use of a deaerated solution with a lower pH value but does not help with repassivation conditions. When comparing the passive layers formed on 17Cr4Ni2Mo and 17Cr12Ni2Mo formed in pH 5 solution, an increase in the molybdenum content can be seen in the passive layer of

17Cr12Ni2Mo (compare Figures 4.34 and 4.35), which is the main alloying element that improves corrosion resistance in low pH solutions (Figure 2.7).

Scratch tests performed on all steels showed that there is a large difference between repassivation speeds of 13Cr steel, which contains no nickel or molybdenum, and all other steel grades, which contain both additional alloying elements. According to the potentiodynamic tests 13Cr steel exhibits a higher corrosion current density (as well as an increased passive current density) compared to all other steels, which indicates a higher corrosion rate.

Passive layer chemistry analysis revealed a clear difference between the thickness of the passive layer formed on 13Cr steel and those formed on 17Cr4Ni2Mo and 17Cr12Ni2Mo in pH 5, 5 % NaCl solution at 30 °C (Figures 4.33 to 4.35). A thick native passive film of 13Cr (6.7 nm) means a high order of defects is present in the film, indicating poor protective properties, while the other steels had much thinner passive layers (2-3 nm), indicating a significantly lower defect density. Another difference between 13Cr and all other steels was that the 13Cr sometimes showed a discoloration on its surface (also known as rouging), whereas none of the other steels ever exhibited this behavior. This further shows the importance of nickel and molybdenum.

Certain results gained from immersion tests performed on 17Cr12Ni2Mo and 22Cr5Ni3Mo in comparison to 20Cr24Ni3Mo point to a negative effect of manganese on the pitting resistance of stainless steel, which is in agreement with the MARC equation from Speidel (equation 3). The manganese content of the investigated steel grades was, unfortunately, too low to fully confirm or disprove this statement. The negative impact of nickel found in the MARC equation, however, is in obvious contradiction to our results.

With the exception of the 13Cr steel, the scratch tests performed on different steels in 5 % NaCl solution at 30 °C showed no significant differences in the current decay slope, for times between 0.1 s < t < 1 s (see Table 4.10). This indicates that the exact amount of chromium, nickel and molybdenum does not affect repassivation rates (expressed as current decay slope steepness), only that they need to be present in certain quantities to allow fast repassivation when mechanical depassivation occurs in open circuit conditions. By comparing Figures 4.8 and 4.9 or Figures 4.10 to 4.15 with Figure 4.16 it can be seen that the pH of the solution also does not affect the repassivation speed, hence why the results from 20Cr24Ni6Mo in a pH 2 solution were added to Table 4.10. While repassivation kinetics may change under more extreme pH conditions, which change the chemical composition of the formed passive layer (see Figures 4.35, 4.37 and 4.41), these conditions were not tested due to equipment

limitations. Namely, the nickel based alloy used for the scratch test equipment would start to corrode at pH values below 2.

A schematic representation of the effect of alloying elements in different media on the repassivation behavior of stainless steels is shown in Figure 5.1. An increase in alloying elements results in a passive film with a smaller defect density than that of a less alloyed steel. The log i(t) vs log t slope is different only in a certain time frame (close to the time, where a steady state is achieved) however the level of passivity that can be reached, is different. A change of slopes cannot be excluded (lower alloyed materials with a more horizontal slope) but was not found in the (limited number of) tests performed.

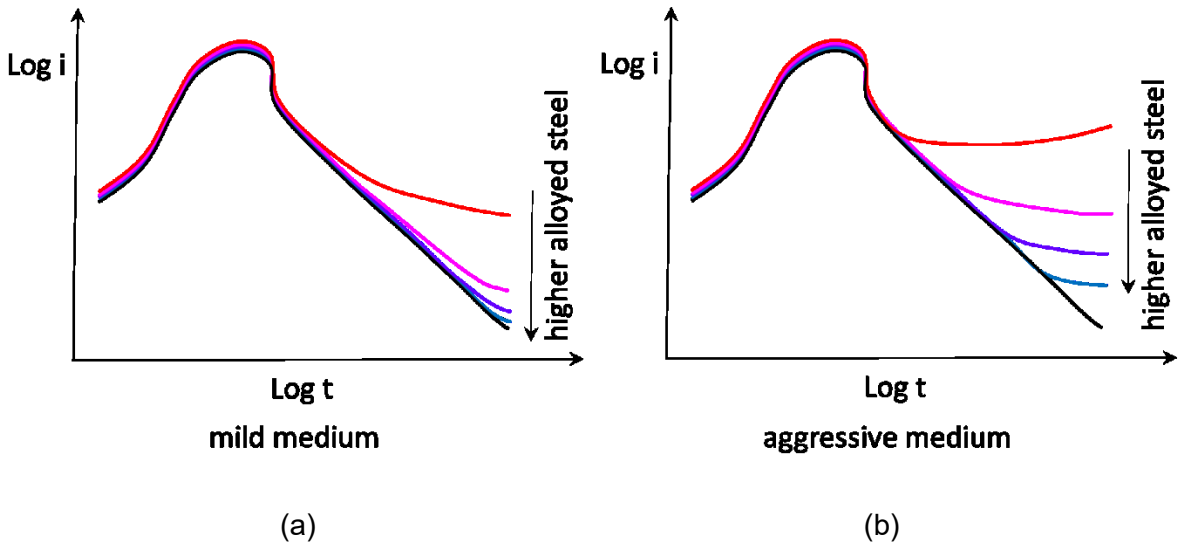

Figure 5.1: Schematic of repassivation behavior of differently alloyed stainless steels, (a) mild medium, (b) aggressive medium

5.2 Effect of temperature

Temperature has a strong effect on the aggressiveness of a solution, influencing the reaction speed in accordance with the Arrhenius equation. If the temperature of a solution exceeds a certain value (these high temperatures being outside the scope of our investigation), it will even affect the chemistry of the corrosion product formed [101].

Immersion tests showed uniform corrosion occurring at higher pH values for austenitic steels 17Cr12Ni2Mo and 20Cr24Ni6Mo at 80 °C compared to 30 °C, and pitting corrosion occurring

at higher pH values for bainitic steels 13Cr6Ni2Mo and 15Cr6Ni2Mo at 80 °C compared to 30 °C. This shows that both pitting and uniform corrosion are more likely to occur at higher temperatures. The extent to which increased temperature affects the pH value at which each type of corrosion occurs varied according to the type of steel.

The results of potentiodynamic experiments clearly show a difference between solutions at 30 and 80 °C, most notably increasing the corrosion current densities, as expected, but also affecting the passivity ranges, narrowing with an increase in temperature. The idea of critical pitting temperature has existed for a while [102], and is fully supported by these results. The best example of this is shown in Figures 4.5 and 4.6, where an increase in temperature has caused the 22Cr5Ni3Mo steel to have a breakthrough potential at approximately 0.1 V_{SCE}, whereas an electrolyte decomposition potential of approximately 1 V_{SCE} had been reached at the lower temperature – the increase in temperature thus significantly reduced the passive potential interval of this steel, indicating a strong reduction in corrosion resistance.

The scratch tests showed some effects of the solution temperature on the results obtained. Four tests were successfully performed in 5 % NaCl solution at 80 °C, three of which were carried out using 13Cr6Ni2Mo steel and one using 20Cr24Ni6Mo steel. All exhibited a high current density peak (compared to the same tests performed in 5 % NaCl solution at 30 °C), ranging between 38 and 57 mA/cm^2, with the 13Cr6Ni2Mo steel exhibiting very similar, small current density decay slopes of α_1 = 0.74, α_2 = 0.74 and α_3 = 0.77, indicating that the steel might be close to the edge of passivity and thus resulting in relatively slow repassivation. This reasoning is partially supported by the small difference (57 mV) between corrosion potential and repassivation potential obtained from the potentiodynamic experiment performed in 5 % NaCl solution at 80 °C, despite the higher pH of the solution used for potentiodynamic experiments. The corrosion current density obtained from this steel, however, is equal to 1.25 µA/cm^2, which is extremely high compared to the moderate value (0.28 µA/cm^2) of the 20Cr24Ni6Mo steel in the same conditions. The chemical depassivation test shows this steel to have a repassivation pH of 2.5 at 80 °C, which is close to the pH 3 solution in which the above mentioned scratch tests were performed, further supporting this reasoning.

The chemical depassivation tests showed very similar pH values for both depassivation and repassivation at 30 °C compared to 80 °C, for all four steel grades tested in both temperatures. The biggest difference in either depassivation or repassivation pH values between these two temperatures was 0.25 pH (1 step) and, in the case of the 13Cr steel, the pH values were higher at 80 °C, indicating that the temperature had little to no effect on whether or not repassivation is possible in a solution of a given pH.

5.3 Mechanical vs. chemical depassivation/repassivation

As mentioned in chapter 2, mechanical depassivation may occur due to several reasons. Regardless of the reason, there will be an active site where depassivation has occurred while the rest of the surface will be passive and will have a higher surface potential than the active site. This means that the mechanically damaged site will be a strong anode while the rest of the surface will be a cathode. After a monolayer of oxides is formed in the active region, the potential on the surface of the damaged area will increase, as there is now a barrier through which a potential drop occurs. The growth of the oxide layer will depend on the tendency of the metal to oxidize in the given solution and the potential drop across the film. The film will initially grow according to the high field ion conduction model but will later deviate from this as there is no set potential applied to the area. Instead, the potential depends on the areas that were not damaged (their size, how much of their electrochemical double layer was discharged, how quickly charge is built up, etc.). Since cathodic and anodic sites across the surface of a metallic part change over time, the amount of potential being applied to an area, which has already been partially repassivated, should change over time as well. When the more cathodic site is close to the partially repassivated area, the electric resistivity of both the metal and the solution will be smaller than when the more cathodic site is further away from the repassivating area, resulting in a larger potential being applied to the area at open circuit conditions. While this should theoretically occur even during the initial stages of repassivation the potential difference between the scratched and unscratched areas are large enough for the small differences in the potentials of the cathodic areas to be negligible.

The results of the scratch tests performed in open circuit conditions support this reasoning, as there is a certain result scatter between current decay slopes as well as current peak values, while the potential before performing a scratch is vastly different between experiments performed on the same steel in the same solution. The combination of scatter in current peak values and current decay slopes finally resulted in a scatter of repassivation time of approximately one order of magnitude (Figure 5.2, time required to reach current density of 0.01 mA/cm^2). With the small amount of experiments performed, no clear difference is seen in repassivation times between the steels containing nickel and molybdenum in 5 % NaCl solution at 30 °C.

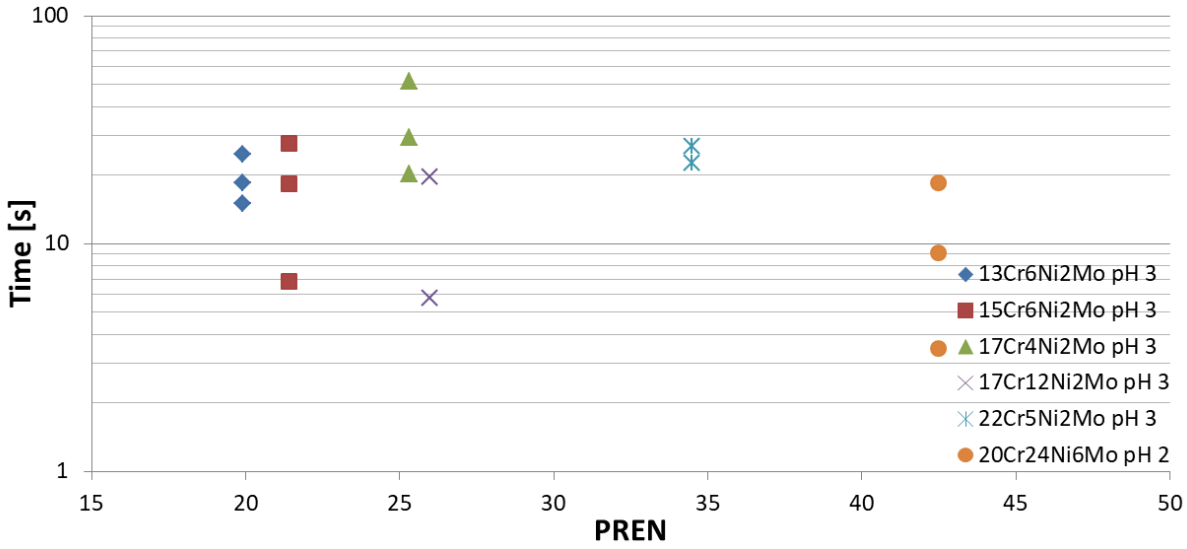

Figure 5.2: Time required for current density to decrease to 0.01mA/cm^2 after performing a scratch test as a function of the PREN values of the investigated steel grades, 5 % NaCl, 30 °C

While a current density equal to 0.01 mA/cm^2 is far higher than the corrosion current density for these materials according to potentiodynamic tests performed in 5 % NaCl at 30 °C (30 to 60 times higher, depending on the material), it is near the limit of the measuring equipment, when using a current range of 1 mA (which was necessary in order to capture the entire current transient). This current density is deemed sufficiently small to confirm the presence of a passive layer (if uniform corrosion is assumed a current density of 0.01 mA/cm^2 translates to a corrosion rate of approximately 0.1 mm/y). We can therefore surmise from Figure 5.2 that all of the steels containing nickel and molybdenum repassivate quickly enough at 30 °C to allow them to be used in their respective electrolytes, with the "repassivation times" ranging from 3.5 to 52 s, depending on the steel.

Another method of interpreting the data is observing the time required for the current density to decrease to 1 % of its peak value. While this method is not ideal, due to the different lengths of time required for the scratch event (a longer scratch time results in a smaller amount of bare metal being exposed in the same amount of time, resulting in a smaller current peak), it does allow for a glance into the initial repassivation rate. By observing this time frame the later stages of repassivation (where the potentials of the unscratched surfaces are close to the potential of the partially repassivated area) are avoided. Instead, it is focused on the earlier stages of repassivation, where the scratched area may be considered a very strong anode compared to the rest of the surface. Figure 5.3 shows the time required for the current to decrease to 1 % of the peak current as a function of PREN, where it becomes apparent that the amount of alloying elements helps with repassivation in the given electrolyte until a certain

amount of alloying elements is reached. Interestingly, the results from 20Cr24Ni6Mo steel in pH 2 solution shows a greater spread in the time required to achieve 1 % of the peak current (more than half an order of magnitude) compared to the other steel-solution combinations.

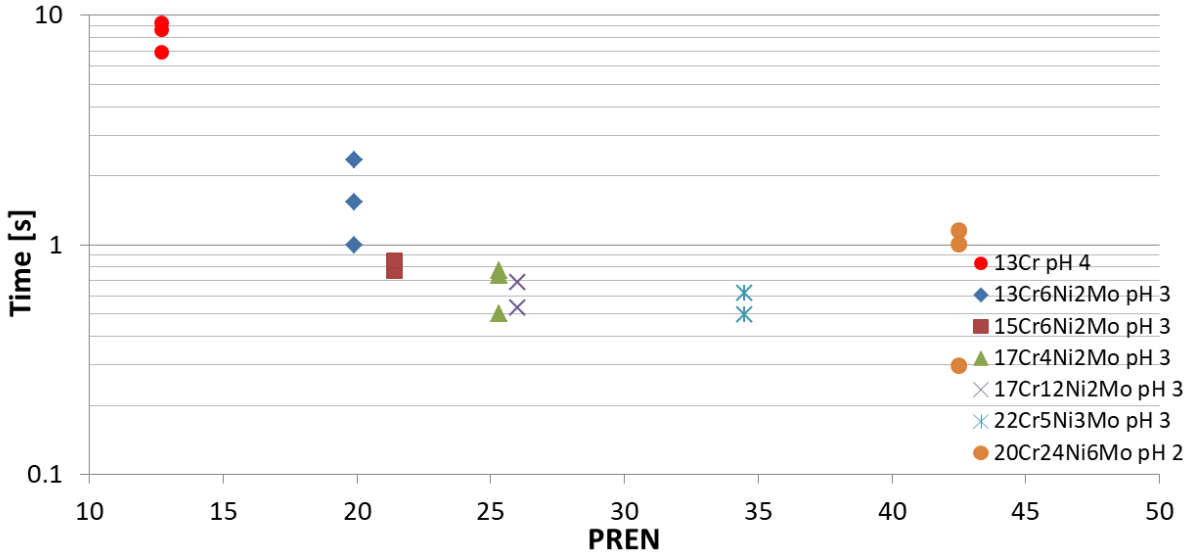

Figure 5.3: Time required for current density to decrease to 1 % of its peak value after performing a scratch test as a function of the PREN values of the investigated steel grades, 5 % NaCl, 30 °C

Chemical depassivation may occur in two ways – either locally in the form of a crevice or a pit, or generally in the form of uniform corrosion. Pitting depends mainly on the presence of halide ions such as Cl^-. Once a pit has nucleated it may propagate, further decreasing the pH of the solution inside the pit until it has propagated enough for the oxide layer above the pit to break away and cause a so called washout. Once this occurs, fresh solution will enter the pit and allow repassivation of the metal within it. If this line of reasoning is correct, solutions that maintain an existing passive layer but do not allow repassivation should result in the constant propagation of pits, until the passive layer is completely undermined and the corrosive attack may be described as general corrosion. Otherwise, alternative lines of reasoning outlined in chapter 2 might prove to be better suited to explain the processes of pit repassivation.

Uniform corrosion occurred on the stainless steel samples investigated, when the solution was simply too aggressive for the passive layer to persist. Once the pH is low enough, or the temperature is high enough, the passive layer will fail, causing the underlying metal to corrode freely. Whether this is due to the passive layer breaking down locally and corrosion spreading from those areas or due to the uniform dissolution of the entire passive layer primarily depends on the properties of the steel and solution used – the bainitic 13Cr6Ni2Mo in 5 % NaCl solution at 80 °C might be more prone to pitting corrosion spreading into very large pits, eventually

covering the entire surface, whereas the 17Cr12Ni2Mo in 5 % NaCl solution at 30 °C caused gradual thinning of the passive film, resulting in an etching effect which occurred across the entire surface of the specimen (as seen in Figure 4.1 (c)). At low enough pH values this type of corrosion occurred in both immersion tests and chemical depassivation tests. The chemical depassivation tests also yielded repassivation pH values, which were in most cases notably higher than the pH values for depassivation (more than 1 pH step), showing that uniform corrosion will not easily occur on passive surfaces. When it does occur, however, it will continue until the solution undergoes a drastic decrease in aggressivity.

5.4 Passive layer forming vs. passive layer maintaining conditions

According to the well-known Faraday experiment regarding passivity, a piece of iron introduced into concentrated HNO_3 acid will cause the formation of a passive iron oxide layer due to the highly oxidizing properties of HNO_3 despite the low pH value. If water is added to this solution the passive layer will persist until it is damaged. Once it has been damaged, a strong reaction will take place, rapidly dissolving the iron due to the high potential caused by the nitric acid solution (practically speaking the potential of the system will be in the active peak region of iron, causing the corrosion rate to increase exponentially with the increase in potential). This experiment thus proves that conditions exist for iron and steel where a passive layer may be maintained, but does not reform if damaged.

The Faraday experiment on passivity was the inspiration to prove the existence of such conditions for the stainless steels investigated in this work. While the chemical depassivation tests seem to prove these conditions, it is important to note that a corrosion product layer was often formed on top of the samples during uniform corrosion, which might affect the results in some way. Furthermore, this is a completely new method which relies on potential measurements and visual sample observation for indicators of the cathodic reaction (H_2 gas generation) – neither of which quantify the rate of corrosion.

It was therefore decided to perform an additional scratch test on a steel in the pH region between depassivation and repassivation pH values. 13Cr6Ni2Mo steel was chosen for this purpose, due to the large difference between these two values. To do this, the steel electrodes were passivated for 24 hours in a deaerated 5 % NaCl, pH 3 solution at 30 °C, followed by the addition of HCl to decrease the solution pH to 2. After a level of pH 2 had been achieved, the electrodes were left in the new solution for 4 hours to reach steady state conditions, followed

by scratch creation. After scratching, the electrodes were left in the solution for an additional 24 hours before removing them from the solution, cleaning them and observing the surface with an optical microscope. Figure 5.4 shows the surface of the scratched electrode, where the inside of the scratched area has become matt gray due to the buildup of corrosion products, while the original surface still shows grind marks and has remained reflective, indicating that passivity was maintained there.

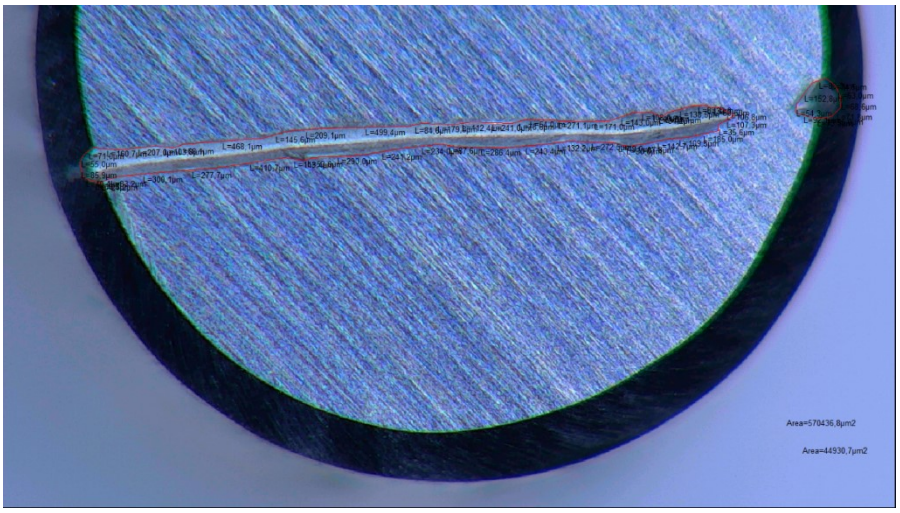

Figure 5.4: Surface of WE 1 from 13Cr6Ni2Mo steel after scratch test in pH 2, 5 % NaCl at 30 °C, scratched area has suffered uniform corrosion, while the rest of the electrode has remained passive

The current was measured in the same way as in previous scratch tests. The difference in current between immediately before scratching and 180 seconds after scratching was equal to 290 nA (Figure 5.5) – a value that only increased over the following 24 hour immersion (most likely due to corrosion increasing the affected area). Considering general corrosion in the scratched area of 0.71 mm^2, the calculated corrosion rate was at least 0.41 mm/y – this calculated corrosion rate is correct if no current is flowing from the scratched area into the unscratched area of WE1, which, however, will take place. Due to the distance between the two electrodes one can only assume a large amount of the current flows into the cathodic region of WE1, but a conservative way of evaluating it would be to simply compare the cathodic areas of both electrodes, which are approximately equal, meaning the corrosion rate inside the scratched area is at least twice the value calculated above.

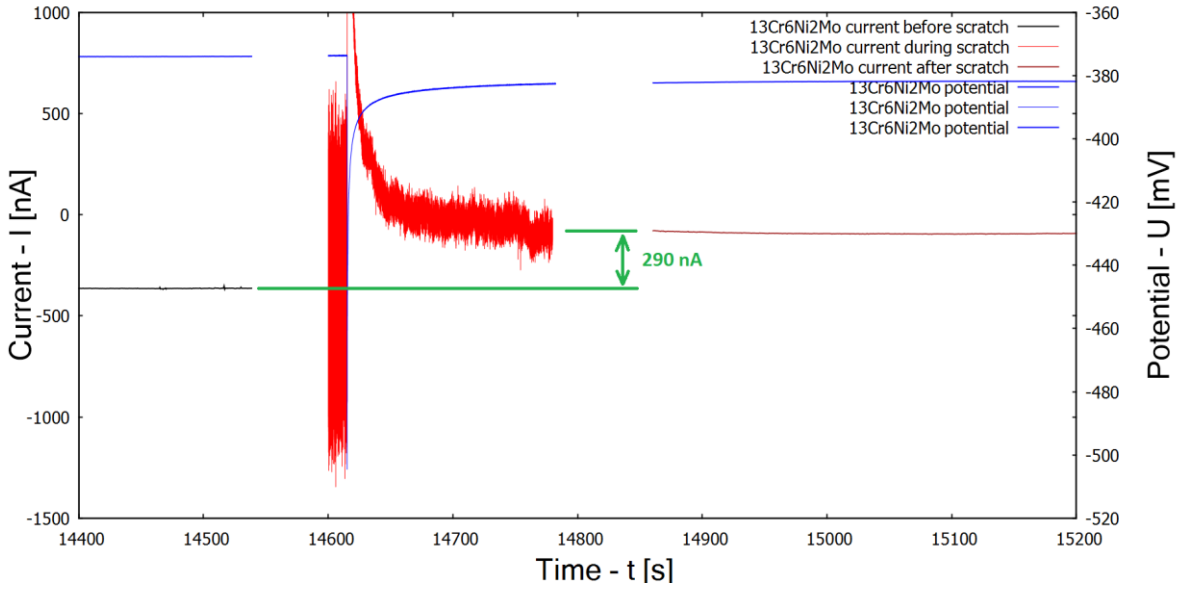

Figure 5.5: Current measurement before scratching, during scratch creation and after scratch creation confirms a current change of 290 nA between the two working electrodes

This additional scratch test thus proves the existence of passivity maintaining solutions that do not allow repassivation, although the exact mechanisms involved are unknown. The most likely explanation is that a potential well below the stability line of a passive layer in a given environment is needed to dissolve it, similar to how the iron oxide in the Faraday experiment does not begin to dissolve unless the potential is decreased below the passivation potential as water is added to the concentrated nitric acid.

In this particular experiment the passive layer persisted for a period of 24 hours in the pH 2 solution. Most steels in the chemical depassivation tests have resulted in appearance of uniform corrosion within 1 to 6 hours after achieving the depassivation pH. Since even the area adjacent to the scratched area has not depassivated (which is where we would expect the corrosive attack to spread) and the 13Cr6Ni2Mo steel withstood a pH between repassivation and depassivation pH values in the chemical depassivation tests for 36 hours without producing H_2 gas on a specific part of the surface (which might occur in the case of a pit that was constantly growing) it is not unreasonable to expect that this steel might avoid general depassivation in such a solution indefinitely.

These considerations give rise to the question of what would occur to pits in such an environment. While it is clear that pits will nucleate and grow in such an environment due to the presence of Cl^- ions, it is unclear whether or not they can repassivate. To answer this question, localized pH and chloride concentrations in pits have to be determined, either experimentally or through simulation.

6 Conclusions

Several conclusions can be drawn from the experiments performed in this thesis. These are divided into scientific results, and practical recommendations for the industry.

Scientific results:

1. It was confirmed that the chemical composition of stainless steel affects both pitting resistance and resistance to uniform corrosion. Even a small increase in chromium content may significantly affect the corrosion resistance properties of stainless steel.
2. Scratch tests performed at open circuit potential do not yield precise data about repassivation rates. Instead it simulates field conditions and provides a rough estimate about the required time to repassivate steel in a certain solution, with a large scatter of results both with regard to peak current densities and current decay slopes. Repassivation was found to take place within the first seconds after scratching, but healing of the passive layer and reaching a steady state takes much longer, with the exact time depending on how close to the limits of passivity the steel is exposed to.
3. A certain amount of alloying elements is required for effective repassivation in a given electrolyte. Any further increase in the amount of alloying elements does not significantly affect the repassivation rates but may improve the stability and protective properties of the passive film.
4. Increasing the temperature of the solution does not significantly affect repassivation pH values. The data obtained from immersion tests and chemical depassivation tests are somewhat conflicting as to how a temperature increase may affect the pH values for depassivation.

5. Results show that when the steel comes close to its chemical depassivation limit the thickness of the passive layer increases. Otherwise passive layers have a thickness of approximately 2 nm. They show a Fe-rich outer sub-layer and a Cr-rich inner sub-layer. When put in a moderately aggressive electrolyte (such as brine with a pH value of around 4), iron species dissolve from the surface of the passive film. A very acidic electrolyte (brine with a pH value of 1), however, instead causes the chromium species to dissolve and the passive layer primarily consists of molybdenum and iron species near the surface.
6. For all tested steels containing both nickel and molybdenum conditions exist whereby passivity is maintained but repassivation is not possible. In fact, steels containing more nickel seem to have a larger difference between the pH at which depassivation and repassivation occur, although other factors such as carbon content or microstructure may also have an effect on these values.

Recommendations for the industry:

1. The difference between activation pH and repassivation pH is equal to or smaller than 1 pH unit and the depassivation pH was never higher than 3.25 (for 13Cr). This means that after acidizing jobs, repassivation can be expected in deaerated conditions.
2. After acidizing repassivation occurs very quickly (within seconds), when the pH is increased above the repassivation values found in Tables 4.11 and 4.12.
3. Alloying 13Cr steel with Ni and Mo results in a pronounced improvement in repassivation properties as well as corrosion resistance. It is believed that this is primarily due to alloying with Mo, which improves the acid resistance of the stainless steel, whereas the nickel mainly retards the corrosion rates within pits.
4. Mechanical depassivation will locally activate the surface. As long as no second impact happens at the identical site within a very short time, this will not result in severe corrosion rates.

7 References

[1] P. Schmuki, From Bacon to barriers: a review on the passivity of metals and alloys, Journal of Solid State Electrochemistry 6 (2002) 145-164

[2] U. Stimming, J.W. Schultze, A semiconductor model of the passive layer on iron electrodes and its application to electrochemical reactions, Electrochemica Acta 24 (1979) 859-869

[3] C.-O.A. Olsson, D. Landolt, Passive films on stainless steels – chemistry, structure, growth, Electrochimica Acta 48 (2003) 1093-1104

[4] B. Beidokhti, A. Dolati, A.H. Koukabi, Effects of alloying elements and microstructure on the susceptibility of the welded HSLA steel to hydrogen-induced cracking and sulfide stress cracking, Material Science and Engineering A 507 (2009) 167-173

[5] W. Khalil, S. Haupt, H.-H. Strehblow, The thinning of the passive layer of iron by halides, Materials and Corrosion 36 (1985) 16-21

[6] M. Pourbaix, Atlas of Electrochemical Equilibria in Aqueous Solutions, NACE, Cebelcor, Houston-Brussels, 1974

[7] A. Atrens, The Secondary Passive Film for Type 304 Stainless Steel in 0.5 M H_2SO_4, Journal of The Electrochemical Society 144 (1997) 3697-3704

[8] C. Loable, I.N. Viçosa, T.J. Mesquita, M. Mantel, R.P. Nogueira, G. Berthomé, E. Chauveau, V. Roche, Synergy between molybdenum and nitrogen on the pitting corrosion and passive film resistance of austenitic stainless steels as a pH-dependent effect, Materials Chemistry and Physics (2016), doi: 10.1016/j.matchemphys.2016.10.049

[9] K. Lorenz, G. Medawar, Corrosion of austenitic chromium-nickel steels with and without nitrogen additions and their resistance to chloride solutions, Thyssenforschung 1 (1969) 97-108

[10] G. Mori, D. Bauernfeind, Pitting and crevice corrosion of superaustenitic stainless steels. Materials and Corrosion 55 (2004) 164–173

[11] R.F.A. Jargelius-Pettersson, Application of the Pitting Resistance Equivalent Concept to Some Highly Alloyed Austenitic Stainless Steels, Corrosion 54 (1998) 162–168

[12] J.Y. Jonsson, L. Wegrelius, S. Heino, M. Liljas, R. Östberg, The Influence of Tungsten (W) on Properties in High Nitrogen Stainless Steels, Materials Science Forum 318-320 (1999) 511–516

[13] M.O. Speidel, Nitrogen Containing Austenitic Stainless Steels, Materialwissen-schaft und Werkstofftechnik 37 (2006) 875–880

[14] S. Holzleitner, Zum Mechanismus der chloridinduzierten Spannungsrisskorrosion hochlegierter austenitischer Stähle, Ph.D. thesis, Montanuniversität Leoben, Leoben, 2008, 1-147

[15] A. Visser, Chloridinduzierte Korrosion an austenitischen Stählen unter schwingender Beanspruchung, Ph.D. thesis, Montanuniversität Leoben, Leoben, 2016, 1-152

[16] C.R. Clayton, I. Olefjord, Passivity of Austenitic Stainless Steels, in: P. Marcus (ed.): Corrosion Mechanisms in Theory and Practice, 2nd edition, Marcel Dekker, New York – Basel, 2002, 217-242

[17] C.-O.A. Olsson, S.E. Hörnström, An AES and XPS study of the high alloy austenitic stainless steel 254 SMO® tested in a ferric chloride solution, Corrosion Science 36 (1994) 141–151

[18] K. Sugimoto, Y. Sawada, The role of molybdenum additions to austenitic stainless steels in the inhibition of pitting in acid chloride solutions, Corrosion Science 17 (1977) 425–445

[19] K. Hashimoto, K. Asami, A. Kawashima, H Habazaki, E. Akiyama, The role of corrosion-resistant alloying elements in passivity, Corrosion Science, 49 (2007) 42–52

[20] K. Hashimoto, K. Asami, K. Teramoto, An X-ray photo-electron spectroscopic study on the role of molybdenum in increasing the corrosion resistance of ferritic stainless steels in HCl, Corrosion Science 19 (1979) 3–14

[21] H. Ogawa, H. Omata, I. Itoh, H. Okada, Auger Electron Spectroscopic and Electrochemical Analysis of the Effect of Alloying Elements on the Passivation Behavior of Stainless Steels, Corrosion 34 (1978) 52–60

[22] I. Olefjord, B. Brox, U. Jelvestam, Surface Composition of Stainless Steels during Anodic Dissolution and Passivation Studied by ESCA, Journal of The Electrochemical Society 132 (1985) 2854-2861

[23] M. Urquidi, D.D. Macdonald, Solute-Vacancy Interaction Model and the Effect of Minor Alloying Elements on the Initiation of Pitting Corrosion, Journal of The Electrochemical Society 132 (1985) 555-558

[24] Y.C. Lu, M.B. Ives, C.R. Clayton, Synergism of alloying elements and pitting corrosion resistance of stainless steels, Corrosion Science 35 (1993) 89-96

[25] Y.C. Lu, J.L. Luo, M.B. Ives, Effect of Nitriding on the Anodic Behavior of Iron and Its Significance in Pitting Corrosion of Iron.Based Alloys, Corrosion 47 (1991) 835-839

[26] G.P. Halada, D. Kim, C.R. Clayton, Influence of Nitrogen on Electrochemical Passivation of High-Nickel Stainless Steels and Thin Molybdenum-Nickel Films, Corrosion 52 (1996) 36–46

[27] J. Yang, S. Wang, D. Xu, Y. Guo, C. Yang, Y. Li, Effect of ammonium chloride on corrosion behavior of Ni-based alloys and stainless steel in supercritical water gasification process, International Journal of Hydrogen Energy 42 (2017) 19788–19797

[28] K. Park, H. Kwon, Effects of Mn on the localized corrosion behavior of Fe–18Cr alloys, Electrochimica Acta 55 (2010) 3421–3427

[29] H. Spähn, Elektrochemische Korrosion in wässerigen Lösungen ohne gleichzeitige mechanische Beanspruchung, in E. Kunze (ed.): Korrosion und Korrosionsschutz, Band 1, Wiley-VCH, Berlin – Weinheim, 2001, 164

[30] H. Krawiec, V. Vignal, O. Heintz, R. Oltra, Influence of the dissolution of MnS inclusions under free corrosion and potentiostatic conditions on the composition of passive films and the electrochemical behaviour of stainless steels, Electrochimica Acta 51 (2006) 3235–3243

[31] M.P. Ryan, D.E. Williams, R.J. Chater, B.M. Hutton, D.S. McPhail, Why stainless steel corrodes, Nature 415 (2002) 770–774

[32] Q. Meng, G.S. Frankel, H.O. Colijn, S.H. Goss, Stainless-steel corrosion and MnS inclusions, Nature 424 (2003) 389-90

[33] M.P. Ryan, D.E. Williams, R.J. Chater, B.M. Hutton, D.S. McPhail, Stainless-steel corrosion and MnS inclusions, Nature 424 (2003) 390

[34] N. Sato, T. Noda, K. Kudo, Thickness and structure of passive films on iron in acidic and basic solution, Electrochimica Acta 19 (1974) 471–475

[35] K. Osozawa, H.-J. Engell, The anodic polarization curves of iron-nickel-chromium alloys, Corrosion Science 6 (1966), 389–393

[36] A. Barbucci, G. Bruzzone, M. Delucchi, M. Panizza, G. Cerisola, Breakdown of passivity of aluminium alloys by intermetallic phases in neutral chloride solution, Intermetallics 8 (2000) 305–312

[37] M. Cabrini, A. Cigada, G. Rondell, B. Vicentini, Effect of different surface finishing and of hydroxyapatite coatings on passive and corrosion current of Ti6Al4V alloy in simulated physiological solution, Biomaterials 18 (1997) 783–787

[38] S. Hornkjøl, Anodic growth of passive films on niobium and tantalum, Electrochimica Acta 36 (1991) 1443–1446

[39] S. Sutthiruangwong, G. Mori, Corrosion properties of Co-based cemented carbides in acidic solutions, International Journal of Refractory Metals and Hard Materials 21 (2003) 135–145

[40] S. Sutthiruangwong, G. Mori, R. Kösters, Passivity and pseudopassivity of cemented carbides. International Journal of Refractory Metals and Hard Materials 23 (2005) 129–136

[41] S. Sutthiruangwong, G. Mori, Influence of refractory metal carbide addition on corrosion properties of cemented carbides, Materials and Manufacturing Processes 20 (2005) 47–56

[42] G. Mori, T. Vogl, J. Haberl, W. Havlik, T. Schöberl, P. Hosemann, Erosion-Corrosion Rates of Corrosion-Resistant Alloys Under High-Velocity Multiphase Conditions, Corrosion 70 (2014) 579–590

[43] J. Kovač, A. Legat, B. Zajec, T. Kosec, E. Govekar, Detection and characterization of stainless steel SCC by the analysis of crack related acoustic emission, Ultrasonics 62 (2015) 312–322

[44] H.S. Klapper, B. Zajec, A. Heyn, A. Legat, Elucidating Nucleation Stages of Transgranular Stress Corrosion Cracking in Austenitic Stainless Steel by In Situ Electrochemical and Optical Methods, Journal of The Electrochemical Society 166 (2019) C3326–C3335

[45] T. Magnin, L. Coudreuse, Corrosion fatigue mechanisms in b.c.c. stainless steels, Acta Metallurgica 35 (1987) 2105–2113

[46] T. Magnin, Recent Advances for Corrosion Fatigue Mechanisms, ISIJ International 35 (1995) 223–233

[47] A. Berradja, F. Bratu, L. Benea, G. Willems, J.P. Celis, Effect of sliding wear on tribocorrosion behaviour of stainless steels in a Ringer's solution, Wear 261 (2006) 987–993

[48] J. Chen, Q. Zhang, Q. Li, S. Fu, J. Wang, Corrosion and tribocorrosion behaviors of AISI 316 stainless steel and Ti6Al4V alloys in artificial seawater, Transactions of Nonferrous Metals Society of China 24 (2014) 1022–1031

[49] J. Marian, J. Knap, M. Ortiz, Nanovoid Cavitation by Dislocation Emission in Aluminum, Physcal Review Letter 93 (2004) 165503-1 – 165503-4

[50] N.J. Laycock, R.C. Newman, Temperature dependence of pitting potentials for austenitic stainless steels above their critical pitting temperature, Corrosion Science 40 (1998) 887–902

[51] M.H. Nazari, X. Shi, Vehicle Risks of Winter Road Operations and Best Management Practices, Sustainable Winter Road Operations (2018) 241–272

[52] D.D. MacDonald, The Point Defect Model for the Passive State, Journal of The Electrochemical Society 139 (1992) 3434-3449

[53] Z. Ahmad, Principles of corrosion engineering and corrosion control, Chapter 4; Types of Corrosion, Butterworth – Heinemann, Oxford, 2006, 120-270

[54] G.T. Burstein, C. Liu, R.M. Souto, S.P. Vines, Origins of pitting corrosion. Corrosion Engineering, Science and Technology 39 (2004) 25–30

[55] F.F. Berg, Corrosion Diagrams, VDI-Verlag, Düsseldorf, 1965, 12

[56] H. Meng, X. Hu, A. Neville, A systematic erosion–corrosion study of two stainless steels in marine conditions via experimental design, Wear 263 (2007) 355–362

[57] A. Neville, M. Reyes, H. Xu, Examining corrosion effects and corrosion/erosion interactions on metallic materials in aqueous slurries, Tribology International 35 (2002) 643–650

[58] A. Neville, X. Hu, Mechanical and electrochemical interactions during liquid–solid impingement on high-alloy stainless steels, Wear 251 (2001) 1284–1294

[59] V.A.D. Souza, A. Neville, Corrosion and synergy in a WCCoCr HVOF thermal spray coating—understanding their role in erosion–corrosion degradation, Wear 259 (2005) 171–180

[60] P.I. Marshall, G.T. Burstein, Effects of alloyed molybdenum on the kinetics of repassivation on austenitic stainless steels, Corrosion Science 24 (1984) 463–478

[61] H.S. Kwon, E.A. Cho, K.A. Yeom, Prediction of Stress Corrosion Cracking Susceptibility of Stainless Steels Based on Repassivation Kinetics, Corrosion 56 (2000) 32–4057

[62] M. Stern, Evidence for a Logarithmic Oxidation Process for Stainless Steel in Aqueous Systems, Journal of The Electrochemical Society 106 (1959) 376-381

[63] E.A. Cho, C.K. Kim, J.S. Kim, H.S. Kwon, Quantitative analysis of repassivation kinetics of ferritic stainless steels based on the high field ion conduction model, Electrochimica Acta 45 (2000) 1933–1942

[64] J.-B. Lee, Effects of alloying elements, Cr, Mo and N on repassivation characteristics of stainless steels using the abrading electrode technique, Materials Chemistry and Physics 99 (2006) 224–234

[65] R. Carranza, J. Galvele, Repassivation kinetics in stress corrosion cracking - I. Type AISI 304 stainless steel in chloride solutions, Corrosion Science 28 (1988) 233–249

[66] G.T. Burstein, K. Sasaki, Electrochemical Reactions of Freshly Bared Metal Surfaces Using the Fluid Impacted Guillotined Electrode, Journal of The Electrochemical Society 148 (2001) B282-B287

[67] G.S. Frankel, C.V. Jahnes, V. Brusic, A.J. Davenport, Repassivation Transients Measured with the Breaking-Electrode Technique on Aluminum Thin-Film Samples, Journal of The Electrochemical Society 142 (1995) 2290-2295

[68] J. Wloka, T. Hack, S. Virtanen, Repassivation Kinetics of Al-Alloys for Aircraft Structures, P. Marcus, V. Maurice (ed.), Passivation of Metals and Semiconductors, and Properties of Thin Oxide Layers, Elsevier, Amsterdam, 2006, 537–542, doi:10.1016/b978-044452224-5/50083-4

[69] S.B. Madden, D.J. Moosbauer, J.R. Scully, Effects of Chromate and Molybdate Ions on Scratch Repassivation Behavior of Precipitation Hardened Aluminum Alloys, ECS Transactions 50 (2013) 57–78

[70] G.S. Chen, M. Gao, R.P. Wei, Microconstituent-Induced Pitting Corrosion in Aluminum Alloy 2024-T3, Corrosion 52 (1996) 8–15

[71] D.A. Little, B.J. Connolly, J.R. Scully, An electrochemical framework to explain the intergranular stress corrosion behavior in two Al–Cu–Mg–Ag alloys as a function of aging, Corrosion Science 49 (2007) 347–372

[72] T.R. Beck, Reactions and Kinetics of Newly Generated Titanium Surfaces and Relevance to Stress Corrosion Cracking, Corrosion 30 (1974) 408–414

[73] T.R. Beck, Stress Corrosion Cracking of Titanium Alloys, Journal of The Electrochemical Society 115 (1968) 890-896

[74] G. Mori, private communication, Graz, 9th December 2019

[75] R.M. Fernández-Domene, E. Blasco-Tamarit, D.M. García-García, J. García-Antón, Cavitation corrosion and repassivation kinetics of titanium in a heavy brine LiBr solution evaluated by using electrochemical techniques and Confocal Laser Scanning Microscopy, Electrochimica Acta 58 (2011) 264–275

[76] D.G. Kolman, J.R. Scully, Limitations of Potentiostatic Repassivation Techniques and Their Relationship to the Applicability of the High Field Approximation to the Repassivation of Titanium, Journal of The Electrochemical Society 142 (1995) 2179-2188

[77] D.G. Kolman, J.R. Scully, On the Repassivation Behavior of High-Purity Titanium and Selected α, β, and β + α Titanium Alloys in Aqueous Chloride Solutions, Journal of The Electrochemical Society 143 (1996) 1847-1860

[78] B.-Y Kim, C.-J. Park, H.-S. Kwon, Repassivation Kinetics of Zirconium Alloys Investigated by a Scratching Electrode Technique, Metals and Materials International 14 (2008) 71–75

[79] L. Guan, Y. Li, G. Wang, Y. Zhang, L.-C. Zhang, pH dependent passivation behavior of niobium in acid fluoride-containing solutions, Electrochimica Acta 285 (2018) 172–184

[80] A.G. Gad-Allah, W.A. Badawy, H.A. Abd El-Rahman, M.M. Abou Romia, Kinetics of the passivation of molybdenum in salt solutions as inferred from impedance and potential measurements, Surface and Coatings Technology 31 (1987) 117–126

[81] H. Xu, D. Sun, H. Yu, Repassivation behavior of 316L stainless steel in borate buffer solution: Kinetics analysis of anodic dissolution and film formation, Applied Surface Science 357 (2015) 204–213

[82] S. Ahila, B. Reynders, H.J. Grabke, The evaluation of the repassivation tendency of Cr-Mn and Cr-Ni steels using scratch technique, Corrosion Science, 38 (1995) 1991–2005

[83] R.W. Bosch, B. Schepers, M. Vankeerberghen, Development of a scratch test in an autoclave for the measurement of repassivation kinetics of stainless steel in high temperature high pressure water, Electrochimica Acta, 49 (2004) 3029–3038

[84] G.T. Burstein, R.J. Cinderey, The potential of freshly generated metal surfaces determined from the guillotined electrode—A new technique, Corrosion Science 32 (1991) 1195–1211

[85] R.J. Cinderey, G.T. Burstein, The effects of chromate on the transient repassivation potential of aluminium in chloride solution, Corrosion Science, 33 (1992) 493–498

[86] G.T. Burstein, C. Liu, The cathodic reaction during repassivation of aluminium in open circuit. Corrosion Science 37 (1995) 1151–1162

[87] G.T. Burstein, C. Liu, Time-resolved electrochemical impedance of the guillotined aluminium electrode, Electrochimica Acta 39 (1994) 873–882

[88] G.T. Burstein, R.M. Organ, Repassivation and pitting of freshly generated aluminium surfaces in acidic nitrate solution, Corrosion Science 47 (2005) 2932–2955

[89] T. Yamamoto, K. Fushimi, M. Seo, S. Tsuri, T. Adachi, H. Habazaki, Depassivation–repassivation behavior of type-312L stainless steel in NaCl solution investigated by the micro-indentation, Corrosion Science 51 (2009) 1545–1553

[90] K. Fushimi, T. Yamamoto, K. Azumi, M. Seo, H. Habazaki, A numerical model for current transients during micro-indentation of passive iron surface. Electrochimica Acta 52 (2007) 6901–6910

[91] T. Yamamoto, K. Fushimi, H. Habazaki, H. Konno, Depassivation–repassivation behavior of a pure iron surface investigated by micro-indentation, Electrochimica Acta 55 (2010) 1232–1238

[92] T. Yamamoto, K. Fushimi, H. Habazaki, H. Konno, S. Miura, The Effect of Metal Texture on Depassivation-repassivation Behavior of Iron in Borate Buffer Solution Investigated by Micro-indentation, ECS Transactions 16 (2009) 133-140, doi:10.1149/1.3229962

[93] K. Fushimi, T. Shimada, H. Habazaki, H. Konno, M. Seo, Mechano-electrochemistry of a passive surface using an in situ micro-indentation test, Electrochimica Acta 56 (2011) 1773–1780

[94] K. Fushimi, K. Takase, K. Azumi, M. Seo, Current transients of passive iron observed during micro-indentation in pH 8.4 borate buffer solution, Electrochimica Acta 51 (2006) 1255–1263

[95] J.R. Galvele, S.M. de Micheli, I.L. Muller, S.B. DeWexler, I.L. Alanis, Critical potentials for localized corrosion of aluminium alloys, in: B.F. Brown, J. Kruger, R.W. Staehle (Eds.), Localized Corrosion, NACE, Houston, 1974, 580

[96] ASTM G129 – 00(2013): Standard Practice for Slow Strain Rate Testing to Evaluate the Susceptibility of Metallic Materials to Environmentally Assisted Cracking, in: ASTM Volume 03.02 Corrosion of Metals: Wear and Erosion, ASTM, West Conshohocken, 2013

[97] DIN EN ISO 6892-1:2017-02: Metallic materials - Tensile testing - Part 1: Method of test at room temperature, Beuth-Verlag, Berlin, 2017

[98] E. Mujanović, B. Zajec, T. Kosec, A. Legat, S. Hönig, G. Zehethofer, G. Mori, Activation and Repassivation of Stainless Steels in Artificial Brines as a Function of pH, Materials 12 (2019) 3811

[99] A.R. Moshaweh, G.T. Burstein, Evolution of unpredictable behaviour of a passivated stainless steel measured electrochemically, Corrosion Science 113 (2016) 126-132

[100] G.T. Burstein, B.T. Daymond, The remarkable passivity of austenitic stainless steel in sulphuric acid solution and the effect of repetitive temperature cycling, Corrosion Science 51 (2009) 2249–2252

[101] P.A. Lefrancois, W.B. Hoyt, Chemical Thermodynamics of High Temperature Reactions In Metal Dusting Corrosion, Corrosion 19 (1963) 360–368

[102] D.A. Vermilyea, Concerning the Critical Pitting Potential, Journal of The Electrochemical Society 118 (1971) 529–531